

AD-A121 886

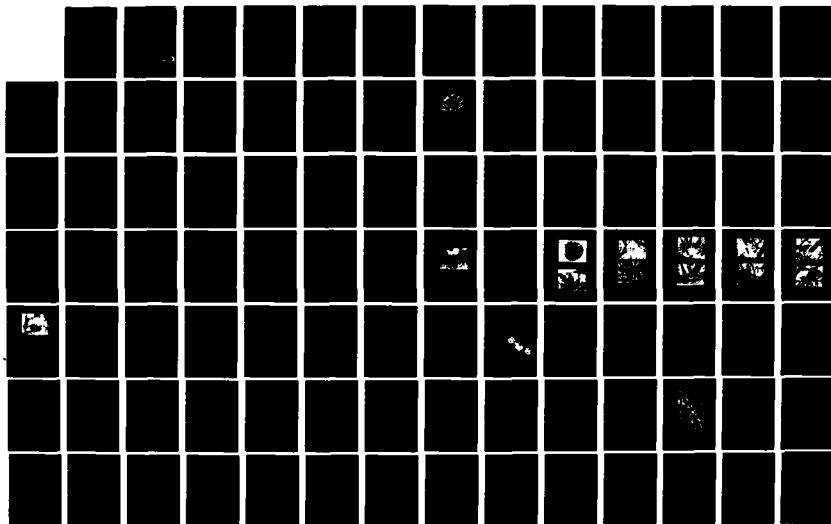
A STUDY OF LOCALIZED PLASTIC DEFORMATION AS RELATED TO
FATIGUE MECHANISMS(U) BROWN UNIV PROVIDENCE RI DIV OF
ENGINEERING J BAIK ET AL. MAY 82 AFOSR-TR-82-0998
AFOSR-77-3246

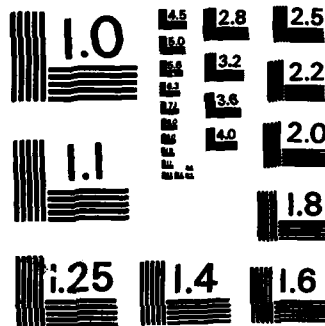
1/2

UNCLASSIFIED

F/G 11/6

NL





MICROCOPY RESOLUTION TEST CHART
NATIONAL BUREAU OF STANDARDS-1963-A

AD A121806

FINAL TECHNICAL REPORT

(AFOSR Grant No. AFOSR-77-3246)

A STUDY OF LOCALIZED PLASTIC DEFORMATION
AS RELATED TO FATIGUE MECHANISMS

Jai-Man Baik
Laurenz Hermann
Robert J. Asaro

Division of Engineering
Brown University
Providence, Rhode Island

May, 1982

DTIC
ELECTE
NOV 23 1982
S D
E

Approved for public release;
distribution unlimited.

DTIC FILE COPY

82 11 22 062

Table of Contents

	<u>page</u>
I. Introduction	1
II. Relevance	2
II.1 Accomplishments	3
III. Summary of Research (taken from J. M. Baik)	5
III.1 Introduction	6
III.2 Cyclic Deformation Behavior and Strain-Life Characteristics	11
III.2.1 Introduction	11
III.2.2 Experimental	12
III.2.2.1 Materials and Specimen Preparation	12
III.2.2.2 Procedures	16
III.2.2.3 Equipment	19
III.2.3 Results	20
III.2.3.1 Monotonic and Cyclic Deformation Response	20
III.2.3.2 Total Strain and Plastic Strain Control LCF Behavior	27
III.2.3.3 Fatigue Life Characteristic	36
III.2.3.4 Fracture Surface Morphology	41
III.3 Crack Growth Under Uniform Loading	51
III.3.1 Introduction	51
III.3.2 Experimental	52
III.3.2.1 Differential Compliance Technique	52
III.3.2.2 Materials and Equipment	59
III.3.3 Results	61
III.3.3.1 Crack Closure Behavior	61
III.3.3.2 Fatigue Crack Growth	66
III.3.3.3 Fracture Toughness	69
III.3.3.4 Fractography	72
III.4 Crack Growth Under Complex Loading: Overload Effects	74
III.4.1 Introduction	74
III.4.2 Experimental	77
III.4.3 Results	78
III.4.3.1 Single Cycle Overload	78
III.4.3.2 Periodic Overloads	83
III.4.3.3 Fractography	96
III.5 Discussion	101
III.5.1 Microstructure Characteristics	101
III.5.2 Monotonic and Cyclic Deformation Response	103
III.5.3 Fatigue Life and Crack Initiation	103

AIR FORCE OFFICE OF SCIENTIFIC RESEARCH (AFSC)

NOTICE OF TRANSMITTAL TO DTIC

This technical report has been reviewed and is approved for public release IAT AFR 190-12.

Distribution is unlimited.

MATTHEW J. KEMPER

Chief, Technical Information Division

III.5.4	Crack Closure and Fatigue Crack Growth Under Uniform Loading	111
III.5.5	Fracture Toughness	118
III.5.6	Overload Retardation and Crack Growth Under Complex Loading	119
III.6	Conclusions	120
III.7	Legions	
III.7.1	List of Tables	122
III.7.2	List of Figures	123
IV.	References	129
V.	Personnel	134
VI.	Reports and Publications	135
VII.	Oral Presentations	136

Accession For	
NTIS GRA&I	<input checked="checked" type="checkbox"/>
DTIC TAB	<input type="checkbox"/>
Unannounced	<input type="checkbox"/>
Justification	
By	
Distribution/	
Availability Codes	
Dist	Avail and/or Special
A	



UNCLASSIFIED

SECURITY CLASSIFICATION OF THIS PAGE (When Data Entered)

REPORT DOCUMENTATION PAGE		READ INSTRUCTIONS BEFORE COMPLETING FORM
1. REPORT NUMBER AFOSR-TR- 82-0990	2. GOVT ACCESSION NO. AD-A2117 806	3. RECIPIENT'S CATALOG NUMBER
4. TITLE (and Subtitle) A STUDY OF LOCALIZED PLASTIC DEFORMATION AS RELATED TO FATIGUE MECHANISMS		5. TYPE OF REPORT & PERIOD COVERED Final Technical Report
		6. PERFORMING ORG. REPORT NUMBER
7. AUTHOR(s) Baik, Jai-Man, Hermann, Laurenz Asaro, Robert J.		8. CONTRACT OR GRANT NUMBER(s) AFOSR-77-3246
9. PERFORMING ORGANIZATION NAME AND ADDRESS Division of Engineering Brown University Providence, Rhode Island 02912		10. PROGRAM ELEMENT, PROJECT, TASK AREA & WORK UNIT NUMBERS 61102F 2306/A1
11. CONTROLLING OFFICE NAME AND ADDRESS AFOSR/NE Bldg 1410 Bolling AFB DC 20332		12. REPORT DATE May, 1982
14. MONITORING AGENCY NAME & ADDRESS (if different from Controlling Office)		13. NUMBER OF PAGES 139
		15. SECURITY CLASS. (of this report) Unclassified
		15a. DECLASSIFICATION/DOWNGRADING SCHEDULE
16. DISTRIBUTION STATEMENT (of this Report) Approved for public release; distribution unlimited.		
17. DISTRIBUTION STATEMENT (of the abstract entered in Block 20, if different from Report)		
18. SUPPLEMENTARY NOTES		
19. KEY WORDS (Continue on reverse side if necessary and identify by block number) fatigue, fatigue crack growth, fatigue crack initiation, cyclic deformation, computer control testing, localized deformation, crack tip closure, overload retardation, differential compliance		
20. ABSTRACT (Continue on reverse side if necessary and identify by block number) This is concerned with a study of the micro- and macromechanics of fatigue crack initiation and crack propagation in an age-hardenable 2048 aluminum alloy, which is the high purity version of 2024 or 2124 aluminum, and their relation- ship to localized plastic deformation. Special attention was given to the importance of microstructure, including grain size and ageing treatment in cyclic response and low cycle fatigue (LCF) behavior, crack growth along with the phenomena of crack tip closure, and on overload retardation effects. Crack closure was studied in detail throughout the course of this research program		

Unclassified

SECURITY CLASSIFICATION OF THIS PAGE(When Data Entered)

20. Abstract (continued)

and its use in describing crack growth was explored. Fracture toughness tests were performed and the results were compared with the K_{IC} value reported in literature. Discussion is also included on the experimental techniques used in this research since they are novel and should have quite general applicability in fracture mechanics theory.

The results show that the LCF performance and thus fatigue initiation life based on the plastic strain control tests do not show any appreciable differences between different temper materials, but crack closure levels, crack growth rates and overload retardation are well influenced by microstructure. The lowest crack growth related to highest crack tip closure loads and the largest amount of overload retardation are associated with underaged microstructures which are prone to display non-uniform deformation pattern characterized by localized shearing. The closure model is also shown to provide an accurate description of overload retardation following single cycle and multiple cycle overloads in that we found a very good correlation between crack growth rate and "effective stress intensity range" ΔK_{eff} .

Unclassified

SECURITY CLASSIFICATION OF THIS PAGE(When Data Entered)

model developed earlier in this program indicated that a large grain size appears to favor localized shearing which in turn leads to fatigue crack initiation.

The concept of an effective stress intensity range has also been studied in detail. This has been done by studying the kinetics of crack growth through overload affected zones. The results show that, provided the plastic zone is indeed larger than the grain size, Elber's concept of an effective ΔK range is a useful quantitative guide for describing non-uniform loading histories. Our work in this area has led to the further development of an extremely sensitive experimental technique for monitoring small increments of crack growth. The technique will be described in more detail later where its accuracy will be discussed by comparing crack growth increments between overloads measured by the compliance technique to the same growth increments measured by scanning electron microscopy after complete fracture of the specimen.

The most recent work on the project has been concerned with crack initiation. This work included a study of cyclic deformation response and the determination of overall fatigue life in tension. Metallurgical variables were chosen to match those used in our crack growth studies. Our results are interesting in that very similar plastic strain life behavior was found, at least in the small axisymmetric tension-compression specimens we tested, for the three tempers T351, T851 and T851*. An explanation for this might be found in the observation that in the T351 temper cracks tended to initiate but grow slower than in either the T851 or T851* tempered specimens. Crack initiation mechanisms included localized slip (i.e., localized shearing) and second phase particles. Since microstructures containing coherent or semicoherent zones or precipitates are known to be more prone to localized shearing, it is possible that crack initiation within shear bands occurs more readily in alloys with a T351 temper.

II. Relevance

An understanding of fatigue mechanisms, especially those causing crack initiation and growth, will undoubtedly play a major role in future development of more fatigue resistant materials to be used in aircraft design. Metallurgical variables such as grain size, precipitate (dispersoid) type

I. Introduction

One of the most common features of metal plasticity is the tendency for uniform patterns of deformation to break down into patterns which are characterized by highly localized modes. When these modes take the form of localized necks or shear bands they act as direct, or at least imminent, precursors to rupture.¹⁻⁴ Precipitation hardened alloys, and especially the kind used in aircraft construction, are particularly prone to localized shearing during both monotonic and cyclic deformation.^{2,5-8} This project has been concerned with evaluating the role of localized shearing in cyclic deformation, fatigue crack initiation, and propagation in 2000 series aluminum alloys.

Our work has led to the development of new techniques for measuring fatigue crack growth and for experimentally determining crack opening and closing loads. We have applied the technique to the study of fatigue crack growth in 2048 aluminum. Metallurgical effects concerned with ageing treatment were studied in some detail; for example, we have found that the highest crack tip closure loads and lowest crack growth rates, are associated with underaged microstructures. In addition we have found that grain size also has an important effect on crack growth in that increasing grain size tends to decrease crack growth rates and increase crack closure levels. Furthermore, studies of overload retardation have shown that underaged or peakaged microstructures undergo the largest amounts of retardation.

As just mentioned, it was found that grain size has a very important effect on crack growth rates. We have shown, for example, that the size of the crack tip plastic zone, in relation to the grain size, determines the kind of crack opening behavior that is observed. When the plastic zone size is less than the grain size, crack growth is characterized by large amounts of out-of-plane shearing caused by the inhomogeneous, localized shearing within the grain matrices ahead of the growing crack. When the plastic zone size is larger than the grain size, the tendency for out-of-plane shearing is much less, the closure levels fall--they actually undergo a transition--and the growth rate is increased. Grain size was also shown to have an important role in determining the tendency for localized shearing to set in within individual grains. An analytical

resulting slower rates of crack growth) can be achieved by grain size control. Unfortunately this usually involves a coarsening of grain size which may also lead to decreases in fracture toughness. Underaged microstructures (corresponding to commercial tempers like T351) also give rise to lower growth rates than peakaged microstructures (corresponding to commercial tempers such as T851) or slightly overaged microstructures. Our results on overload retardation are consistent with this in that the greatest amounts of retardation following multiple, single cycle overloads was observed in underaged microstructures.

The quantitative usefulness of the closure concept has been tested by correlating the kinetics of crack growth through overload affected regions in terms of an "effective stress intensity" range, $\Delta K_{\text{eff}} \equiv K_{\text{max}} - K_{\text{open}}$. For single cycle overloads the correlations were quite good although the observed phenomenology of closure was found to be rather complex.

Some of the effects of microstructure on crack growth have been interpreted in terms of micromechanical models for plasticity in age-hardened alloys. These models suggested that large grain materials would display larger amounts of out-of-plane shearing at a crack tip. This is the result of an increased tendency for localized shearing within the grain matrices. This, in turn, could lead to very much rougher fracture surfaces and lower crack growth rates. These models also predicted a reduced tendency for localized shearing near a crack tip after the crack tip plastic zone reached beyond a grain size, which is consistent with the observed transition in closure levels. The transition from high to low values of closure loads correlated well with a critical value of K_{max} which in fact yielded a computed plastic zone size approximately equal to the grain width.

In the latter part of the project a study of cyclic deformation response and overall fatigue life was undertaken. The results of this study helped put our studies of crack growth in clearer perspective. For example, whereas crack growth was found to be slower in our T351 temper than in either the T851 or T851* tempers, overall fatigue life need not be increased. This is apparently due to earlier crack initiation occurring within localized shear bands.

and distribution, as well as environment are important and their effects on fatigue crack initiation and crack growth must be understood more fully. Furthermore, since the mode of crack initiation and advance is sensitive to metallurgical structure, and since fracture modes can be shown to significantly influence such properties as the rate of crack initiation and growing crack tip phenomenology such as crack tip closure, it is important to also explore the effects of microstructure on fatigue crack opening and closing stress intensities. Furthermore, because crack closure plays an important part in overload retardation, there is the possibility of improved resistance to crack growth for non-uniform loadings by choosing materials or microstructural controls that maximize closure effects.

The role of microstructure in aluminum alloys in fatigue crack initiation, crack growth, closure and overload retardation have been studied in this research.

II. 1. Accomplishments

Over the course of this project we have studied, in detail, the micro and macromechanics of fatigue crack growth in structural aluminum alloys, principally 2048 aluminum. We have developed an extremely accurate differential compliance technique, originally begun at Brown by Paris and Hermann, for measuring fatigue crack growth and crack tip closure. The technique has been used to study fatigue crack growth, crack tip closure, overload retardation in age-hardened 2048 aluminum and, more recently, response to spectrum loading histories. In addition to these experimental studies, theoretical work under the project included an analysis of crack tip plasticity for a steadily, and quasi-statically, propagating crack, along with a model for the localized shearing within a single grain. This single grain model was aimed at trying to understand why coarse grained materials appear to show an increased tendency to undergo localized shearing, which, in turn, leads to out-of-plane crack growth. The crack tip plasticity studies highlighted some of the interesting effects of plastic "wakes" left behind the propagating crack tip.

During the course of this project we have made several interesting observations of the effects of microstructure on crack growth and crack initiation. We have demonstrated that large crack tip closure loads (and

In summary, we feel this project has made a strong contribution to the experimental methodology used in the study of fatigue crack growth and fracture mechanics. We have characterized crack growth behavior in 2048 aluminum in detail, and have provided new insights into the important but difficult concepts of crack closure. Finally, we have highlighted some of the more important effects of microstructure on crack tip plasticity and localized shearing during fatigue crack initiation and growth, including crack retardation following overloads.

III. Summary of Research

This section contains the text of the Ph.D. Thesis of Dr. J. M. Baik. This thesis discusses and presents key results from the project and is written with good perspective of relevant work found in the literature.

III. 1. Introduction

An understanding of fatigue mechanisms in metals and alloys will undoubtedly play a major role by providing an absolute guideline in the future development of more fatigue resistant materials.

During the past twenty years or so extensive studies of the mechanisms of fatigue have been carried out to provide a basic understanding necessary for describing fatigue in terms of specific processes such as cyclic deformation response, crack initiation, and crack propagation. This research has highlighted in particular the importance of microstructure in fatigue failure.

Microstructural variables such as grain size, precipitate (or inclusion) type and distribution, in addition to environment are known to be especially important and their effect on fatigue crack initiation and crack growth must be understood more fully.

The fatigue failure process can be subdivided into three stages: (1) cyclic deformation prior to crack nucleation, (2) crack initiation and (3) crack growth. The former two stages belong to the fatigue crack initiation period and the last stage belongs to the fatigue crack propagation period. Generally fatigue crack initiation is studied, with low cycle fatigue (LCF) performance, in smooth specimens, and crack propagation is studied in notch members. This means that crack initiation is usually interpreted using cumulative strain models while crack propagation is associated with the growth of a large through-crack treated in the sense of conventional fracture mechanics.

It is now understood that localized plastic deformation plays an important role in both the initiation and propagation of fracture. Also, the significance of localized shear processes has been demonstrated in both monotonic as well as fatigue failures, and in both cases there are important microstructural or material effects involved. Therefore, it is of particular importance to develop a general understanding of localized plasticity in the fatigue process since in many polycrystalline alloys, notably age-hardenable alloys of aluminum, titanium and nickel, localizations have been shown to control both cyclic deformation response and early crack initiation (1-3). This localization phenomena can be linked to particular properties of microstructure. In alloys of age-hardenable aluminum-copper system, for example, when the matrix is hardened by small coherent precipitates or GP zones rather than by incoherent precipitates, highly localized bands of shear strain develop due to precipitates shearing.

It is also becoming increasingly clear that localized plastic deformation plays an important role in fatigue crack advance. Here, again, the materials which seem to show pronounced effects are age-hardenable alloys, especially those with a face-centered cubic crystal structure. Generally, underaged alloys containing coherent, shearable precipitates show the greatest amount of localized shearing (4), often with accompanying crack growth rates which are less than in the overaged condition containing incoherent, nonshearable particles with comparable yield strengths. Suitable explanations for these observations have not yet been reported.

Since Elber's (5,6) experimental discovery of crack tip closure, the closure model has been employed by numerous investigators in the analysis of fatigue crack growth. Elber (5,6) proposed that the residual stretch of material left in the wake of the propagating crack induces the compressive residual stresses on the crack tip due to incompatible mating fracture surfaces and thus reduces the effective load for crack propagation. The closure concept can be formulated through an "effective stress intensity" range $\Delta K_{eff} = K_{max} - K_{open}$, where K_{max} is the maximum stress intensity applied and K_{open} is defined as the stress intensity level required to actually open the crack tip against compressive "closure" forces which act to close it. With this notion of an "effective stress intensity" range ΔK_{eff} , a number of attempts have been reported to explain various phenomena such as crack retardation following overload (7,8), R ratio effects on fatigue crack growth (6,9), the influence of mean stress on crack growth thresholds (10) and environment effects on the rates of crack growth (11,12). In this ΔK_{eff} approach, it is hypothesized, following the procedures introduced by Paris (13), that the fatigue crack growth rate, da/dN , can be uniquely related to ΔK_{eff} .

Crack closure behavior also seems to be affected by mode of crack advance. Paris and Hermann (7) have observed well defined high closure-to-low closure transitions in 2024 aluminum, which occurs with an obvious change in fracture surface topology. These transitions seem to be related to the mode of crack advance, since substantial amounts of shearing process produce a characteristically "zig-zag" crack path morphology and since this resulting rough fracture surface can be responsible for the

high closure levels. On this point, McEvily (10) has recently discussed the possibility that high closure stress intensities may result from the large components of shear fracture in the low K_{max} range. Further, there is an interesting fractographic observation (14) showing that crack growth occurs by a Mode II (shear mode) process at low stress intensity level and by a Mode I (opening mode) at high stress intensity level. These shear mode fractures are influenced by localized shearing in the grain matrices, which is also enhanced in underaged state containing coherent particles.

Another interesting example of slip induced closure effects has been reported by Louwaard (15) on 7075 aluminum of different grain size. The large grained alloys displayed a "slip band cracking" fracture mode within the grains which lead to high closure levels and low values of crack growth rate, but in fine grained alloys similar phenomena were not observed. While it may be that large grains impose less restraints on grain matrix shearing, there are a number of observations which suggest that the slip properties are also very important in determining if localized shear will occur. For example, Hornbogen and Graf (16) found that localized shearing, slip-band decohesion, and reduced crack growth rates also occurred in sheets of underaged iron-nickel-aluminum alloys. These were not grain size effects, but were clearly related to the precipitate's size and degree of coherency. Localized shearing and slip band cracking did not occur in overaged alloys. These studies, however, did not include measurements of crack closure.

Now, while it seems clear that there are important microstructural and slip induced effects in the closure process, the fundamental relationships

between them and crack growth mechanisms and growth rates are not yet clearly understood. The purpose of this research is to study the micro- and macro-mechanics of both fatigue crack initiation and crack propagation, and to investigate their relationship to localized plastic deformation in age-hardenable 2048 aluminum alloys. Precipitation-hardened aluminum alloys have received special attention due to ease of microstructure control by ageing treatment and because of the high performance of the various microstructures. In particular, 2048 aluminum has been recently developed for aircraft construction material by increasing its fracture toughness. Special attention was given in the present study to the importance of microstructure, including grain size and ageing treatment in cyclic response and LCF behavior, crack growth along with the phenomena of crack tip closure, and on overload retardation effects.

In order to characterize the material properties of different microstructures studied, the monotonic and cyclic deformation behavior and LCF performance were investigated by strain control tests and their results are contained in Section II. Since crack closure was studied in detail throughout the course of research program, and its use in describing crack growth was explored, considerable discussion on the concepts and results are included in Section III along with the fracture toughness values and crack growth behavior under constant amplitude loading.

As a vital step toward understanding fatigue crack growth under conditions of spectrum loading, as encountered in service, tests were carried out for the purpose of studying specimen response to multiple

cycle overloads. The attempt was made to quantitatively describe the observed crack growth retardation following such overloads using the measured crack opening loads. Results of these tests are summarized in Section IV.

III. 2. Cyclic Deformation Behavior and Strain-Life Characteristics

2.1 Introduction

In a study of the cyclic deformation behavior of metals, it is important to consider their cyclic stress-strain curves. Most metals show either cyclic hardening or softening when they are subjected to cyclic plastic deformation. Cyclic hardening or softening is usually observed by varying the applied stress under constant strain control or by varying the applied strain amplitude under constant stress control during cyclic deformation. It has, however, become clear that plastic strain is the controlling parameter in metal fatigue, and so it is more appropriate to control the strain limit rather than the stress limits (22). This circumstance is not without practical justification, since in many structural components the material at the critical location (a notch root, the surface of a bending member, etc.) is subjected to essentially strain cycling conditions due to the constraint of surrounding elastic material (17).

The interest in low cycle fatigue (LCF) testing stems directly from the need for information on metals when subjected to relatively few cycles, viz., failure in fewer than 5×10^4 cycles by definition, of controlled cyclic strain (18). In the present LCF test program, the emphasis was put on the cyclic deformation response shown by cyclic stress-strain curves and

the fatigue initiation resistance shown by plastic strain-fatigue life relation of different microstructures studied. The cyclic stress-strain curve was obtained by the incremental strain step test, and the plastic strain - fatigue life relation was obtained by both total strain control test and plastic strain control test. It turned out that the plastic strain control test provided a more accurate correlation with the Coffin-Manson plot for materials which do not show a clear saturation of stress but consistent hardening-softening behavior over the entire plastic strain range.

Finally, the fracture surfaces of different microstructures studied were also investigated by scanning electron microscopy (SEM).

2.2 Experimental

2.2.1 Materials and Specimen Preparation

The material used in this series of experiments was 2048 aluminum alloy whose chemical analysis is given in Table I. Aluminum alloy 2048 is a relatively new material designed for aircraft applications with improved fracture toughness. This has been achieved by lowering the content of copper and reducing the content of impurities such as iron and silicon below that normally found in aluminum alloy 2024. Excess amounts of copper yields high levels of undissolved soluble phase θ (CuAl_2), whereas both iron and silicon produce large particles of insoluble intermetallics ($\text{Al}_7\text{Cu}_2\text{Fe}$, Mg_2Si and $(\text{Fe}, \text{Mn})\text{Al}_6$) by eutectic decomposition during ingot solidification (19). These second phase particles have a well-known detrimental effect on the fracture toughness of age-hardenable aluminum alloys since they can be fractured during primary processing and their incoherency promotes void growth and coalescence.

The material obtained from the Reynolds Metals Company as a 28 mm thick plate in the -F temper was solution heat-treated in a lead-melt bath at 495°C for 3 hours, quenched in cold water of 20°C and immediately (i.e. within 1 hour) stretched to 2 percent plastic deformation for residual stress relief. This was followed by appropriate ageing and subsequent machining to a final specimen size. The three ageing conditions to be reported on here are described in Table II. The typical grain structure of plate obtained after T351 temper are shown in Figure 1 in which A denotes the rolling direction and B, C will be explained in the next section.

To study grain size effects, the finer grain size plate with T851 temper (to be referred to as fine grained hereafter) was also tested. The grain sizes measured across the long transverse cross section perpendicular to the loading axis are 0.063 mm and 0.19 mm for fine grain and coarse grain material, respectively.

Uniaxial, cylindrical specimens with threaded ends were employed through the LCF test programs. Specimens were machined such that the loading axis is parallel to the rolling direction A in Figure 1. The area of gauge section was determined by considering the loading capacity of the Wood's metal grip. To prevent plastic buckling during compression, a length-to-diameter ratio of 2 was chosen. The shape and dimensions of specimen are shown in Figure 2.

Since it is well understood that surface finish has a large effect on the crack nucleation period, all specimens were mechanically polished with a series of abrasive paper down to 15 μ m on the

TABLE I

Chemical Analysis of 2048 Aluminum in Weight Percent

element	Si	Fe	Cu	Mn	Mg	Cr	Ni	Zn	Ti	Al
%	.05	.09	3.9	.54	1.59	<.01	<.01	.01	0.15	Rem.

TABLE II

Ageing Designation and Condition Used for 2048 Aluminum Specimen

<u>Temper Designation</u>	<u>State</u>	<u>Description</u>
T851*	slightly overaged	solution heat treated, cold worked, stress relieved by stretching and artificially aged at 190°C for 24 hours.
T851	peakaged	same as above except for artificial ageing at 190°C for 12 hours.
T351	underaged	same as above except for ageing at room temperature.

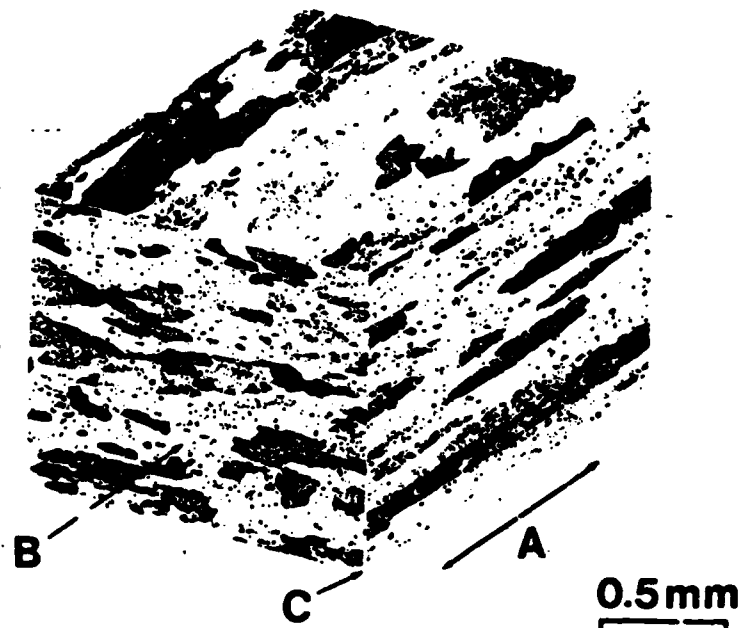


Figure 1: Typical grain structure in 2048-T351. A shows the rolling direction. Crack's plane is parallel to face B and its front is parallel to edge C.

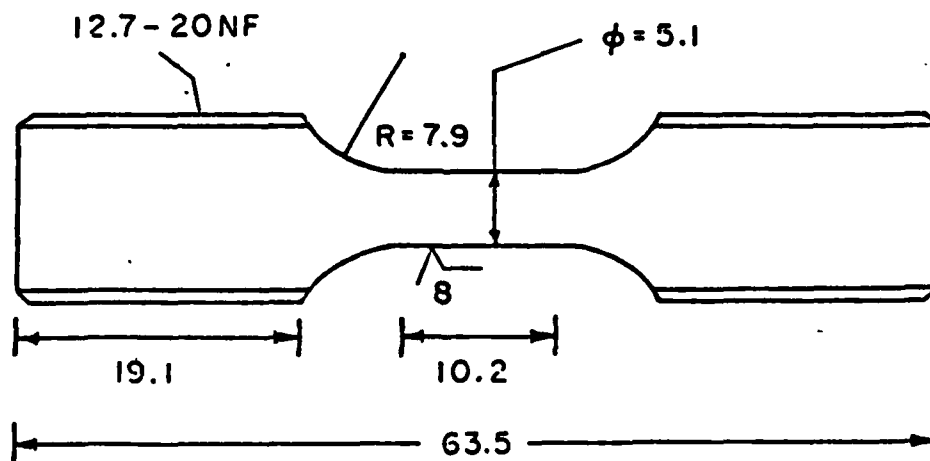


Figure 2: Dimensions of low cycle fatigue specimen (unit : mm)

lathe and finally electropolished until both the machining marks and the surface scratches completely disappeared. This electropolished surface provided an equal surface quality as well as a good surface for slip line and surface crack observation under an optical microscope. A solution of 800 ml ethanol and 60 ml perchloric acid (60%) was used for electrolyte. The diameter of the specimen was measured with an optical micrometer having the resolution power of 2.5×10^{-3} mm to keep the surface scratch-free.

2.2.2 Procedures

Three types of the low cycle fatigue (LCF) tests were performed to investigate the cyclic deformation response and to compare the fatigue resistance for different tempers and microstructures: an incremental strain test, a total strain control test and a plastic strain control test.

The incremental step strain test, originally proposed by Landgraf, et al. (20) to determine the cyclic stress-strain curve, consists of subjecting specimens to blocks of decreasing-increasing strain-time history. A maximum strain amplitude of ± 2.0 percent was selected since that range is usually sufficient to cyclically stabilize the metal quickly without the danger of causing the specimen to neck, fail or buckle before a stable state is achieved (20). In these blocks, a zero strain amplitude was reached after 40 cycles and the maximum strain amplitudes after another 40 cycles. A solid, stabilized cyclic stress-strain curve was obtained after the application of several blocks and the test was continued until the specimen fractured. By comparing cyclic curves with monotonic stress-strain curves cyclic softening or hardening behavior

can be characterized.

Fully reserved, total strain control tests were performed to obtain the strain-fatigue life relation of different microstructures. The procedures for this test are well established and are similar to those described elsewhere (21,22). Fatigue life was determined at the point where tensile load peak dropped down to half of first cycle tensile peak.

When large fatigue cracks develop on the final stage of test, the hysteresis loops are distorted and show an inflection point in the compressive portion of them. Figure 3 is given as an example of this behavior. Once this malformed hysteresis loop has formed on compressive reversal, the tensile peak continues to drop rapidly while the compressive peak remains almost constant. The testing was done under low strain amplitudes, i.e. less than 1 percent strain.

Finally, the plastic strain control test was conducted under computer control. It is programmed that when the apparent strain calculated by electronic signal from strain gauge reaches the value of plastic strain setting plus the elastic strain computed at instantaneous load level, the loading direction is reversed. The instantaneous elastic strain was computed from instantaneous stress divided by elastic modulus already determined from cyclic stress-strain relation. The peak loads of both tensile and compressive reversals were also detected directly and accurately by electronic signal from the load cell and the average stress level was computed simultaneously over the programmed intervals of equal logarithmic values. From these data, a cyclic hardening or softening curve can be constructed by plotting the stress required

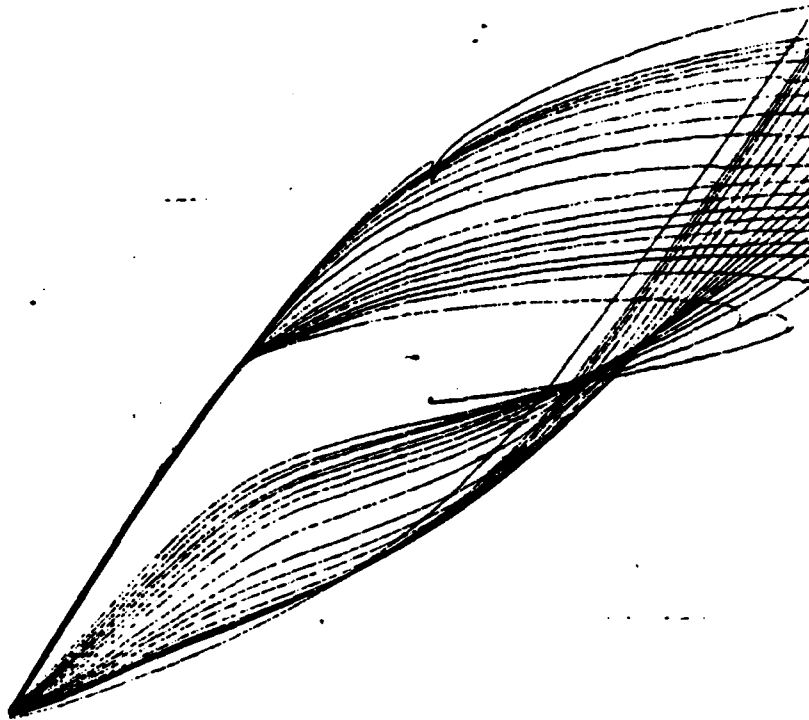


Figure 3: The final stage of total strain control LCF test shows the distorted hysteresis loop when a macroscopic large crack developed. Note that the tensile peak continuously drops while the compressive peak remains nearly constant.

to maintain the imposed strain as a function of the number of cycles.

2.2.3 Equipment

All mechanical tests were conducted on an Instron closed loop servo-hydraulic test machine of 44 kN (10 kips) capacity in laboratory dry air at room temperature. Since, in total strain control, a fractured specimen may continue to cycle even though there is a zero tensile load response, an under-peak detector on the Instron machine was used to prevent equipment and specimen damage. This shut-off device requires that a pre-determined tensile load (in this case, 50 percent of the initial tensile peak) be reached on each successive cycle for the test to continue. Thus, when a large crack develops in a specimen and the tensile peak load falls below this preset value, the machine will immediately and automatically stop, preventing the pounding together of the fractured ends of specimen, and thus permitting the examination of undamaged fracture surfaces. For the plastic strain control LCF tests, a PDP-11/34 mini-computer was used to control an Instron testing machine with an interface designed and fabricated at Brown University.

For gripping the specimens, 12.7 mm-20NF threaded grips were used to prevent slipping during tensile and compressive reversals. It should be sure that the specimen is firmly tightened to the grip not to show any free play on the reversals of loading.

In order to assure proper axial alignment of specimen with the loading axis, a grip of a low melting alloy (so-called Wood's metal) was used. A clip-on extensometer with 8 mm gauge length was used for the strain measurement and accurate to strains as well as 10^{-4} . Since

the sharp knife edges on extensometer can provide an easier crack initiation site, Scotch-Brand magic tape was used on the contact points of the gauge section to prevent the earlier-than-expected failure. Even with these precautions some specimens, especially soft specimen of T351 temper, failed from the contact points and were excluded from the consideration of results. The extensometer usually undergoes some drift until the knife edges settle into the tape and a waiting period of 15 minutes were required.

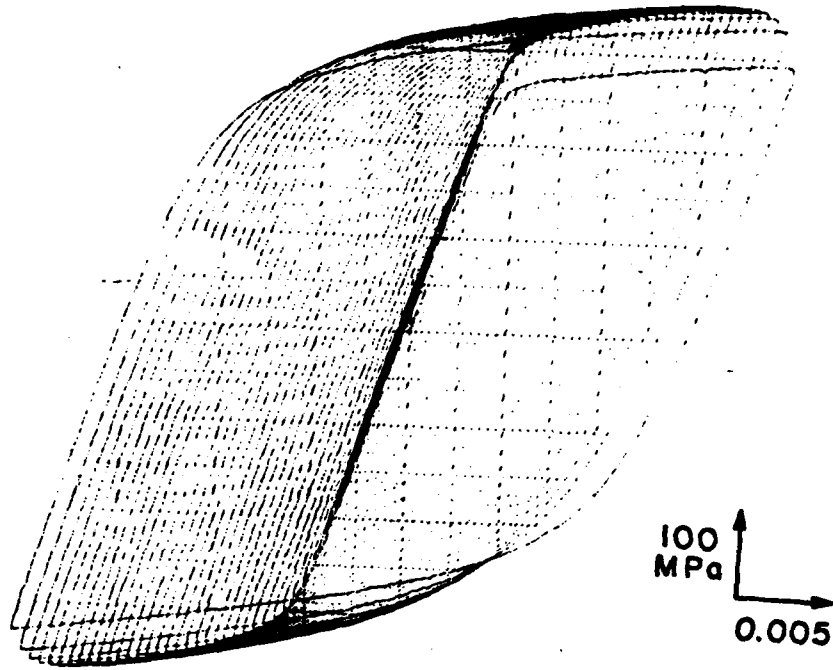
During the course of the strain control LCF tests, the first ten stress-strain hysteresis loops were autographically recorded and subsequent recordings of fixed, equal logarithmic intervals were obtained.

After completing the LCF test, the crack profile and the fracture surface was examined under optical microscope and scanning electron microscope (SEM) to study the fracture morphology. Energy dispersive X-ray analysis (EDAX) was frequently used for analyzing the second phase particles or interesting areas.

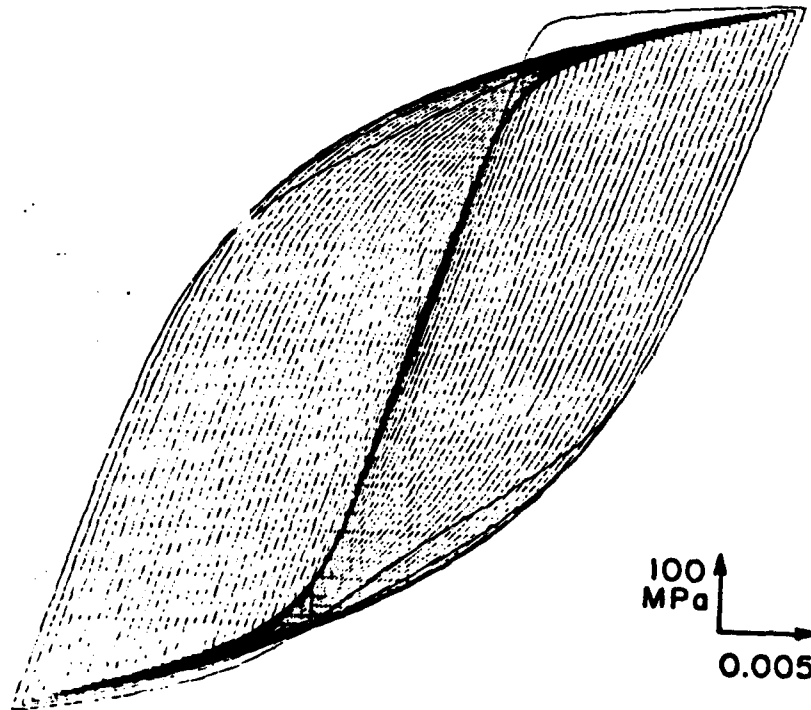
2.3 Results

2.3.1 Monotonic and Cyclic Deformation Response

During the incremental strain step tests, the stress-strain hysteresis loops were continuously recorded for all tempers until the specimen failed completely by crack propagation through the cross section. Figures 4a, b show initial cyclic hardening and softening behavior for the T351 and T851 tempers, respectively, during the first decreasing strain block. After several blocks, the stable hysteresis loops were obtained as shown in Figure 4c, for the T851*

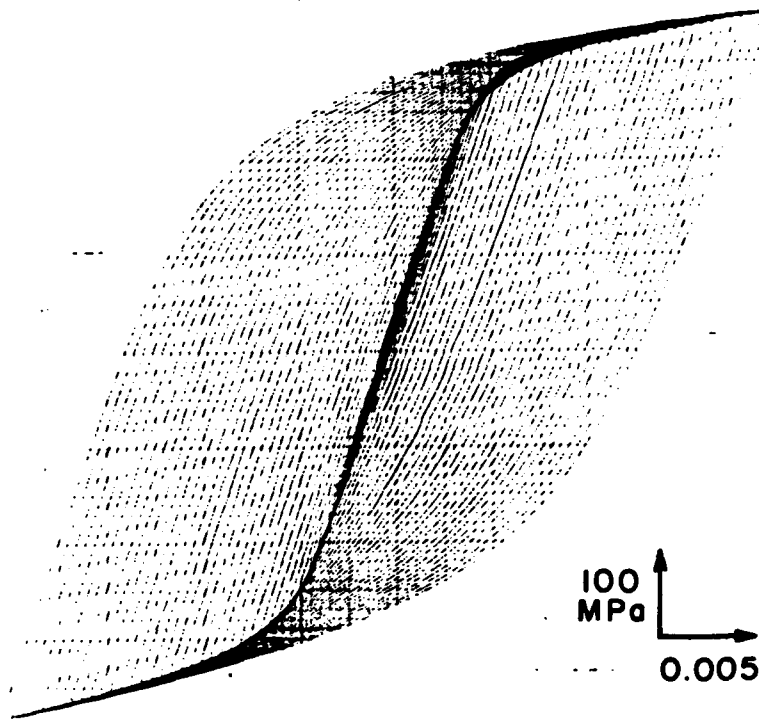


(a)



(h)

Figure 4: (Captions on next page)



(c)

Figure 4: Hysteresis loops during the incremental strain step test.

(a) T351 temper shows the cyclic hardening behavior.

(b) T851 temper shows the cyclic softening behavior.

(c) T851* temper after 3 blocks of incremental strain shows the stable, solid hysteresis loops.

(a) and (b) taken from the first decreasing strain block are not stabilized yet. Monotonic stress-strain curves were taken from the first quarter cycle of (a) and (b).

temper. There was essentially no difference in these stable loops for both decreasing and increasing strain increment of cycling. Cyclic stress-strain curves drawn through the tips of these stable hysteresis loops are shown in Figures 5a, b, c, d for all different microstructures studied along with the monotonic curves which were taken from the first quarter cycle. By comparing the cyclic stress-strain curve with the monotonic curve, the nature and extent of cyclically induced changes are immediately apparent. Table III shows the tabulation of monotonic and cyclic tensile properties of all tempers including the different grain sizes. In both monotonic and cyclic deformation yield strengths at 0.2 percent strain offset are reported, and monotonic (cyclic) strainhardening exponents are the best-fit slopes of logarithmic monotonic (cyclic) stress-plastic strain plots. It can be seen from this table that subsequent artificial ageing at 190°C produces higher strength and the lower ductility. The overaged temper designated as T851*, however, shows reductions in both strength and ductility from the peak-aged temper. The effect of grain size shows that the fine grain material has superior strength and ductility as compared to the same temper of the coarse grain material. The hardening exponents of all tempers increase by a factor of two or three showing steeper curves in cyclic deformation.

All cyclic stress-strain curves show no transition of hardening to softening or vice versa, but rather consistent hardening or softening for all the strain ranges studied. A higher degree of cyclic softening is observed in the overaged temper than in the peak-aged temper.

In this test the T351 temper failed after 3 1/2 blocks, whereas

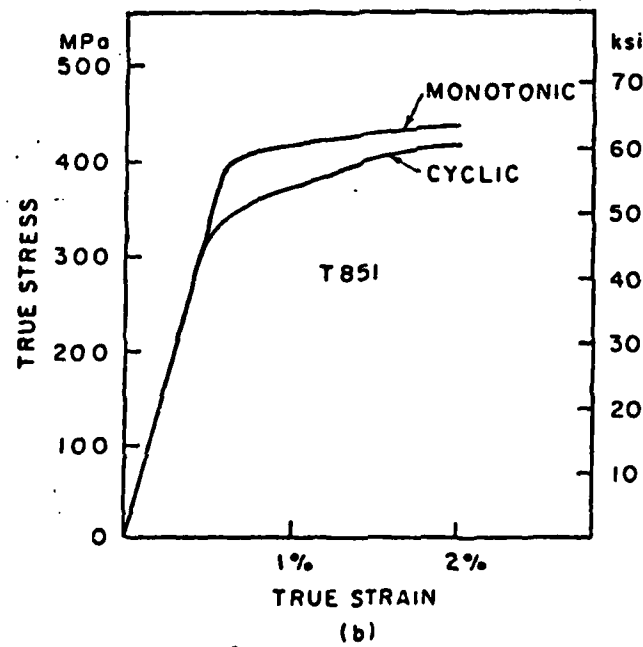
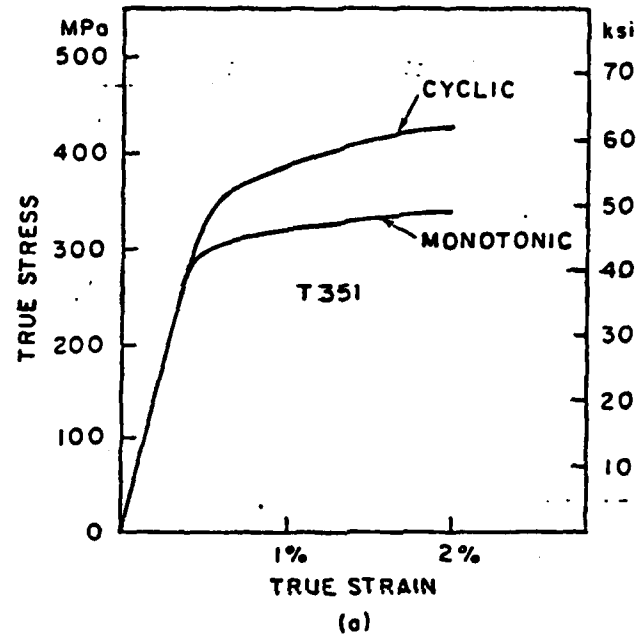


Figure 5: (Captions on next page)

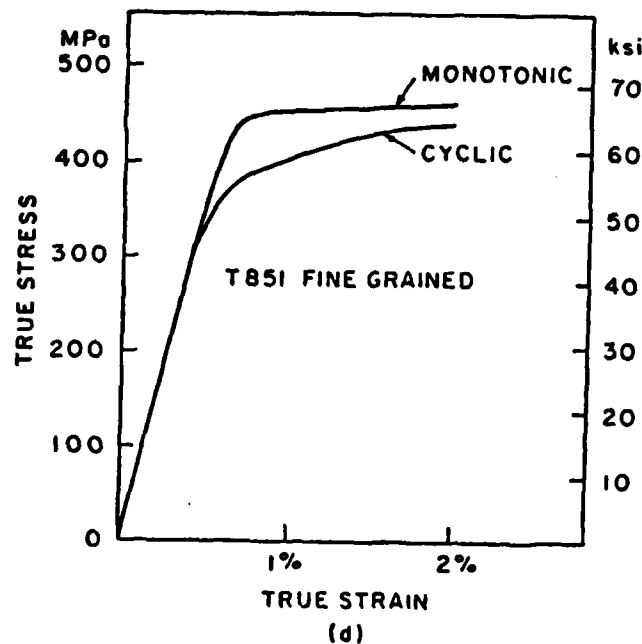
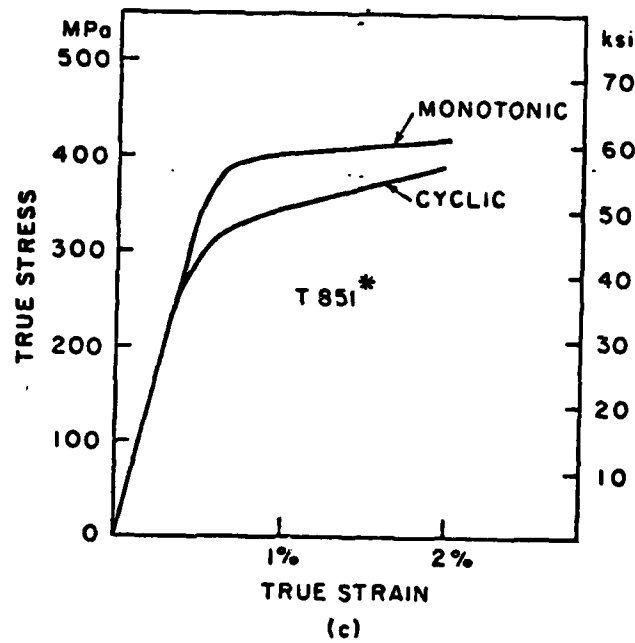


Figure 5: Monotonic and cyclic stress-strain curves obtained during incremental step test. (a) T351 temper is cyclically hardened over the entire plastic strain range. (b) T851, (c) T851*, and (d) fine grained T851 temper are cyclically softened over the entire plastic strain range.

TABLE III

Monotonic Tensile and Cyclic Parameters

	T351	T851	T851*	Fine Grained T851
<u>Monotonic</u>				
σ_y MPa(ksi)	303 (44.0)	410 (59.5)	397 (57.6)	446 (64.7)
σ_u MPa(ksi)	384 (55.7)	452 (65.5)	428 (62.1)	492 (71.3)
σ_u/σ_y	1.27	1.10	1.08	1.10
RA	32	29	27	30
ϵ_f	0.24	0.15	0.12	0.17
k MPa(ksi)	404 (58.6)	486 (70.5)	475 (68.9)	490 (71.0)
n	0.044	0.026	0.030	0.015
<u>Cyclic</u>				
σ'_y MPa(ksi)	367 (53.3)	352 (51.0)	324 (47.0)	381 (55.2)
ϵ'_f	4.4	4.3	2.3	2.9
k' MPa(ksi)	572 (82.9)	582 (84.5)	563 (81.7)	598 (86.7)
n'	0.070	0.080	0.091	0.073
C	-0.95	-0.94	-0.86	-0.89

Monotonic

σ_y : 0.2% offset yield strength

σ_u : ultimate tensile strength

RA: reduction in area

ϵ_f : true fracture ductility

k: strength coefficient, $\sigma = k(\epsilon_p)^n$

n: strain-hardening exponent

Cyclic

σ'_y : 0.2% offset cyclic yield strength

ϵ'_f : fatigue-ductility coefficient

k': cyclic strength coefficient,
 $\Delta\sigma/2 = k'(\Delta\epsilon_p/2)^{n'}$

n': cyclic straining hardening exponent

C: fatigue-ductility exponent

the other tempers failed after 6 blocks. This result also suggests that the T351 temper is inferior to the other tempers in fatigue initiation resistance. The detailed comparison will be given later by the relation of fatigue life versus plastic strain amplitudes applied.

2.3.2 Total Strain and Plastic Strain Control LCF Behavior

Typical hysteresis loops from 1 to 10 cycles for the fine grained T851 temper are shown in Figure 6, tested at a total strain amplitude of $\pm 1.0\%$. In the initial reverse cycle into compression, a doubly inflected curve with a portion of convex curvature has resulted. After several cycles, these inflected behaviors of reverse deformation diminished and stabilized into normal cyclic hysteresis loops with gradual cyclic softening. These characteristic hysteresis loops were also observed for the T851* and the T851 tempers of coarse grain material. This behavior implies that dispersion hardening with an Orowan mechanism is active in these tempers materials probably due to large precipitation particles of $S'(Al_2CuMg)$. Even though microconstituent analysis was not performed due to the complexity of commercial alloys, it has been well known that a reasonable amount of incoherent, non-shearable S' particles as well as large semicoherent and shearable GPII zones are formed during these tempering conditions.

Asaro (23) suggested in his kinematic hardening model that this inflected behavior is due to a non-linear elastic behavior and a memory effect of the non-shearable precipitates with the matrix having low stacking fault energy. In contrast to the previous tempers, the T351 temper showed the normal hysteresis loop without any inflection behavior

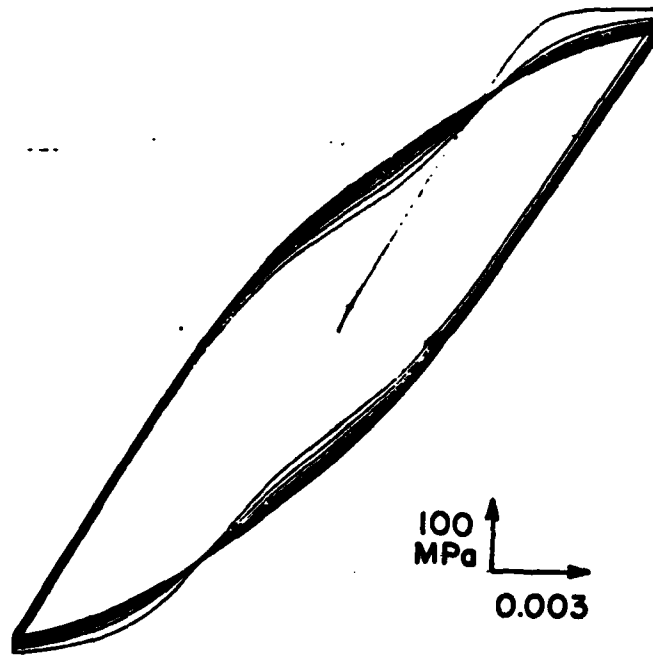


Figure 6: Cyclic hysteresis loops from 1 to 10 cycles from the fine grained T851 temper, tested at total strain amplitude of $\pm 1.0\%$. The doubly inflected behavior of reversed deformation are shown clearly in the first hysteresis loop and diminishes as the cyclic loading goes on.

implying that the precipitation hardening attributed to shearable, coherent GPI particles dominates (24).

The flow stress variations with respect to the number of reversals applied for different values of total strain amplitudes are plotted in Figures 7a, b, c, d, for all tempers studied. Since the hysteresis loops, especially in low strain amplitude cycling, showed different peak levels of tensile and compressive reversals, the cyclic stress amplitudes were determined by taking average values of those stresses in each hysteresis loop. Only the T351 temper showed continuous cyclic hardening whereas all other tempers showed continuous cyclic softening until final fracture. As expected from cyclic stress-strain curves, there was no transition from hardening to softening or vice versa up to the point of final failure. It should be noted that the abrupt drop of stress level at the end stage of life is not due to softening but due to the presence of cracks large enough to be observed in a low power magnifier and coincides with the onset of a distorted hysteresis loop in compressive reversals. The degree of cyclic hardening/softening was enhanced at high strain amplitudes with rapid initial hardening/softening followed by slow hardening/softening, whereas that is less evident at low strain amplitudes. When interpreting the result, it should be noted that the number of reversals is plotted on a logarithmic scale. There seems to be no saturation at high strain amplitudes and the saturation is not clear, again, at low strain amplitudes.

Since it is believed that plastic strain is the controlling parameter in fatigue fracture (25) and those tempers tested here have

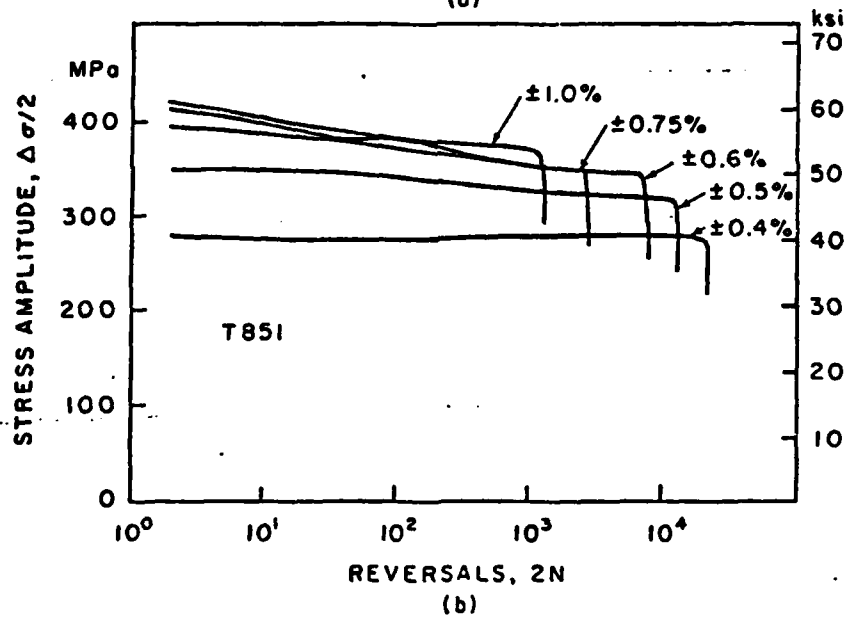
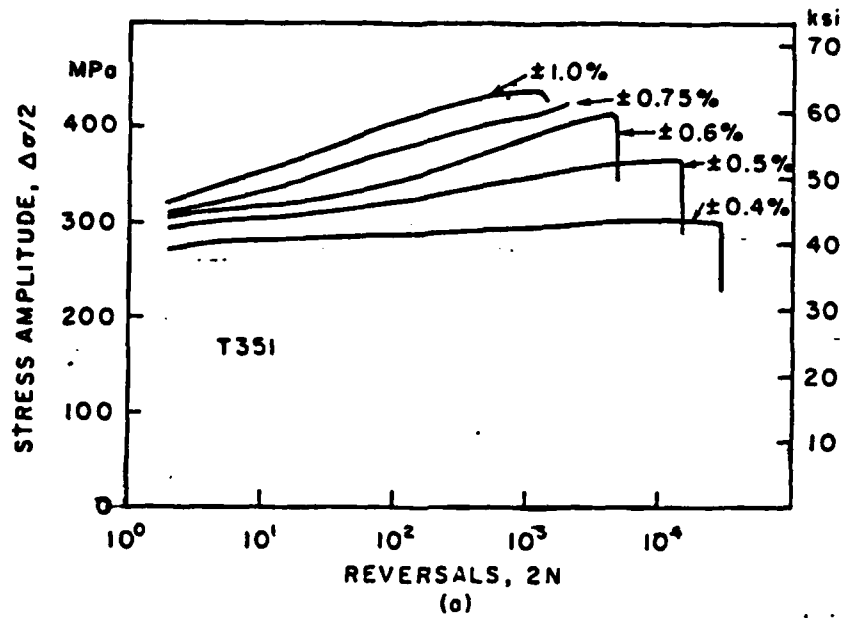


Figure 7: (Captions on next page)

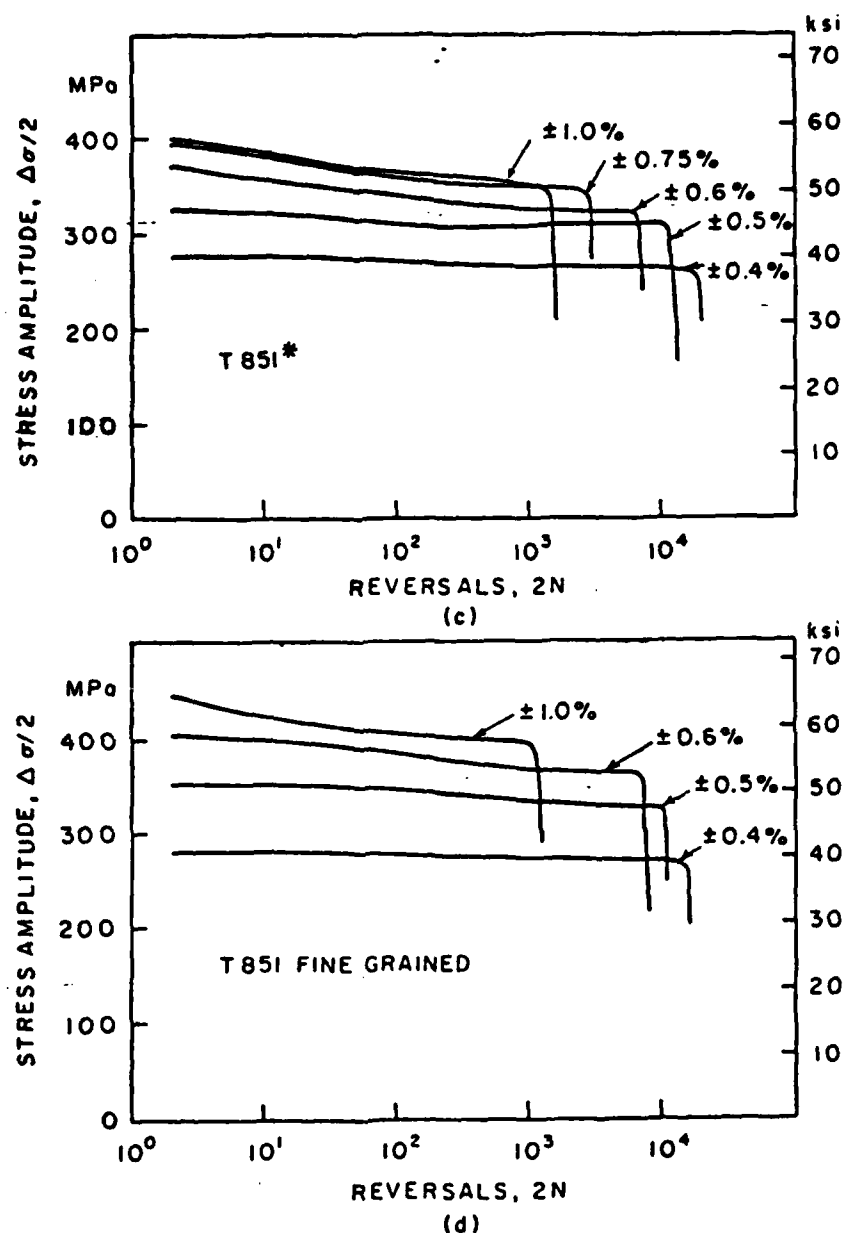


Figure 7: Cyclic response curves for different microstructures from total strain control tests. (a) T351 (b) T851 (c) T851* (d) Fine grained T851 temper. The constant strain amplitudes in percent, are indicated on the curves. Note that the cyclic stress amplitude was determined by taking average values of tensile and compressive peaks in each hysteresis loop. Only the T351 temper shows cyclic hardening behavior.

shown no distinct saturation but consistent cyclic hardening/softening behavior up to final failure, the constant plastic strain control test was performed. Figure 8 shows the typical hysteresis loops for the T851 temper of coarse grain material with the plastic strain amplitude of $\pm 0.5\%$. Slight wavy curves in these loops are due to the computer control which is able to command only the stepwise motion of loading ram. There is shown an interesting phenomenon in this figure; the unloading slope for elastic strain recovery was quite different from the initial loading elastic slope, probably due to reversed plastic flow even at positive stress and inelastic contribution to the strain amplitude (26). The difference was as much as up to 10% showing that the width of the hysteresis loop is smaller than the plastic strain amplitude programmed. In this experiment, the plastic strain amplitude was determined by the apparent width of the actual hysteresis loop rather than the plastic strain amplitude programmed by following a conventional method (27). The T851 and the T851* tempers again showed the doubly inflected curves, but not the T351 temper, though the T851* temper has slightly large curvature of convex portion in a compressive half. The cyclic straining response curves for different plastic strain amplitudes are plotted in Figures 9a, b, c, d with the number of reversals applied. They are similar to, but have slightly greater degree of hardening/softening behavior than those obtained from the total strain control tests. It should be noted that the plastic strain amplitudes shown are corrected values according to previous explanation.

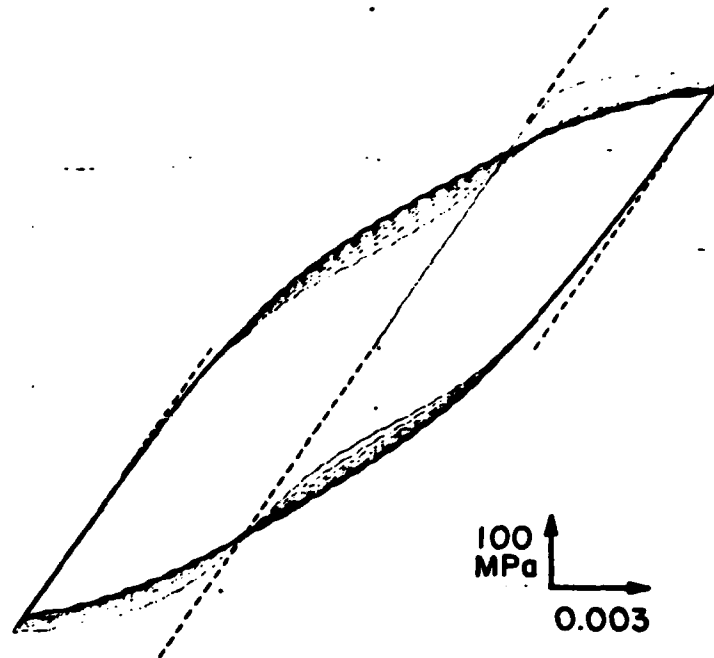


Figure 8: Hysteresis loops of 1 to 10 cycles taken from the plastic strain control test on T851 temper. The plastic strain amplitude was $\pm 0.5\%$. A slightly wavy curves are due to stepwise motion of loading ram by computer control. Note that the half widths of the hysteresis loops are smaller than the plastic strain amplitude, probably due to reversed plastic flow even at positive stress.

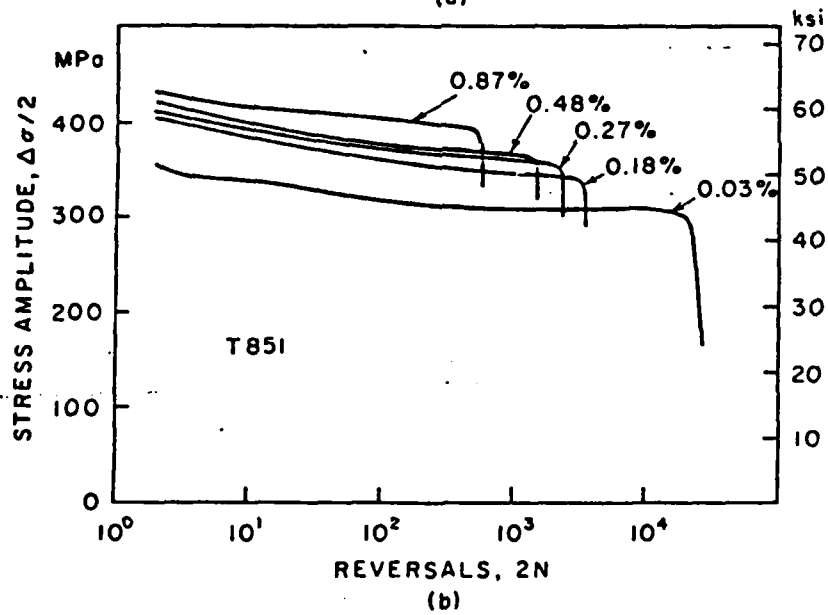
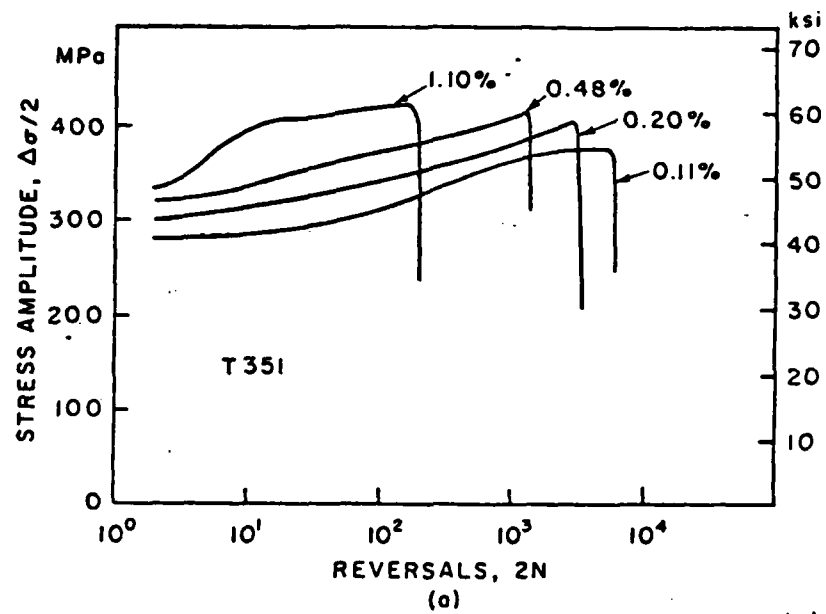


Figure 9: (Captions on next page)

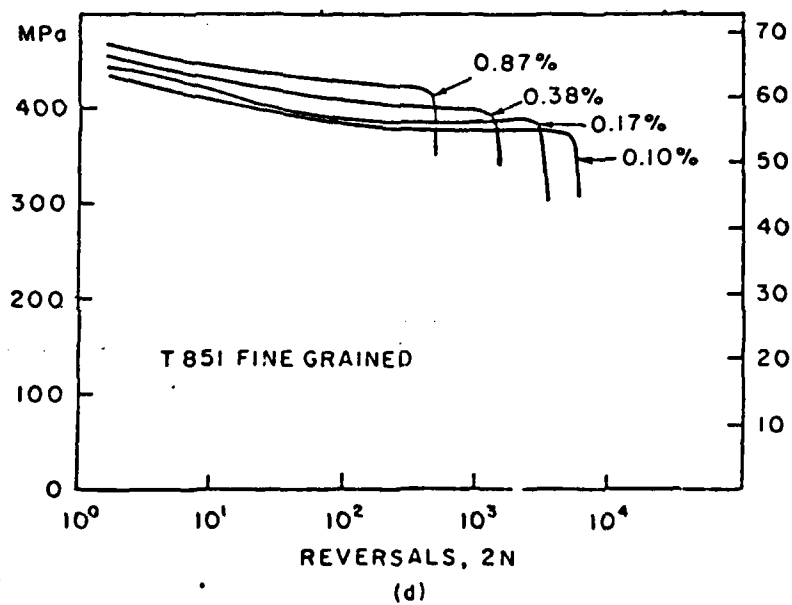
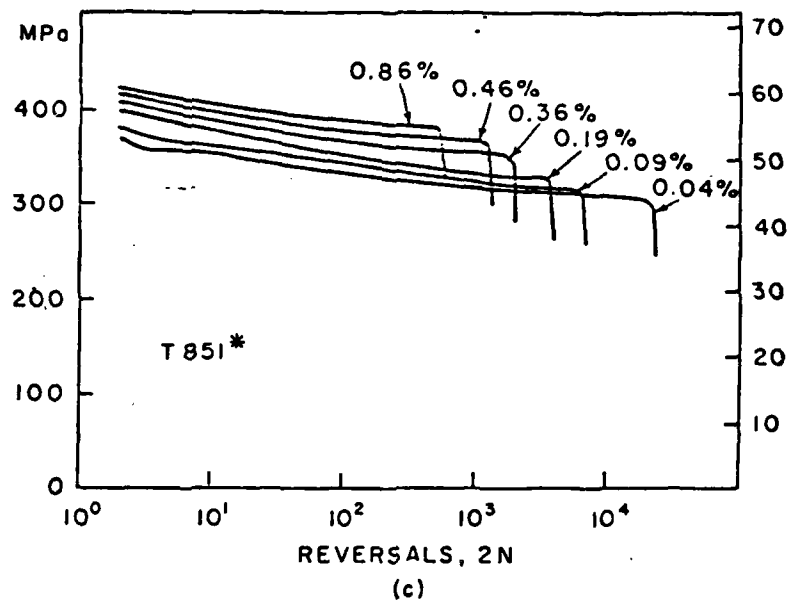


Figure 9: Cyclic response curves obtained from plastic strain control tests. (a) T351 (b) T851 (c) T851* (d) Fine grained T851 temper. The plastic strain amplitude in percent are indicated on the curves. These magnitudes are corrected values according to explanations in the text.

2.3.3 Fatigue Life Characteristic

The fatigue resistance to total strain cycling for any particular metal can be considered as the summation of its elastic and plastic strain resistance (28), hence

$$(\Delta\epsilon_t/2) = (\Delta\epsilon_e/2) + (\Delta\epsilon_p/2) = (\sigma'_f/E)(2N_f)^b + \epsilon'_f(2N_f)^c \quad (1)$$

where

- $\Delta\epsilon_t/2$: total strain amplitude
- $\Delta\epsilon_e/2$: elastic strain amplitude
- $\Delta\epsilon_p/2$: plastic strain amplitude
- σ'_f : fatigue strength coefficient
- E : Young's (elastic) modulus
- N_f : number of cycles to failure (=fatigue life)
- $2N_f$: number of reversals to failure
- b : fatigue strength exponent
- ϵ'_f : fatigue ductility coefficient
- c : fatigue ductility exponent

The first part of the above equation relates the elastic strain or stress amplitude to the number of reversals to failure. The second part of Eq. (1), called the Coffin-Manson equation (29,30), relates the plastic strain amplitude to the number of reversals to failure. A schematic representation of Eq. (1) is shown in Figures 10a, b.

It can be seen that at short lives the plastic strain component predominates, emphasizing the importance of ductility. At long lives

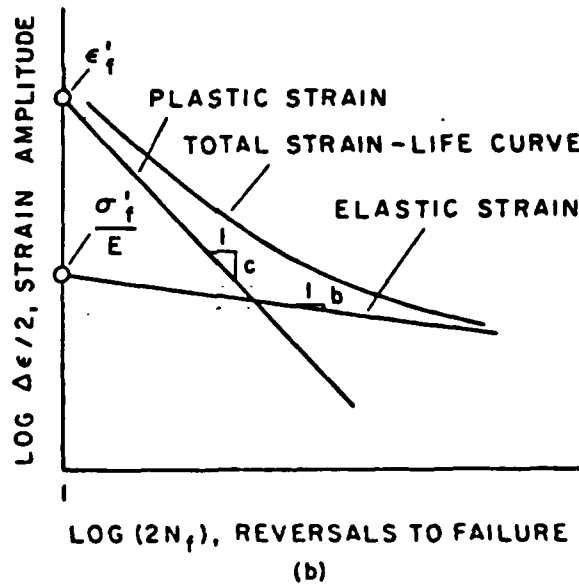
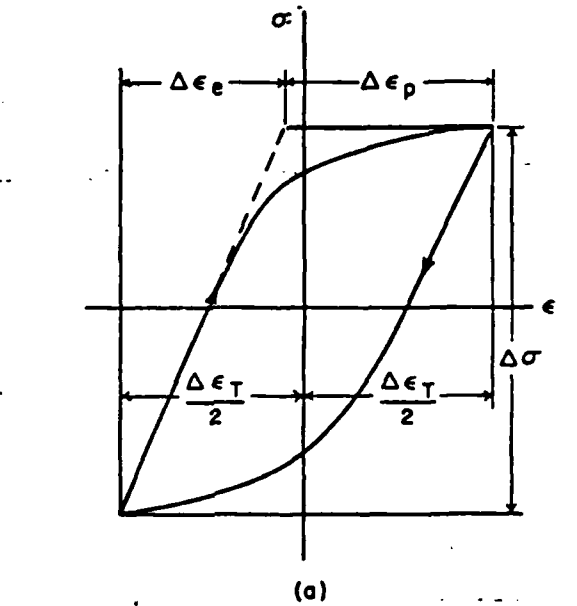


Figure 10: (a) Typical stress-strain hysteresis loop. Total strain can be divided into an elastic strain portion and a plastic strain portion.

(b) Typical strain-life curves for elastic, plastic and total strain amplitudes. For the notations, see text.

the elastic component becomes predominant, emphasizing the role of strength (17). However, due to the primary importance of plastic strain both in unidirectional plastic deformation and in fatigue, Coffin-Manson equation has been widely used. It has been attempted to relate the plastic strain resistance, ϵ_f' , with the monotonic fracture ductility, ϵ_f , shown in Table III, but no general agreement is found between the results reported.

The relations of the fatigue life vs. the strain amplitude applied are shown in Figures 11a, b, c, d in the form of a Coffin-Manson plot for all the tempers. In these figures, two kinds of plastic strains are plotted: one is the computed value at half life ($N_f/2$) during the total strain control tests and the other is the fixed value directly from the plastic strain control tests. These two values show significant differences, particularly for the T351 temper and in the small plastic strain range. The discrepancy could be partly due to the characteristics of materials in that they show no clear saturation but continuous hardening/softening behavior.

Sanders et al. (31) showed the deviation from the single slope of the Coffin-Manson plot in commercial aluminum alloys, and attributed them to changes in deformation processes as a function of the plastic strain amplitudes. They argued that slip is homogeneous at high plastic strains ($>10^{-3}$) and heterogeneous at low plastic strains ($<10^{-3}$) which turns into dual slope behavior. It should be noted that in their experiment, the plastic strain amplitude was computed from the total strain control tests with the values at half life. In the same way, when the computed plastic

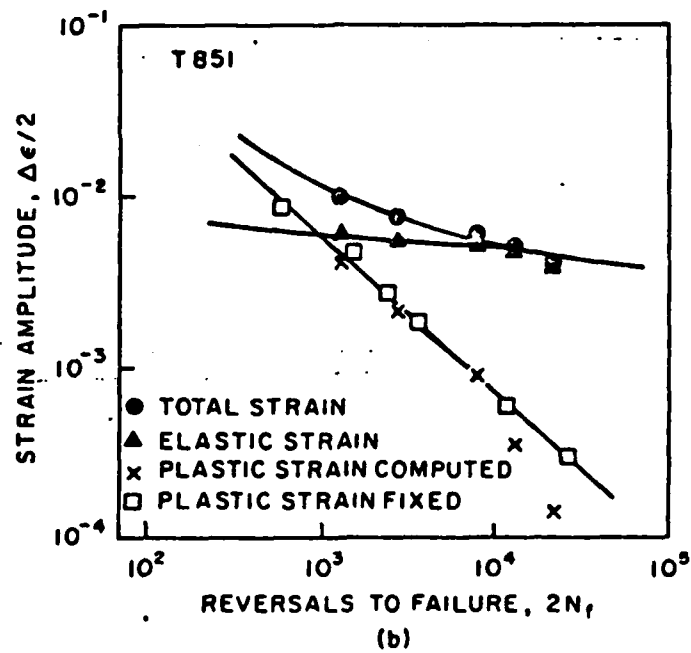
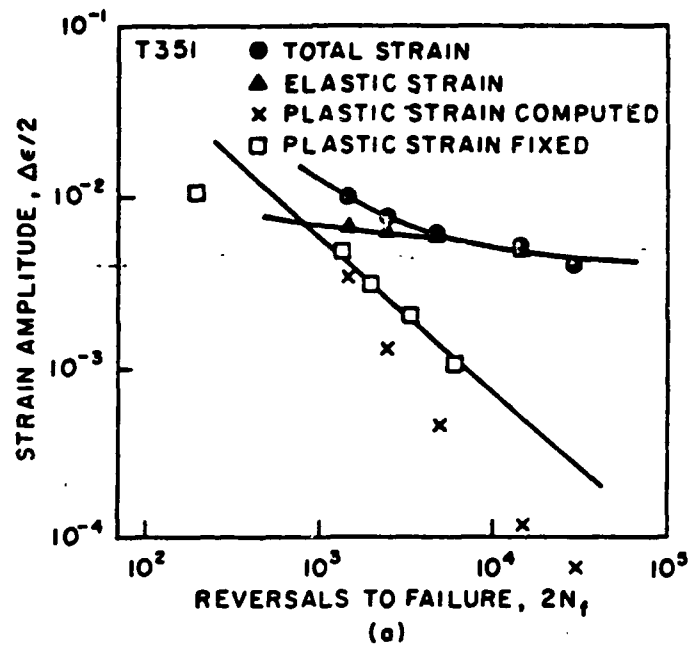
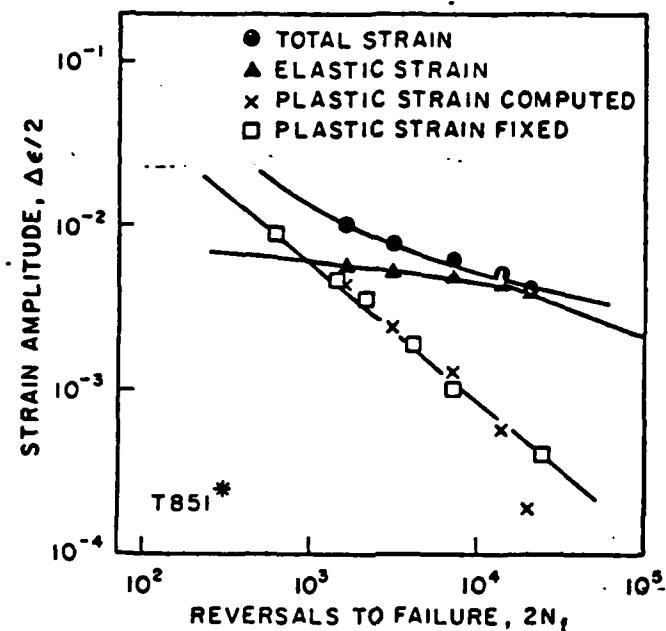
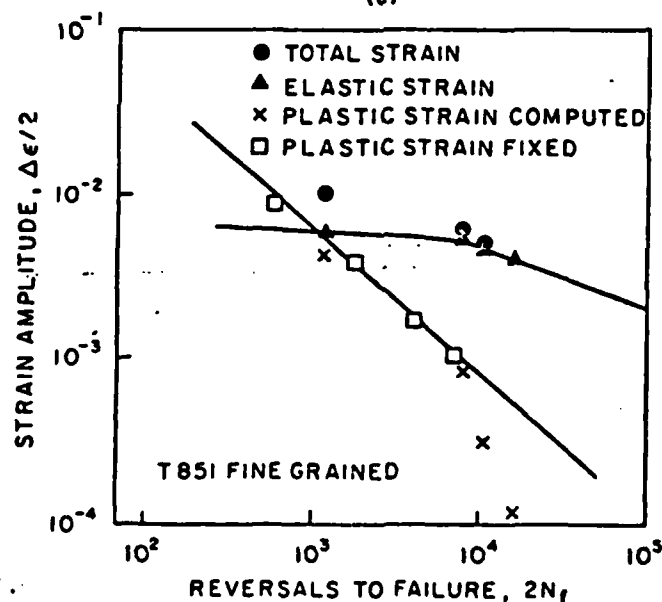


Figure 11: (Captions on next page)



(c)



(d)

Figure 11: Strain-fatigue life relations for different microstructures studied. (a) T351 (b) T851 (c) T851* (d) Fine grained T851 temper. In these graphs, the cross mark represents the computed plastic strain amplitude determined at half life in total strain control test, whereas the open square represents the fixed value from the plastic strain control test. Note that the T351 temper shows big difference between two values.

strain was plotted in these tests the multiple-slope behavior are clearly shown with the deflection point around 10^{-3} as in their results. On the other hand, the plot of fixed value from the plastic strain control tests shows a straight line of single slope. In these tests, the range of 10^{-2} to 10^{-4} plastic strains was studied. The above explanation is sufficient to prove the necessity of the plastic strain control test.

In order to compare the LCF resistance between different microstructures, the results only from the plastic strain control tests were plotted again in Figure 12. There is not significant difference among the T851, the T851* tempers of coarse grain materials and the T851 temper of fine grain material, whereas the T351 temper shows a slight, if any, inferiority to them.

2.3.4 Fracture Surface Morphology

The crack profile observed from the vertical cross sections shows that the cracking mode is entirely transgranular in all the microstructures studied. The fact that a number of small cracks were left only on the surface implies that the fatigue crack was mainly generated from the surface. The small cracks nucleated on the surface were subsequently linked up together and propagated to cause final failure. The higher the strain amplitude, the more generation of multiple surface cracks. On the same amplitude, the T351 temper shows more surface cracks than the other tempers. Figure 13 shows a cluster of surface cracks around the crack initiation site marked as "A" for the T351 temper tested in the plastic strain amplitude of $\pm 0.2\%$. It is interesting that the surface cracks were concentrated as a form of group around the initiation site and

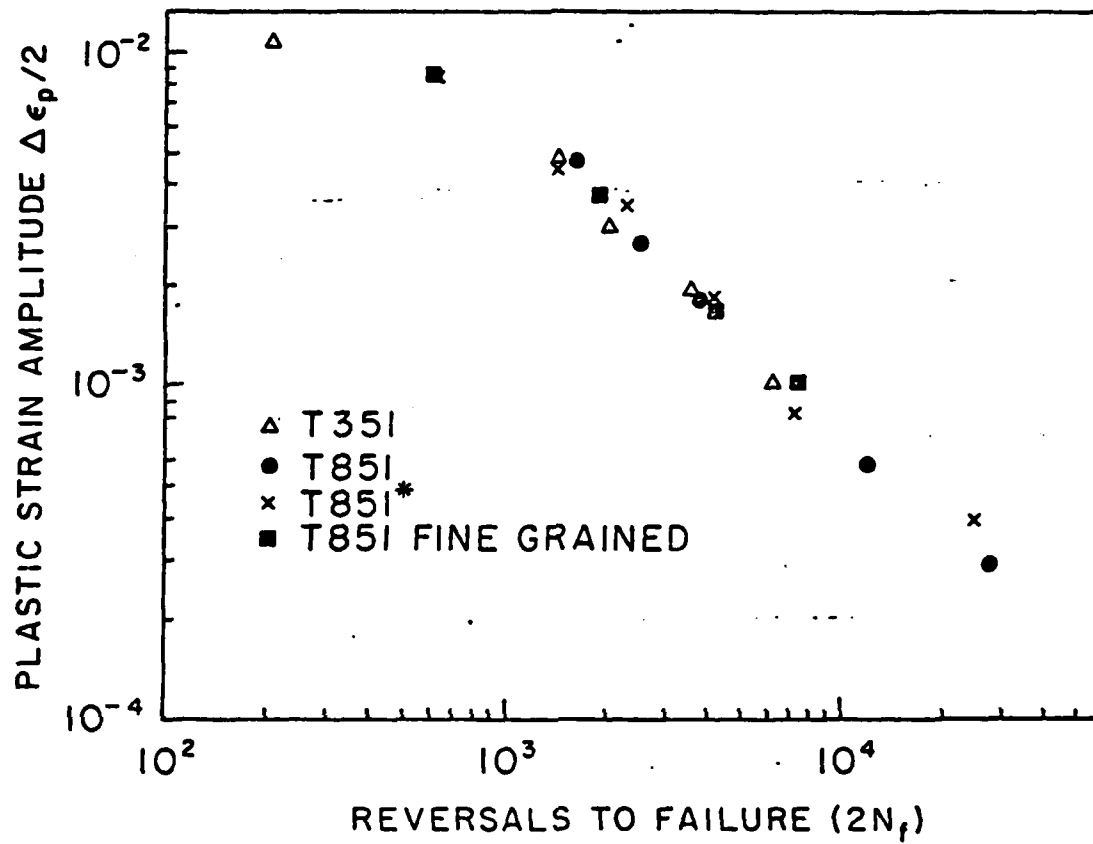


Figure 12: Fatigue life vs. plastic strain amplitude plot. Only the results obtained from plastic strain control tests were plotted to compare the LCF resistance of different microstructures.



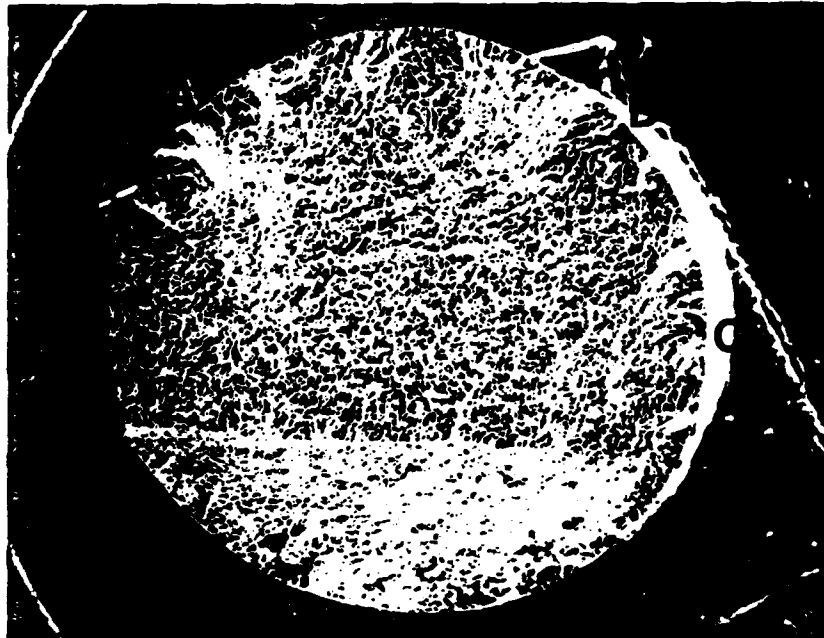
Figure 13: SEM photograph showing a cluster of surface cracks around the fatigue crack initiation site marked as A. Surface cracks are parallel to fracture surface and left chevron marks below the initiation site. From the T351 temper in the plastic strain amplitude of $\pm 0.2\%$. $\times 150$

parallel to main fracture surface leaving chevron marks on the surface.

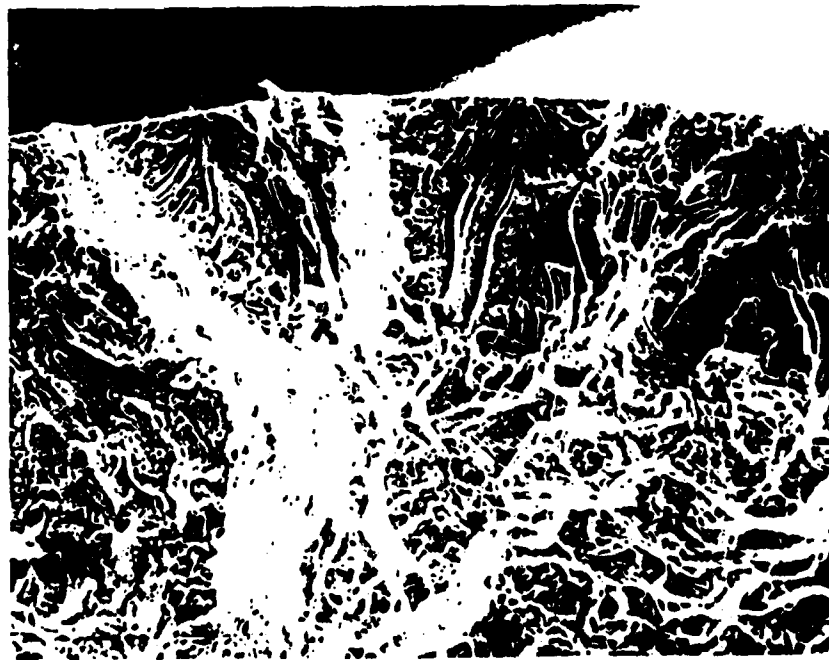
The examination of fracture surface under SEM revealed that the ductile tear ridges covered the whole fatigue fractured area and the multiple initiation site existed, shown in Figure 14a as an example. The multiple initiation sites A, B, C around the surface are again viewed at high magnification in Figures 14b, c, d. The initiation zone has the feathery markings which converge to its "eye" and the brittle appearance of cleavage fractures. This stage I fatigue does not display any characteristic fatigue striations due to the shearing mechanism. The initiation site frequently has a second phase inclusion on its eye as shown in Figures 15a, b, which indicates that the crack was initiated from these second phase particles. The analysis with EDAX shows that these inclusions are intermetallic compounds containing primarily the impurity silicon.

Stage II fatigue propagation is distinguished by striations, parallel plateaus and longitudinal ridges as shown in Figures 16a, b. The fine striations are running perpendicular to the crack propagation direction. At high crack growth rate, the secondary cracks were formed at the roots of many ductile fatigue striations shown in Figures 17a, b.

Around the end stage of fatigue, the fracture surface shows the mixed mode of ductile striations and intermingled dimples as shown in Figure 18. The final overloaded region which was failed by tensile rupture is covered with stretched zones and dimples associated with second-phase particles as shown in Figure 19.



(a)



(b)

Figure 14: (Captions on next page)

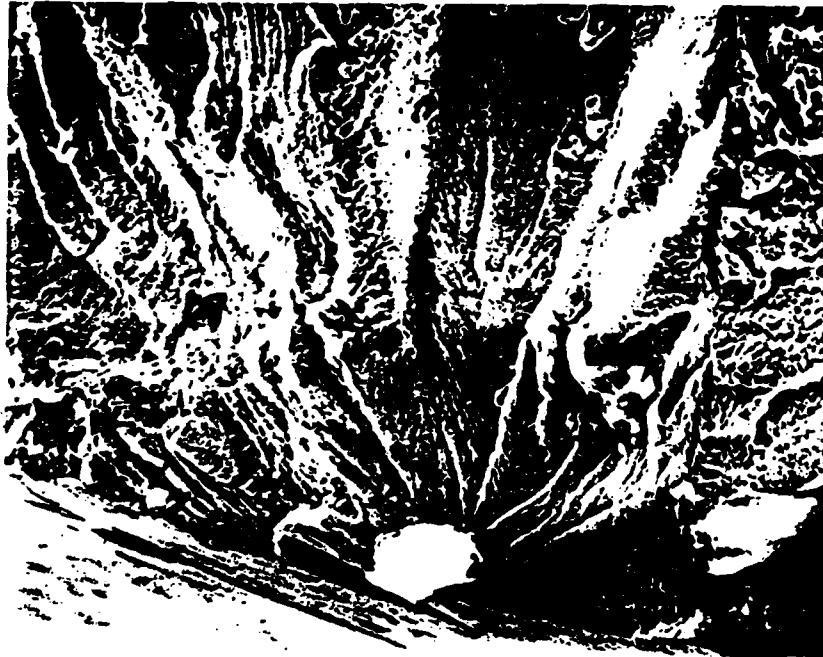


(c)



(d)

Figure 14: SEM fractographs taken from the T851* temper specimen tested at $\pm 0.5\%$ total strain amplitude.
(a) Multiple initiation sites are shown as A,B,C at low magnification (x15).
(b) Magnified view (x150) of A shows feathery marks emanating from nucleation eye.
(c) and (d) are higher magnification of B and C, respectively.



(a)

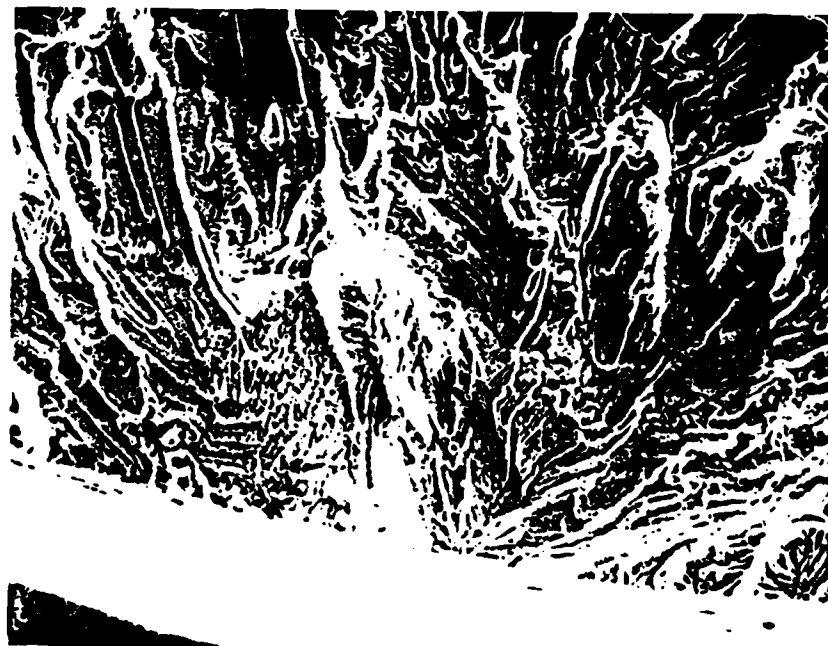


(b)

Figure 15: SEM fractographs showing large second phase inclusions on the initiation site.
(a) inclusion of $15\mu\text{m} \times 700$, T851 temper.
(b) inclusions of $20\mu\text{m} \times 400$, T 851 temper.
EDAX analysis showed that both inclusions are Si-bearing impurity particles.



(a)



(b)

Figure 16: Transitions from Stage I to Stage II characterized by (a) striations perpendicular to propagation directions or (b) steps. (a) also shows a small inclusion on the initiation 'eye' which turned out as CuAl_2 by EDAX analysis.



(a)



(b)

Figure 17: Fatigue Striations comprising secondary cracks at the roots.
(a) T851 temper at x1500 magnification.
(b) T851* temper at x900 magnification.

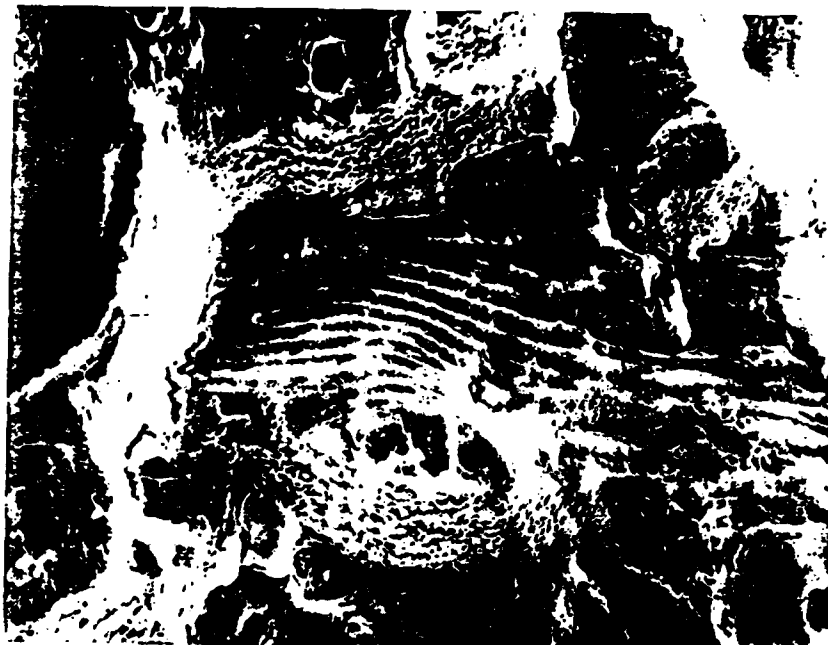


Figure 18: The end stage of fatigue shows the mixed mode of ductile striation and intermingled dimples.

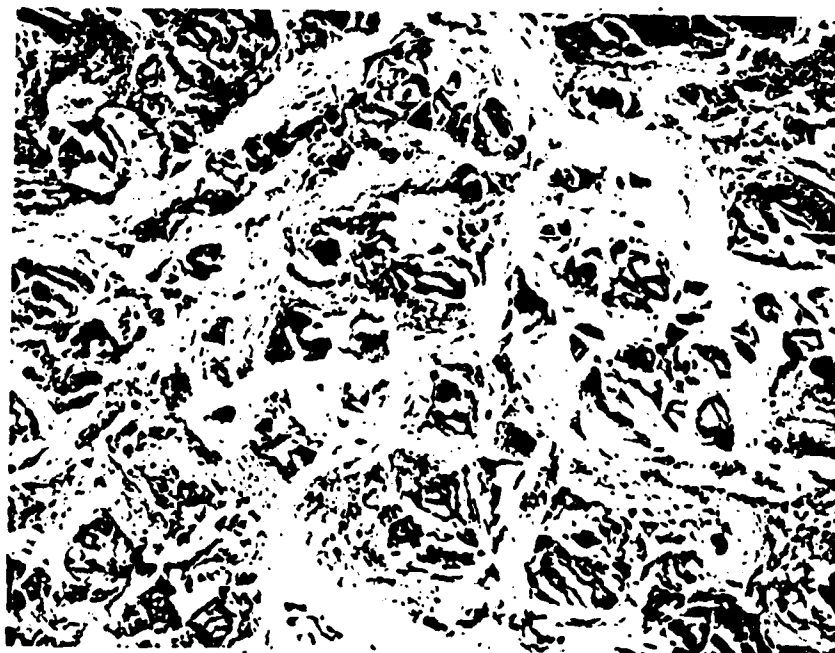


Figure 19: The final overloaded zone by tensile fracture shows stretched zone and dimples associated with second-phase particles.

III. 3. Crack Growth Under Uniform Loading

3.1 Introduction

This section describes procedures and some typical results obtained from a study of the micro and macromechanics of fatigue crack growth under uniform loading. Since the crack closure phenomenon is studied in much detail, its use in analysis of crack growth behavior along with experimental techniques to measure crack opening and growth rate are fully described. The descriptions include presentation of actual data and discussion of how the data is interpreted. This type of discussion is especially important in that the determination of crack opening load is not straightforward and requires explanation.

The emphasis has been put on the role of microstructure, including grain size and precipitate (dispersoid) type on the phenomena of crack tip closure, in fracture toughness and crack growth. The different microstructures studied were achieved through varying heat treatment. The result of this study shows that crack growth rates, following simple uniform loading histories, are lower in underaged microstructures than in either peak-aged or slightly overaged microstructures. In addition, it was found that grain size also has an important effect on crack growth in that increasing grain size tends to decrease crack growth rates and increase crack closure levels. On the other hand, this coarse grain size leads to a decrease in fracture toughness.

Any crack growth study requires the development of an experimental method for measuring small increments of crack growth. Implementation of the crack closure concept in particular, requires the development of an experimental technique to determine the magnitude of the crack tip

closure loads. The techniques developed to date can be classified into two main categories: those that measure bulk specimen response and those that measure opening displacements across the crack on the specimen surface. Bulk response measurements have been performed by interferometry methods for transparent polymers (32), electrical potential methods (33), and acoustic wave techniques using ultrasonics (11,34). Surface displacement measurements have been performed with displacement clip gauges at the notch (35), strain gauges bonded across the crack surface (36), displacement transducers attached ahead of the crack tip or across the crack surface (37) and by laser interferometry techniques (38).

In the present study of crack growth, we employed an extremely sensitive differential compliance technique, initially introduced by Paris and Hermann (7,39) and further developed by us (40) to measure closure loads and distances. This same technique was also used for monitoring changes in specimen compliance due to crack extension. We believe that this technique is superior to surface measurement procedures in that it provides a more realistic estimate of "through thickness" phenomena and is capable of detecting, at least in principle, crack length changes of less than 0.01 mm. Some discussion of the sensitivity of the technique is given in Section IV under the heading of Fractography.

3.2 Experimental

3.2.1 Differential Compliance Technique

When a specimen contains a crack, the compliance for a given position and direction of the load depends on the crack length. By elementary fracture mechanics for plane strain in Mode I (crack tip

opening mode), it can be shown that (40)

$$da = \frac{E}{2B(1-\nu^2)} \left(\frac{P}{K_I} \right)^2 dc \quad (2)$$

where da : change in crack length
 B : thickness of specimen
 ν : Poisson's ratio of specimen material
 P : applied load
 E : Young's modulus
 K_I : stress intensity factor in Mode I
 dc : change in compliance of the system

Also, for a compact tension (CT) specimen the stress intensity factor in Mode I can be expressed as

$$K_I = \frac{P}{B\sqrt{W}} f(a/w) \quad (3)$$

where P is the applied load, W is the width of the CT specimen and the polynomial function of geometry correction factor $f(a/w)$ is, for present purposes, taken as (41)

$$f(a/w) = \frac{(2+a/w)(.886+4.64(a/w)-13.32(a/w)^2+14.72(a/w)^3-5.6(a/w)^4)}{(1-a/w)^{3/2}} \quad (4)$$

for $0.2 \leq a/w < 1$.

It should be noted that the above polynomial expression is different from that of ASTM E399-72 (Standard Method of Test for Plane Strain Fracture Toughness of Materials)

$$f(a/w) = (a/w)^{1/2}(29.6-185.5(a/w)+655.7(a/w)^2-1017(a/w)^3+638.9(a/w)^4)$$

(5)

which is valid only for range of relative crack length, a/w , from 0.45 to 0.55.

The above equations (2)-(4) illustrate how, from changes in compliance changes in crack length and crack opening and closing load can be determined. It was found that crack length changes of the order of at least 0.01 mm can be detected by amplifying the electrical signal representing only compliance changes. This is done by electronically subtracting an elastic displacement signal, δ_{Elastic} , computed from the actual load and by assuming a crack with a given length from the actual load point displacement signal δ_{Actual} . This yields a "differential displacement", $\Delta\delta = \delta_{\text{Actual}} - \delta_{\text{Elastic}}$, where δ_{Actual} is, again, the measured load line displacement and δ_{Elastic} is electronically computed (39) and is linearly proportional to the load. Since the load line displacement is proportional to the actual elastic compliance, the change dc , of the elastic compliance is obtained. The schematic diagram of the electronic system is shown in Figure 20.

Figures 21a-d show some typical data on crack growth and closure for a specimen with a slightly overaged condition. The records are a matching set with the letters A, B, C, . . . etc., corresponding in all four figures.

Figure 21a is the record of load versus actual load line displacement for a growing crack. These records, especially after that labelled "K", clearly show decreasing slope, indicating crack growth, and a bilinear

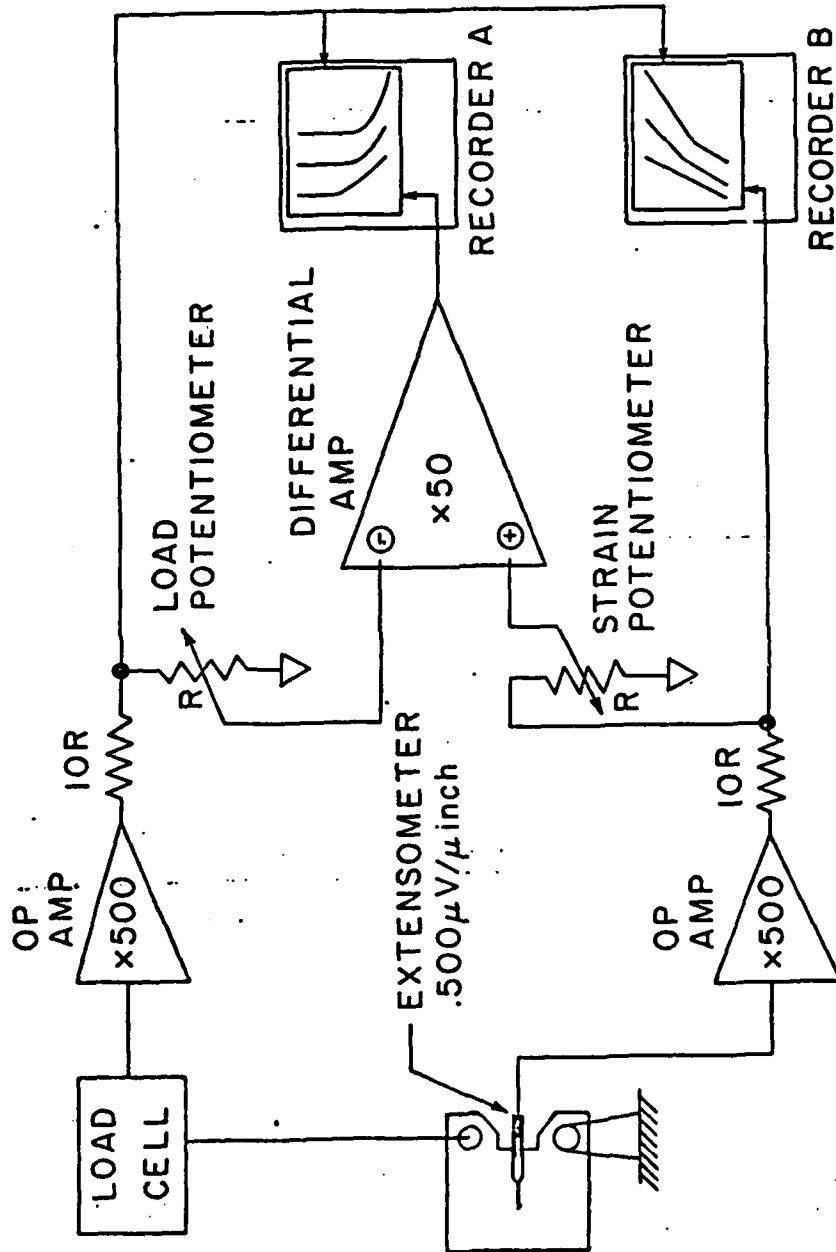


Figure 20: Block diagram of differential compliance system.

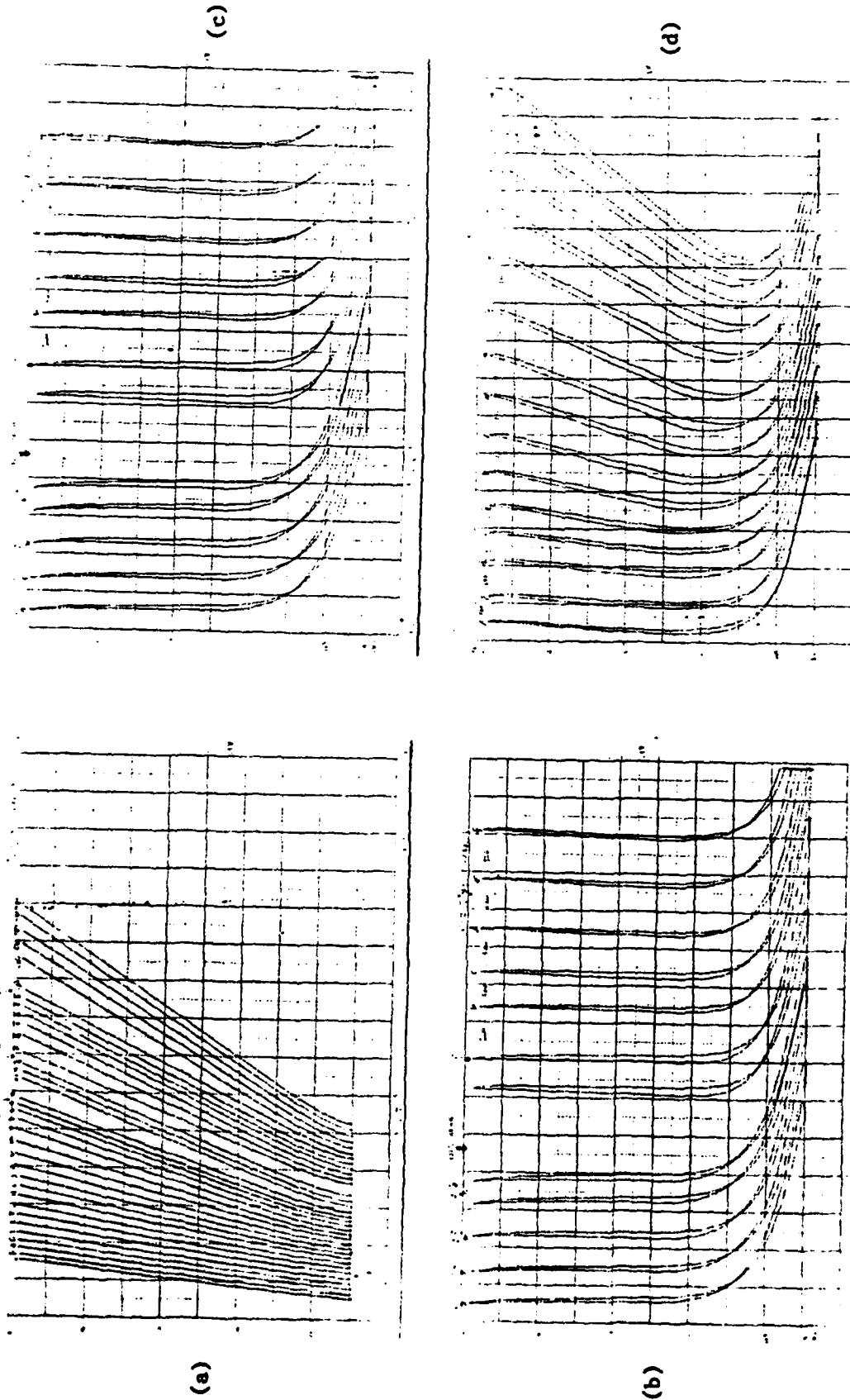


Figure 21: Photographs of unreduced data as plotted on X-Y recorders in the laboratory.
(a): Recorded curves of load vs. load point displacement.
(b): Recorded curves of load vs. differential displacement for uniform loading.
(c): Same as (b).
(d): Same as (b) and (c) after a single cycle overload.

form which indicates crack tip opening. That is, at low values of load the records are linear indicating a well defined elastic compliance determined by the crack with its tip closed - at higher loads the records are again linear but with a reduced slope. This reduced slope, or increased compliance is related to an apparently "larger crack length" at higher loads than that which determines compliance at the lower values of load. One obvious problem in attempting to measure an opening load from the records of Figure 21a is the difficulty in determining the precise load at which the slopes change.

Figures 21b and 21c represent typical data of load versus differential displacement. In this case the crack length assumed for computing δ_{Elastic} was the fully opened crack - at this value of crack length $\delta_{\text{Actual}} = \delta_{\text{Elastic}}$ and the load vs $\Delta\delta$ records become vertical. The search for this vertical record is, in fact, the means of determining this fully opened crack length. The values of load when the records of Figures 21b and 21c become vertical also provide an accurate measure of the crack tip opening load. The typical records shown indicate that opening loads can be determined with relatively little uncertainty. Figure 21d is a collection of load vs $\Delta\delta$ records following an overload and will be discussed in the next section.

For the differential compliance scheme described here to be effective, the loading and unloading curves, such as shown in Figures 21a-d, as examples, must be essentially free from hysteresis. This has been accomplished by using the special gripping fixtures made of an ultra high strength maraging steel shown in Figure 22a. As illustrated by the

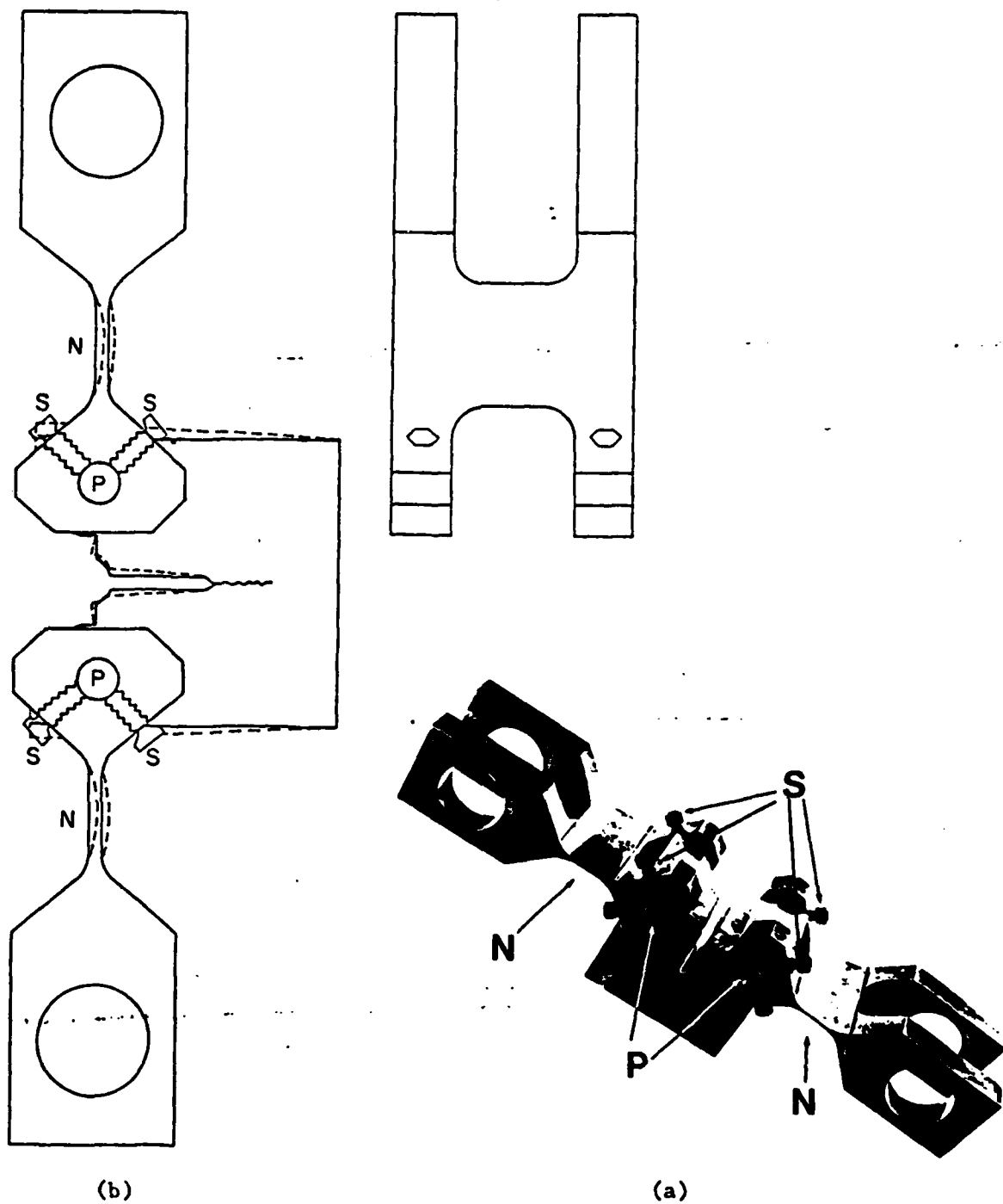


Fig. 22: "Frictionless grips" used for compliance measurements.

- (a): A view of compact tension specimen and hanger plates with labelling corresponding to that in (b).
- (b): Schematic diagram of bending of a specimen and of compensating flexing of hanger plates for the grip configuration shown in (a). N indicates the flexible necked-down sections of the hanger plates, P indicates the loading pins and S indicates the set screws used to prevent rotation of specimen about the pins.

dashed line in Figure 22b when a deeply cracked compact tension specimen is opened the motion is essentially bending. In the grip shown this rotation is accommodated almost entirely by elastic flexing of the machined thin gage hanger plates at points N. This thin gage section N should, therefore, have area large enough to transmit the load to specimen purely elastically. Another possible rotation about the specimen pins at P is nearly eliminated by fixing the grips to the specimen pins with the set screws S to further minimize friction and hysteresis.

3.2.2 Materials and Equipment

The 2048 aluminum plate used for these tests was the same as that for LCF tests. The chemical composition and the temper (ageing treatment) designation are contained in Section II. The residual-stress relieved (see Note 1) and tempered plates were machined to 25.4 mm (1 inch) or 12.7 mm (1/2 inch) thick, 51 mm (2 inch) wide modified CT specimen whose dimensions are shown in Figure 23. The grain orientation of these specimen is such that the loading axis is parallel to the rolling direction A with the crack's plane parallel to face B and its front parallel to edge C as shown from Figure 1 in Section II. The modification of specimen were made to permit direct measurements of load line displacements by making a step into the specimen on which razor edges were glued.

Note 1. It should be noted that for 25.4 mm thick CT specimens, the residual stresses induced by quenching can have a significant effect on the mechanics of crack growth (40). Fatigue tests performed on as quenched and age-hardened specimen without residual stress relief, showed a marked retardation of crack growth due to the compressive stresses on the specimen surface. In addition, the fracture surface revealed a characteristic "black fretted region" which was not observed in the stress relieved fatigue specimens.

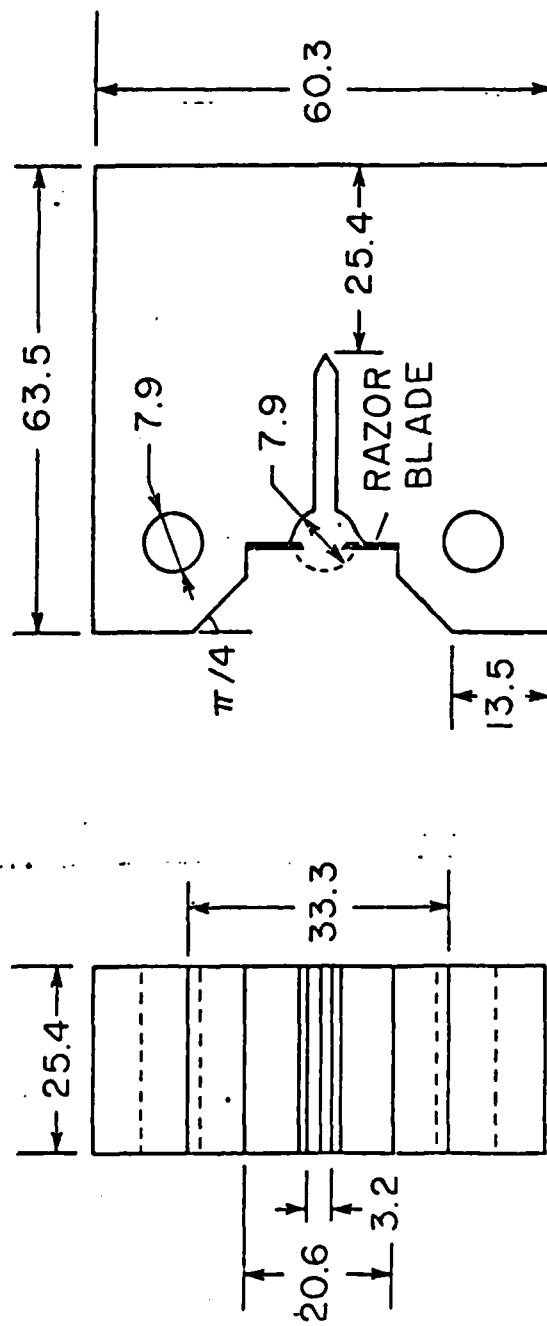


Figure 23: Dimensions of our modified compact tension specimens. (unit : mm). Note that the modified specimen has the razor edges on its load line to measure the load-line displacement.

In fatigue crack propagation tests the specimens were loaded sinusoidally under pull-pull constant amplitude load (with one exception to be discussed later) at 35 Hz on an Instron closed loop servo-hydraulic test machine. R , the ratio of minimum to maximum load in a loading cycle, has the range from 0.1 to 0.3. All load and displacement signals were plotted autographically on two X-Y recorders by controlled loading at a reduced frequency of 0.3 Hz.

Plane strain fracture toughness (K_{Tn}) measurements were performed on 25.4 mm thick CT specimens of the same configuration as those used for the crack growth tests. CT specimens of different microstructures were pre-cracked under final maximum load of 3.6 kN and R ratio of 0.05 until a/w was less than 0.55 by following ASTM E399-72 test procedures. Finally, the longitudinal transverse (L-T) fracture toughness value obtained was examined for the validity as an K_{IC} value. The K_{IC} test is valid if the specimen thickness is greater than $2.5 (K_{IC}/\sigma_y)^2$, which means small scale yielding at crack tip. Both crack propagation and fracture toughness tests were performed at room temperature in dry laboratory environments.

3.3 Results

3.3.1 Crack Closure Behavior

Elber (5) originally showed by experiment that crack closure was a direct consequence of the permanent tensile plastic deformation left in the wake of the propagation crack. As a result of this deformation, the compressive residual stresses due to incompatible mating fracture surfaces will close the crack, reducing the effective load to grow the

crack. In the present test, the distinct closure phenomena occurred in both 25.4 mm thick and 12.7 mm thick specimens. There were no significant differences in the relative magnitudes of closure loads for either the 25 mm or 12.7 mm thick specimens for a given microstructure. This implies that the closure is not only a surface effect due to greater stretch in plane stress region but a general phenomenon in plane strain condition as well.

The closure behaviors for all the different microstructures studied are illustrated in Figure 24 by plotting of opening level, K_{open}/K_{max} ($=P_{open}/P_{max}$), versus normalized crack length, a/w . The result for 2048-T351 taken from the work of Paris and Hermann (7) is also included for comparison. The crack opening level was directly determined from the differential compliance curves, already shown in Figure 21b, c. Usually, the opening load was slightly higher than the closing load and the average value was taken for plotting.

Elber claimed (6) that the closure level was approximately constant and only depends on the stress ratio R during his test with the thin plate center-cracked specimen of aluminum 2024-T3, implying that the closure was independent of the crack length or stress intensity factor K . In the present study, however, the closure level displays some complicated trends as a function of the range of applied stress intensity and the phenomenology of closure was significantly affected by microstructure, too. For constant amplitude loading, there was an evident transition from high to low closure level for all microstructures studied. At low K_{max} levels prior to the transition, the closure level was consistently

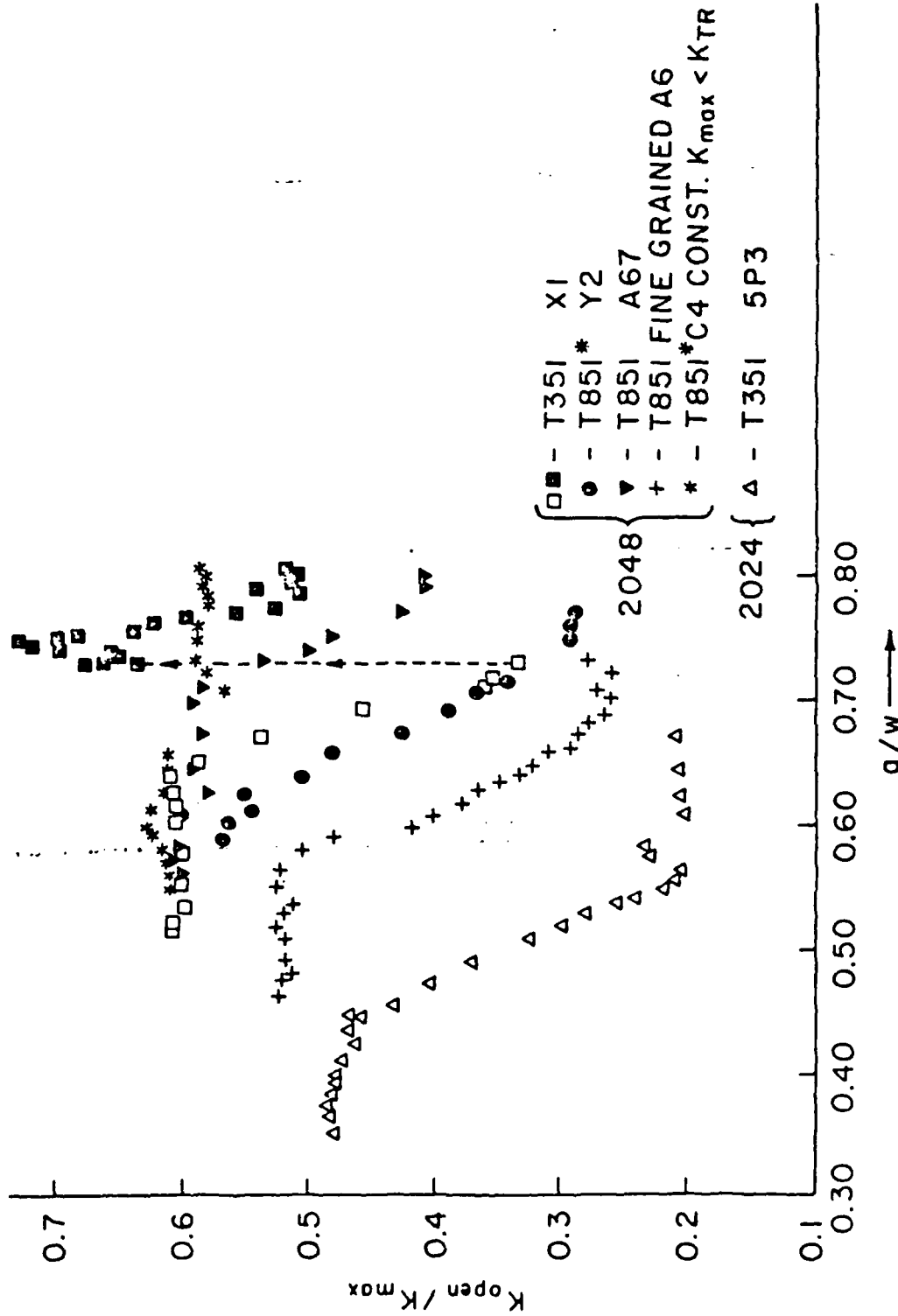


Figure 24: Fatigue crack closure in coarse and fine grain 2048 aluminum represented in terms of the ratio K_{open}/K_{max} versus normalized crack length a/w . Closed squares represented a test involving load reductions following the transition from high to low closure which shows increasing closure behavior. Note that there is no apparent transition in the case of constant $K_{max} < K_{TR}$, as shown with asterisks.

high and close to Elber's result, whereas at high K_{max} in post-transition, closure level dropped down to almost half of pre-transition value.

To investigate the transition behavior, the load level, crack length and K_{max} levels at the transitions are compared. As an example, the result shown in Figure 24 on the T351 (specimen X1) and T851 (specimen A67) tempers are from tests run at maximum load of 3.34 kN and 2.67 kN respectively, both on 25.4 mm thick specimen K_{max} levels at transition were $9.6 \text{ MPa}\sqrt{\text{m}}$ and $10.9 \text{ MPa}\sqrt{\text{m}}$ with a/w values of 0.64 and 0.71, respectively. In fact this was about the largest divergence in observed K_{max} transition levels; the values from seven additional such tests, four of which are on 12.7 mm thick specimens are listed in Table IV. For fine grained T851 temper, though, the test run at the maximum load of 4.45 kN showed the transition at an a/w of about 0.58 with K_{max} of $10.0 \text{ MPa}\sqrt{\text{m}}$. The transitions are evidently not simply functions of specimen compliance (i.e., geometry, including crack length) but appear to occur within a narrow K_{max} range which can be seen from Table IV.

Another noteworthy aspect of the observed closure behavior is its dependence on microstructure including grain size and the effect of ageing treatment. The closure loads were higher, especially at low K_{max} levels, for the coarse grained microstructures compared to the fine grain material including 2024-T351 as shown in Figure 24. There was also a general trend for the underaged microstructures at a given grain size, to display larger closure load, again, at the lower K_{max} levels. By bearing the grain size dependence of transition in mind, the computed plastic zone sizes at the K_{max} transition levels are compared with the measured grain widths; the results are also contained in Table IV. The

TABLE IV
K_{max} Value and Plastic Zone Size Computed at Transition

Specimen	Thickness mm	L _{max} kN	R	K _{max} (tr) MPa-√m	a/w(tr)	temper	grain size mm	r _p (mm)
<u>2048</u>								
A6	25.4	4.45	0.10	10.0	0.58	T851	0.063	0.082
A67	25.4	2.67	0.17	10.9	0.71	T851	0.19	0.158
XI	25.4	3.34	0.13	9.6	0.64	T351	0.19	0.212
YI	25.4	2.45	0.18	9.3	0.69	T351	0.19	0.202
Y2	25.4	3.34	0.13	9.7	0.64	T851*	0.19	0.169
X5	12.7	1.67	0.27	11.0	0.67	T3	0.19	0.280
Y5	12.7	1.78	0.13	10.2	0.65	T3	0.19	0.242
X6	12.7	0.98	0.23	8.2	0.72	T8*	0.19	0.123
Y6	12.7	1.69	0.13	9.9	0.65	T8	0.19	0.177

r_p is the computed plastic zone size at the transitions and d the average grain width measured on face B of Figure 1. The asterisk indicates a slightly overaged temper of 190°C for 24 h as opposed to 190°C for 12 h for T851.

correlation suggests that the transition occurs when the computed plastic zone size extends fully over at least one grain. The suspicion that this transition may be as much a material effect as a specimen compliance effect suggested two additional experiments.

In the first test a crack was grown, to an a/w of 0.80, with a nearly constant K_{max} less than the transition level. This was accomplished by continually reducing the load. The results are also shown in Figure 24 by the asterisks. Although there is a slight decrease in the value of K_{open}/K_{max} , the pronounced "transition" evident in the other tests appears to be absent. A second test, designed to test the reversibility of the transition, was run with a constant load amplitude of 3.34 kN on a 25.4 mm thick specimen until the transition was nearly complete; ΔK at this point was about $14.7 \text{ MPa}\sqrt{\text{m}}$. The load was then continually shed off so as to maintain a constant ΔK of $8.0 \text{ MPa}\sqrt{\text{m}}$ which was below the $9.6 \text{ MPa}\sqrt{\text{m}}$ transition value. The test is represented by the open and subsequently closed squares in Figure 24 which shows that the ratio K_{open}/K_{max} went through a transient increase. This behavior certainly suggests that the crack closure behavior had returned to what it was before the transition.

3.3.2 Fatigue Crack Growth

During recent years most of fatigue crack growth results have been analyzed using the Paris empirical relation (13) between the crack growth rate, da/dN , and the stress intensity factor range, ΔK , as a form of power law $da/dN = C(\Delta K)^m$ where C and m are empirical constants depending on the given material. Based on the closure concept, however, the

modified form of power law $da/dN = C'(\Delta K_{eff})^{m'}$ was suggested.

Following the above relations, some typical results for crack growth rates versus both applied ΔK and computed ΔK_{eff} are given in Figure 25 for the three different ageing conditions T351, T851 and T851*. When the modified power law $da/dN = C'(\Delta K_{eff})^{m'}$ is adopted, the values of C' and m' are 9.6×10^{-11} and 3.7 for T351, 7.3×10^{-10} and 2.8 for T851, 3.2×10^{-10} and 3.0 for T851*, respectively. It should be noted that all the results shown in Figure 25 were obtained under the same conditions, that is, uniform loading with same K_{max} , R ratio and environment. The maximum load amplitude of 2.2 kN and minimum of 0.2 kN was applied which ensured the plastic strain condition for 1 inch thick specimen. The results show that over most of the intermediate ΔK range the lowest growth rates were observed in the T351 temper. A possible explanation for this to be discussed later may be provided by the tendency for underaged microstructures in precipitation hardened materials to display heterogeneous deformation characterized by localized shear bands. This, in turn, leads to out-of-plane shearing, a rough fracture surface morphology, and a reduced rate of crack growth.

Another noteworthy observation of the present study, as discussed in an earlier report (40) is a reduction in growth rate with increased grain size, which seems consistent with a general trend found in recent literature. It was shown therein that, over a wide range of ΔK , the growth rate for the fine grained material was slightly higher than for the material we heat treated and which underwent recrystallization and grain growth.

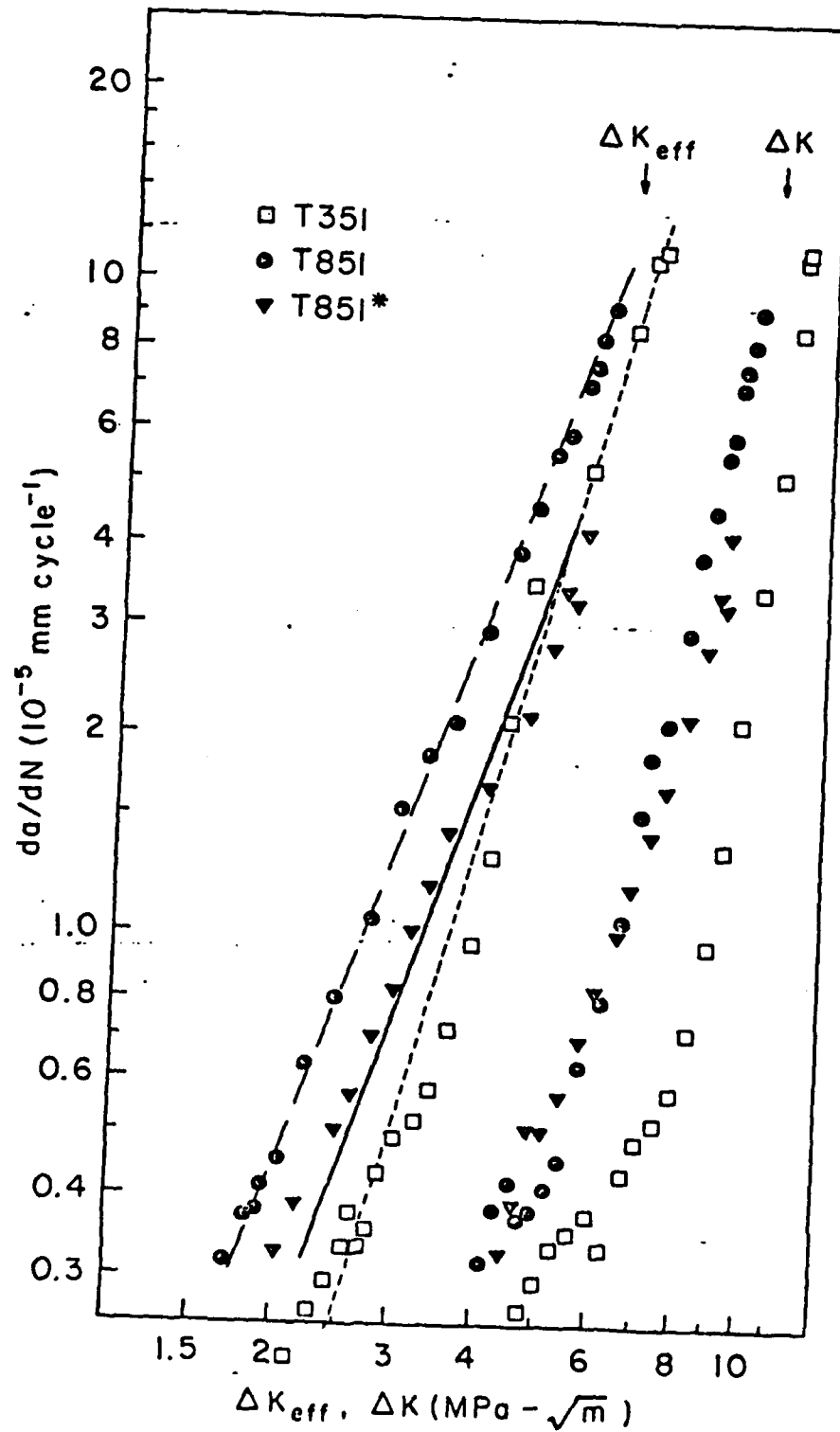


Figure 25: Typical crack growth rate data for three different tempers represented in terms of ΔK and ΔK_{eff} .

3.3.3 Fracture Toughness

The longitudinal transverse (L-T) plane strain fracture toughness results are given in Table V along with the validity examination for all microstructures studied. The load-crack opening displacement curves obtained during the tests are shown in Figure 26 indicating the P_Q values which are determined from the intersection point of the secant lines from origin with slope of 0.95 linear part and the individual curves. For the K_Q values, converted from P_Q by using Equations (3) and (5), to be considered as the valid plane strain fracture toughness, K_{IC} , the following conditions should be satisfied:

$$\frac{P_{\max}}{P_Q} \leq 1.10 \quad (6)$$

$$B \geq 2.5 \left(\frac{K_Q}{\sigma_{ys}} \right)^2 \quad (7)$$

where P_{\max} is the maximum load achieved in the curves of Figure 26, B is the thickness of specimen and σ_{ys} is the 0.2 percent offset yield strength.

As shown in Table V, the first condition of Equation (6) was met for all microstructures, whereas the second condition of Equation (7), however, was not met for the T351 temper but for the other tempers due to the low yield strength and high toughness of the T351 temper. This means that the crack tip plastic region of T351 tempered material was too big compared to the crack size and specimen dimensions in the constraint direction to make its fracture toughness valid for K_{IC} . By ASTM criteria,

TABLE V
Plane Strain Fracture Toughness (K_{IC}) at Room Temperature

Temper	Orientation (1)	P_{max}/P_Q	(2) $B \geq 2.5 K_Q^2 / \sigma_{ys}^2$ (mm)	K_{IC} MPa- \sqrt{m}	σ_{ys} (MPa)	ϵ_f
T351	L-T	1.09	61.0	47.9 [†]	303	0.24
T851	L-T	1.08	18.0	34.8	410	0.15
T851*	L-T	1.02	16.1	31.8	397	0.12
Fine grained T851	L-T	1.02	17.5	37.5	446	0.17

(1) According to crack plane orientation identification code in ASTM E399-72. First letter indicates direction of applied stress and second letter the direction of crack propagation. L = Longitudinal T = Transverse

(2) Minimum thickness requirement to be valid K_{IC} . σ_{ys} is the 0.2 percent offset yield strength.

[†] Not valid for K_{IC} because the specimen thickness was 25.4 mm.

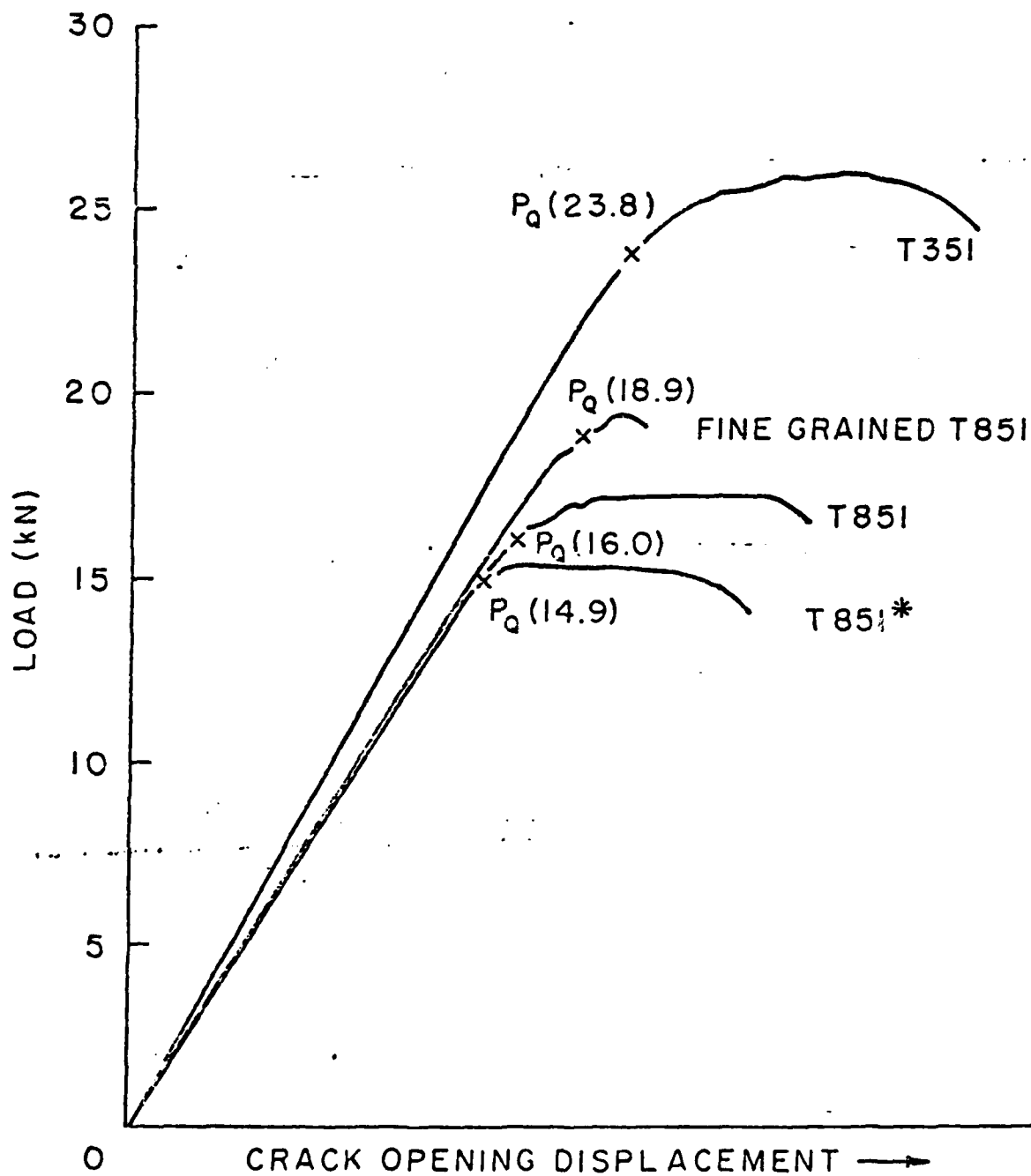


Figure 26: Load-crack opening displacement curves for different microstructure tested. The steeper linear slope for T351 temper is due to short crack length. P_Q , the intersection point of curve and .95 of linear slope, is used for the calculation of K_{IC} value.

therefore, the minimum thickness requirement for this material was calculated to 61 mm which seems to be difficult to meet in practice. Consequently, K_{IC} value for T351 temper is not strictly the characteristic parameter of material, but still has good meaning for the purpose of comparison with the other tempers. The test results show that the highest order of fracture toughness is coincident with that of ductility. In other words, the fracture toughness of material seems to depend on its ductility, not the yield strength level. In the aspect of grain size dependence of fracture toughness, the fine grained material shows superiority to the coarse material. The results of the present study, however, comprise that the ageing condition is a more contributing factor than the grain size difference. It is worth mentioning that the K_{IC} value of $37.5 \text{ MPa}\sqrt{\text{m}}$ for fine grained T851 temper is quite higher than that of $24.2 \text{ MPa}\sqrt{\text{m}}$ for 2024 aluminum, or than that of $30.8 \text{ MPa}\sqrt{\text{m}}$ for 2124 aluminum (42) which is another high purity version of 2024 aluminum but still has high volume percentage of second phase particles compared to 2048 aluminum.

3.3.4 Fractography

Examination of sectioned specimens with optical microscopy revealed that crack propagation was predominantly transgranular in all microstructures. There were numerous microbranches left by the running crack until the transition in closure behavior was reached but few branches seen on the post-transition portion, as shown by the optical micrograph provided in Figure 27. Examination of the fracture surface under low magnification, or with the naked eye, revealed a marked difference, especially distinct



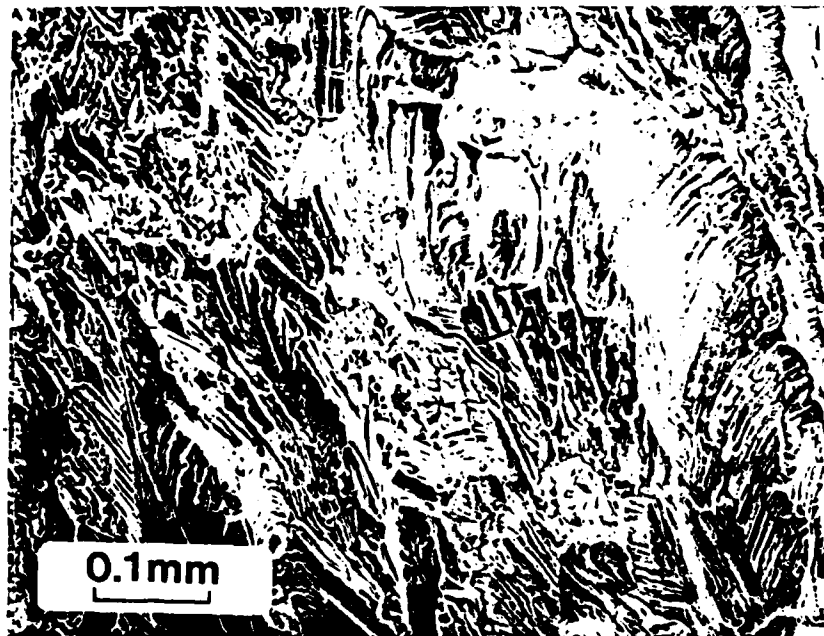
Figure 27: Optical microscopy of fatigue crack profile showing a number of micro-branches prior to the transition point which is indicated by the arrow.

in the T351 temper condition, between the pre-transition zone in closure, and the post-transition zone. The pre-transition zone had a very rough surface, whereas the post-transition fracture surfaces were much smoother. It was also observed that a number of secondary cracks parallel to the specimen surface (shown by the scanning electron fractograph provided in Figure 28a) were formed on the post-transition zone. These observations imply that there could well have been a change in the mode of crack growth. When the fracture surface was investigated by SEM, no distinct evidence of mode change could be observed except that the debris on the fractured surface was gradually decreased along the transition consistent with the decrease in the density of microbranches. A typical view of the fracture surface is shown in Figure 28b. The label "B" in Figure 28b shows the fragment formed by crushing due to residual compressive force at the crack tip. This fragment loosened from the fracture surface may significantly contribute to crack closure which will be discussed in Section V.

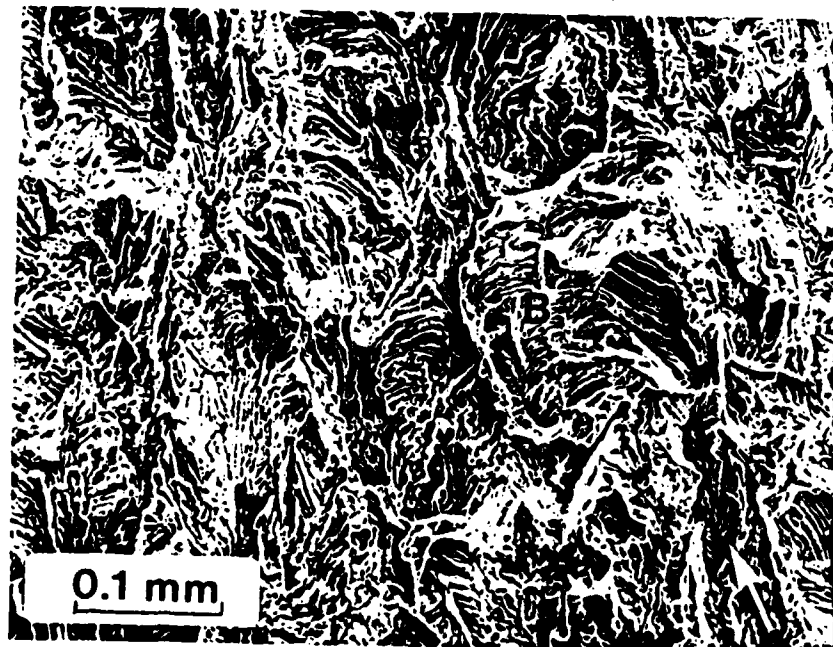
III. 4. Crack Growth Under Complex Loading: Overload Effects

4.1 Introduction

It has been well known that an intermediate tensile peak overload applied in a uniform loading test causes the crack growth delay or retardation. Since many engineering structures are subjected to complex variable loadings in real service condition, the study on mechanism of the crack growth retardation caused by overloads can be thought as a first step toward understanding more complex phenomena in



(a)



(b)

Figure 28a: Scanning electron fractograph showing secondary cracks labelled by "A" parallel to the specimen surface. The propagation direction was indicated by the arrow.

Figure 28b: Typical scanning electron fractograph of 2048 aluminum showing a fragment labelled by "B". The propagation direction was indicated by the arrow.

crack growth under spectrum loading condition. When the retarding effect of peak overload on crack growth is disregarded the prediction of material fatigue life is usually too conservative (43). For more accurate predictions of the fatigue life to failure, therefore, retardation mechanism should be not only qualitatively understood, but also quantitatively modeled.

To date several mechanisms have been advanced in an attempt to explain the phenomenon of retardation. Among these proposed mechanisms are compressive residual stresses ahead of a crack tip (44,45), crack tip geometry with blunting (46), and crack tip closure (5,6). A crack tip geometry model advocates that high tensile load cycles cause crack tip blunting, which in turn causes retardation in fatigue crack growth at the lower cyclic loads until the crack is resharpened. The residual stress model suggests that the application of high tensile overload forms favorable compressive residual stresses in the vicinity of the crack tip that reduce the rate of fatigue crack growth. Recently, the closure model has received more attention from many researchers to explain the retardation phenomenon qualitatively and/or quantitatively (8,34,47,48).

In the present study, the quantitative usefulness of the closure concept has been tested by correlating the kinetics of crack growth through overload affected regions in terms of ΔK_{eff} , first after single cycle overload and next following multiple and periodic overloads. The results suggest that the crack tip closure model is of considerable utility in the non-uniform loading histories employed here, and should

therefore be considered as a possible quantitative tool for more complex spectrum loading.

The role of microstructure on retardation effect was also studied by varying the ageing condition. It turned out that the magnitude of retardation following isolated and periodic single cycle overloads was more pronounced in the underaged microstructure than in peakaged or over-aged microstructures.

4.2 Experimental

Single and multiple, single cycle, overloads tests were performed on 25.4 mm and 12.7 mm thickness CT specimens of different microstructures whose configuration and loading direction are identical to those for uniform loading test. Single tensile peaks of 100% overload were applied periodically with programmed intervals to determine their effects on subsequent crack growth and on the closure level. Since it was found through the study of crack closure under uniform loading that the crack growth mechanism is predominantly in the opening mode (Mode I) after the crack closure transition, which will be discussed in detail in the next section, the overload tests were performed after the fatigue crack had grown into the post-transition zone. Under this condition, the closure model could be adopted with less uncertainty to quantify the observed crack growth retardation behavior following overload. The crack lengths and the closure loads were again measured by the differential compliance technique explained in Section III.2. All the other test variables were the same as those in the uniform loading tests.

4.3 Results

4.3.1 Single Cycle Overload

The response of a material to non-uniform loading can be quite different from its response to uniform loading. For this reason a number of tests were carried out for the purpose of studying specimen response to single and multiple, single cycle, overloads. This is believed to be the first step toward understanding fatigue crack growth under conditions of spectrum loading.

As an example, Figures 29a-d contain the results of a single cycle overload on a 12.7 mm thick specimen in the T851* temper. The uniform load amplitude was 1.0 kN and at a crack length $a = 39.4$ mm the load was increased to 2.0 kN for one cycle; subsequently the load amplitude was maintained at the original 1.0 kN level. Figure 29a shows that crack retardation followed the overload; the solid line is an extrapolation of the crack growth rate data based on data compiled from tests involving only uniform loading, whereas the points are the measured crack lengths. The two sets of points shown are explained by considering the results on crack tip closure shown in Figures 29b and 21d. Figure 21d shows a set of typical different compliance curves following a single cycle overload. The reversal in slope, especially noticeable after the curve marked g, indicates at least two crack opening loads - the first where the record becomes approximately vertical, and the second where it bends over but again becomes linear. Two changes in compliance would have occurred and thus two "opened" crack lengths observed. This explains the two crack lengths indicated by the circles and crosses in Figure 29a.

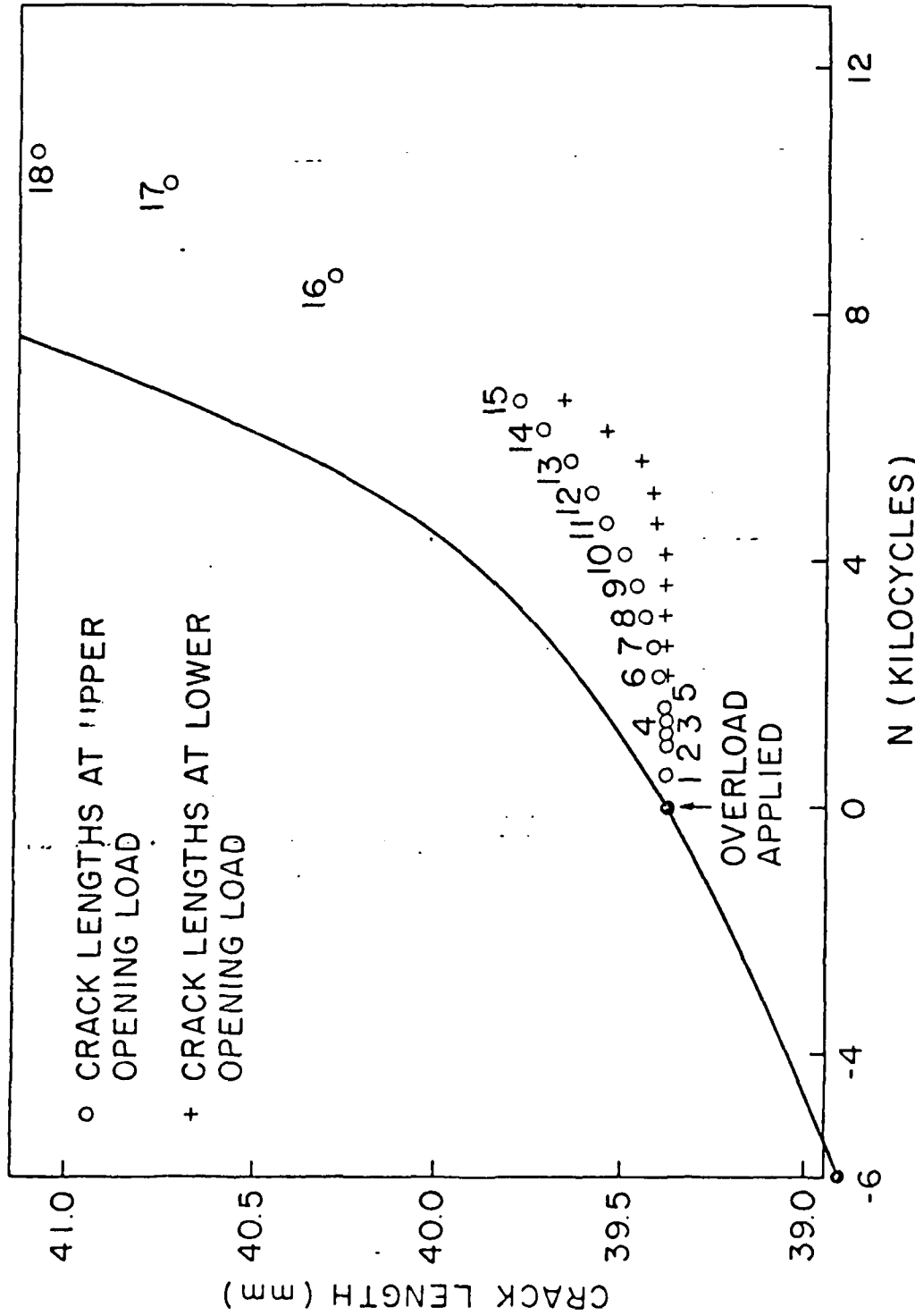


Figure 29: Results on overload retardation in crack growth following a single cycle overload in 2048-T851.

(a): Crack length vs. number of cycles applied. The solid line represents the estimated crack growth rate curve without overload.

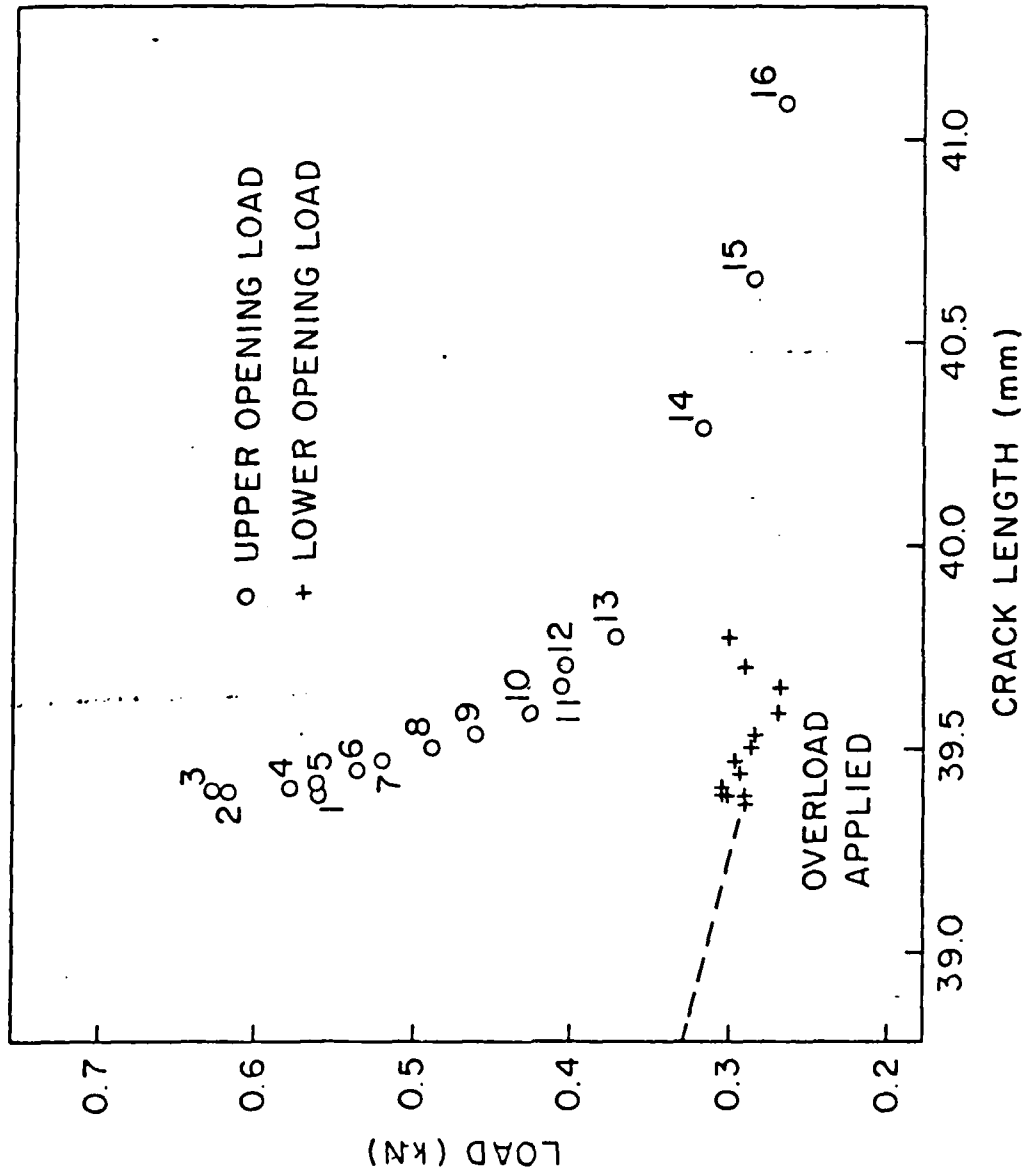


Figure 29(b): Variation of lower and upper opening loads with crack length. The straight solid line shows the level of single opening loads before the overload. Note that the lower opening load disappears to become a single opening load after point 15, implying that the crack has grown out of the overload affected region.

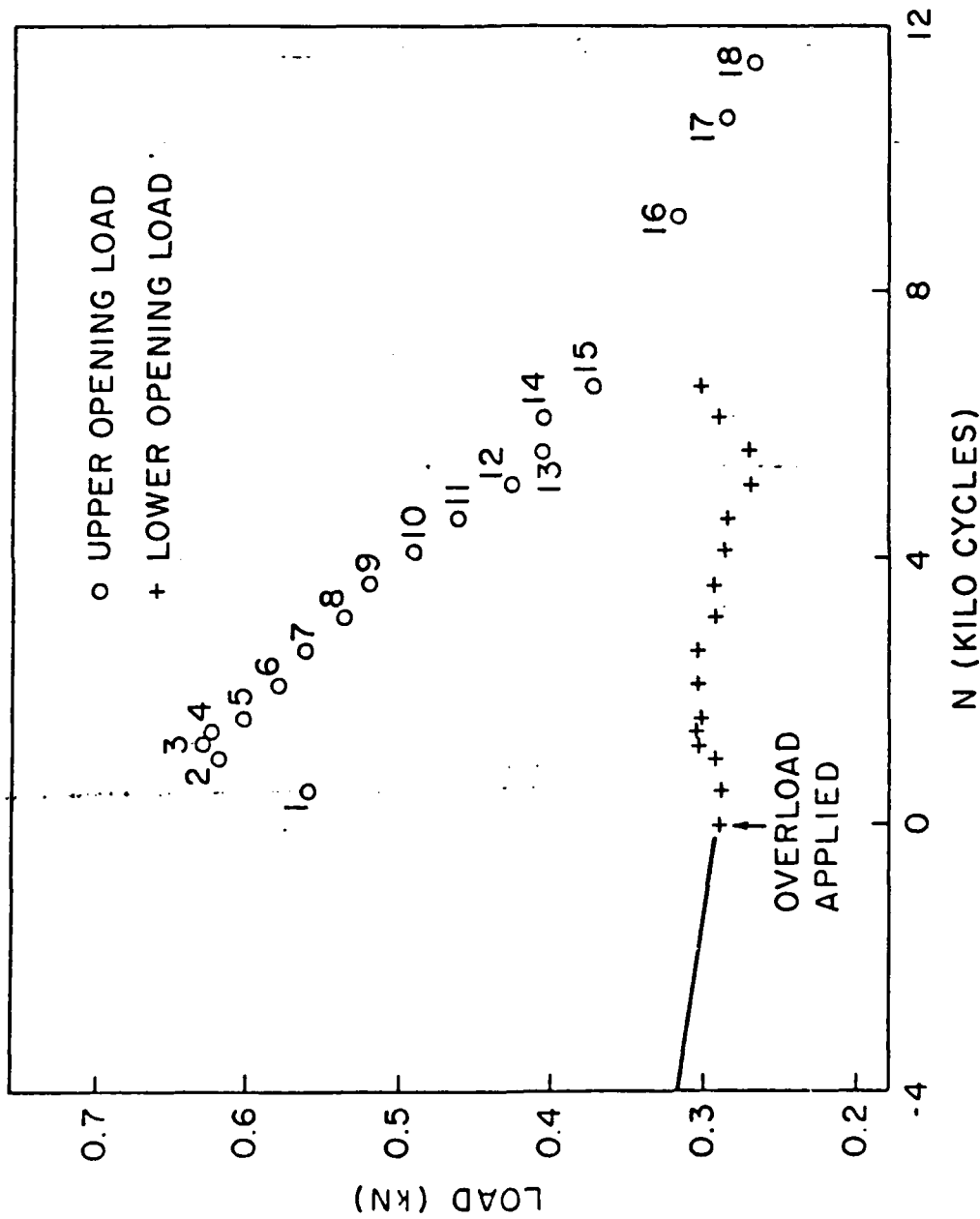


Figure 29(c): Lower and upper opening loads vs. number of cycles applied. The solid line again shows the level of opening loads before the overload.

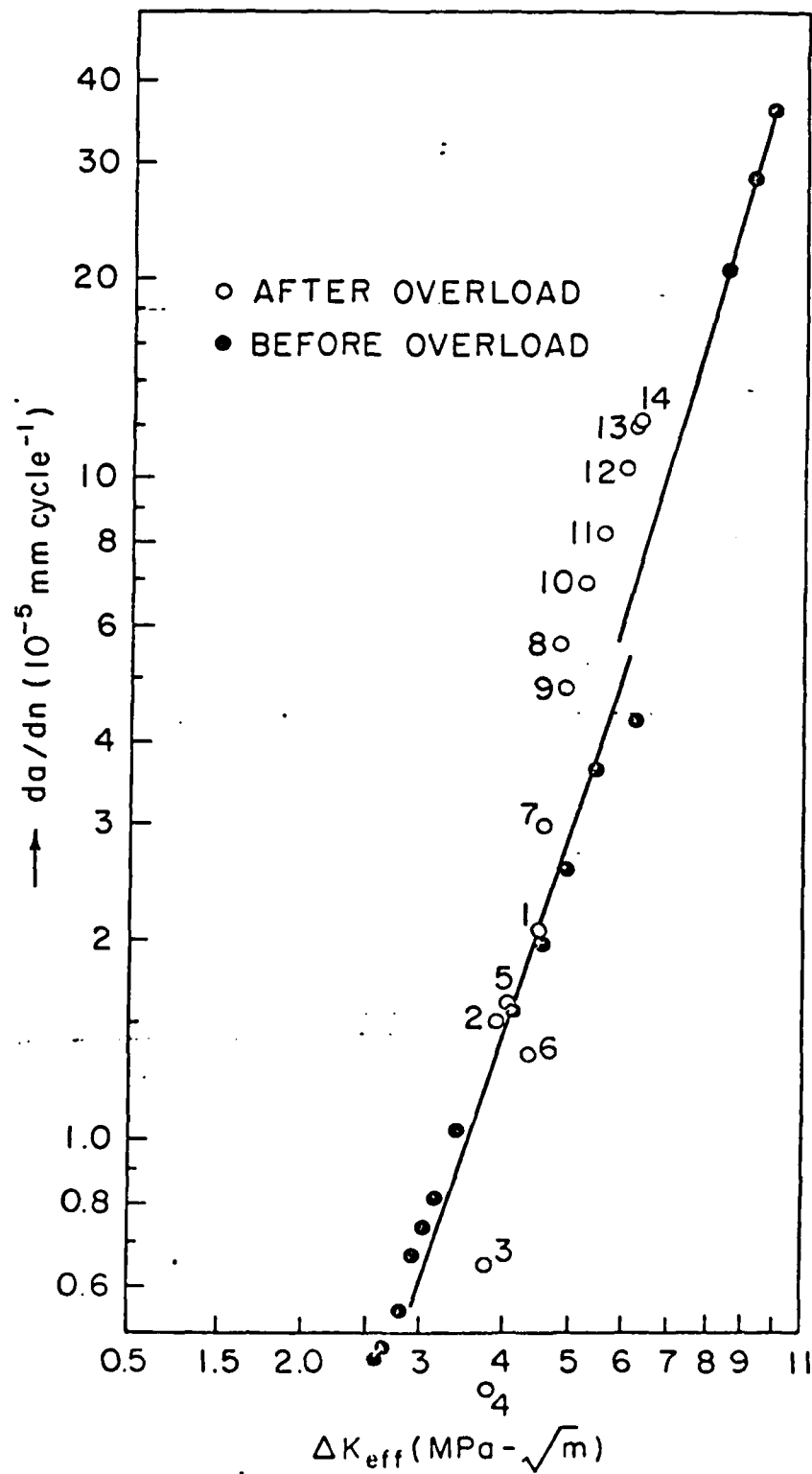


Figure 29(d): Crack growth rates vs. ΔK_{eff} . The closed circles indicate the crack growth rates before overload and the open circles after overload.

From the above observations, it can be concluded that these two opening loads, to be called "lower" and "upper" opening loads hereafter, resulted from two different degrees of stretched zones in the wake of a running crack; the lower one which corresponds to the original opening load resulted from previous uniform loading but slightly decreased in magnitude after overload was applied, and the upper one which corresponds to a true opening at a new crack tip as the crack grows into the overload affected region.

The duration of the overload effect is indicated in Figures 29b and 29c in terms of crack length and the number of cycles following the overload. Once the crack tip has passed through the overload affected zone both the upper and the lower opening loads approach the values which have prevailed in the absence of any overload effect.

In order to see if the observed crack retardation could be explained using a ΔK_{eff} model, ΔK_{eff} was computed using the upper opening load to calculate K_{open} . The results are shown in Figure 29d. Here, and in Figures 29a-c, the numbered data points correspond. Except for the point labeled 4 (shown off scale), there seems to be relatively good correspondence between the measured da/dN and ΔK_{eff} computed from the continually monitored opening loads. Examination of this and similar measurements on the T351 and T851 tempers strongly suggested that the closure concept might offer a reasonably good explanation of overload retardation in the case of periodic, single cycle, overload.

4.3.2 Periodic Overloads

A periodic single cycle overload test was first conducted on a 25.4 mm thick specimen in the T351 temper. The uniform load level was 2.2 kN

and at a crack length of approximately $a \approx 39.6$ mm the load was increased to 4.4 kN for one cycle; the load was then returned to the uniform 2.2 kN and the overloads were repeated every 5000 cycles. The solid line in Figure 30a is the crack advance curve predicted from the data shown in Figure 25 without overloads; overload retardation is evident in the data where different symbols have been used following each overload. It should also be noted that even after 5000 cycles the effects of a 100 percent overload have not vanished. It appears to take about 15,000 cycles, or approximately 0.2 mm of growth before the effects of the overload vanish.

Now the computed width of a "static" plastic zone formed due to the 100 percent overload was 0.19 mm. This implies that the second and third overload were applied while the crack was still under the influence of the first overload. A cumulative overload effect, therefore, could be expected for crack growth retardation. This is apparent when the closure levels were continuously recorded as the crack grew through the overload affected zones, as shown in Figure 30b for both closure levels of the lower and upper opening loads. Crack length and $\Delta K_{eff} (\equiv K_{max} - K_{open})$ were again computed at the upper opening loads. The data show a transient increase in the closure levels, with a maximum value of P_{open} after about 0.04 mm of crack growth. The closure level remains high (i.e., above the pre-overload value) even after 5000 cycles where another overload was applied. In this case, there has indeed been a cumulative effect of the consecutive overloads. This can also be seen by the gradually rising peaks in closure loads following each overload.

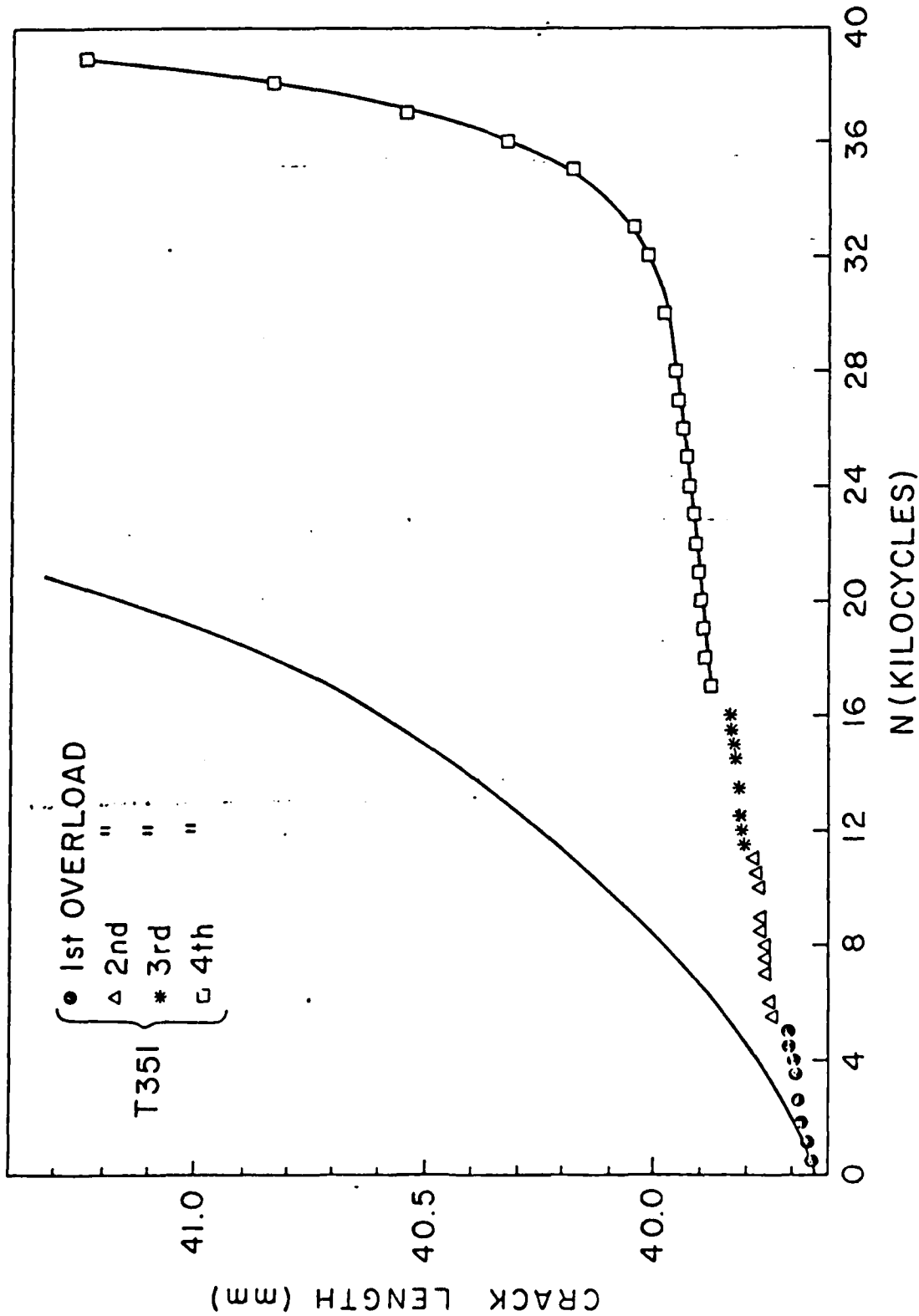


Figure 30: Retardation of crack growth in the T351 temper following periodic single cycle overload with 5000 cycle intervals.

(a): Crack length vs. number of cycles applied. The solid curve shows the estimated growth rate curve without any overloads.

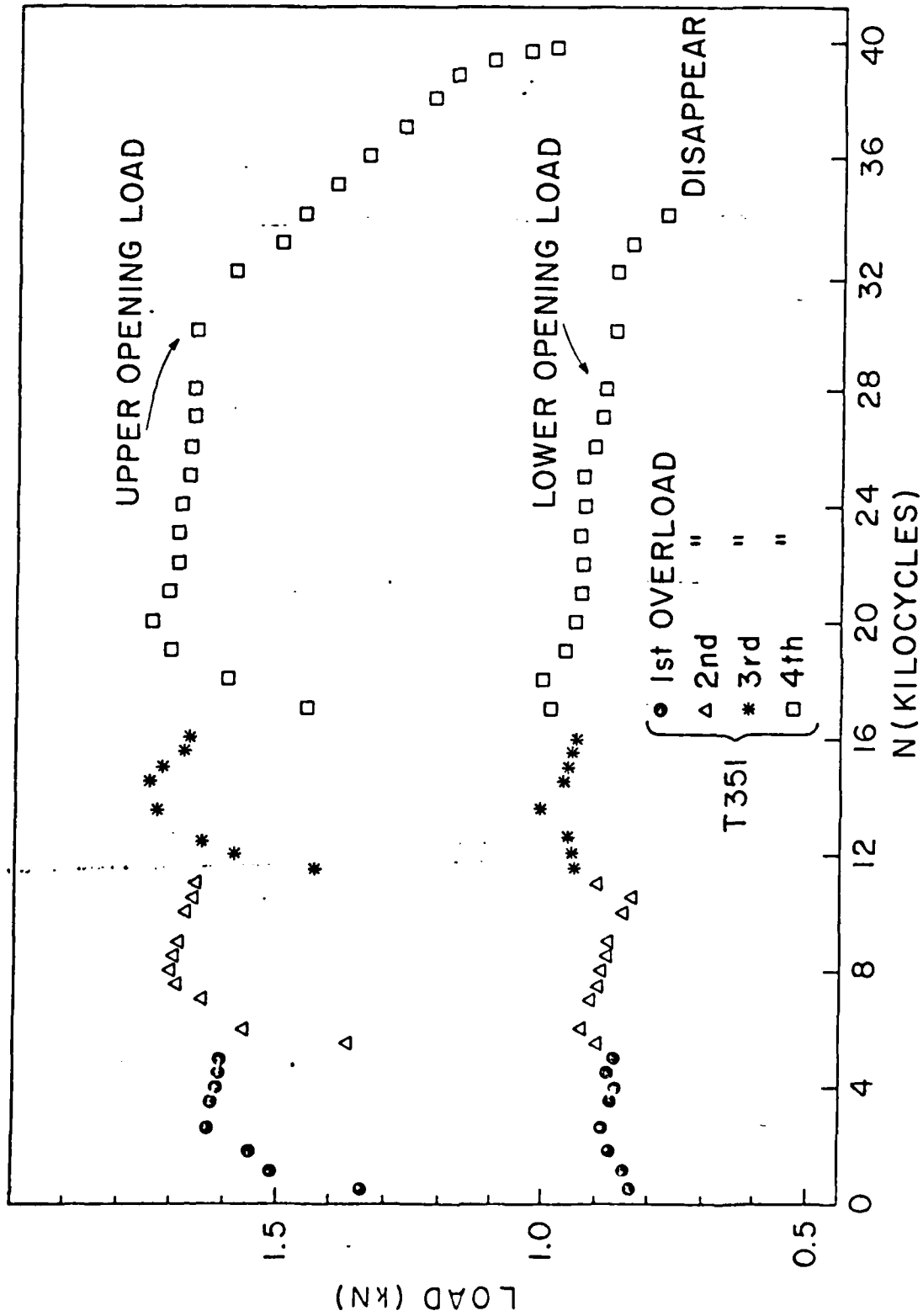


Figure 30(b): Closure level variation with number of cycles. Note that the average closure levels monotonically increase following each overload.

A different type of a multiple overload test was conducted on a 25.4 mm thick specimen in the T851*, slightly overaged temper. In this case, the consecutive overloads were applied after the crack had fully grown out of the plastic zone formed by the previous overload. Retardation is much less pronounced than for the T351 temper, as shown in Figure 31a.. The maximum uniform load was again 2.2 kN with 100 percent overloads applied where indicated. After 4000 cycles (or 0.1 mm of crack growth) the crack growth rate appears to have returned to its pre-overload value whereas for the T351 temper a much greater amount of crack growth would be required to eliminate the effects of the overload. The computed plastic zone width was also 0.1 mm which agrees well with the observed value for the overload affected zone. The closure levels for this specimen are shown in Figure 31b. After 13,000 cycles the opening load has indeed returned to the pre-overload value and there was no cumulative increase in the peak value. In this case of an "isolated" overload, the results show little observable influence of one overload on subsequent overloads.

As a third example, we take a case where multiple overloads with smaller intervals, viz., 3000 cycles, were applied on a specimen with a T851 temper. The effects of the first overload appeared to disappear after around 3000 cycles (or after 0.15 mm of crack growth which is again the plastic zone width) and yet subsequent overloads had a notably cumulative effect on retardation, as shown in Figure 32a. Compared with the T351 and T851* tempers, although the T851 temper has the highest crack growth rates, as shown in Figure 25 in the first overload affected

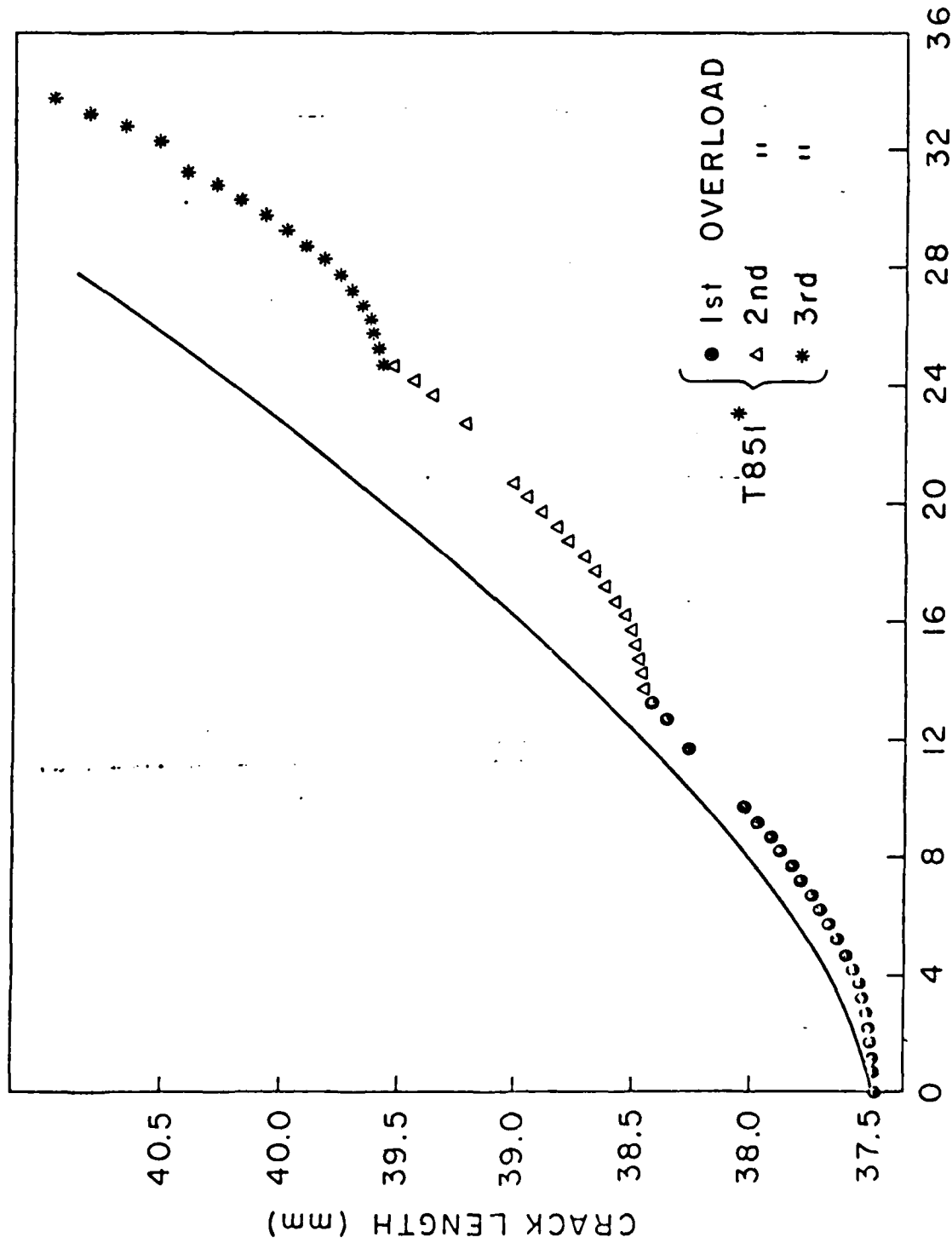


Figure 31: Results on crack retardation in the T851* temper by "isolated" single cycle overloads.
(a): Crack length vs. number of cycles applied.

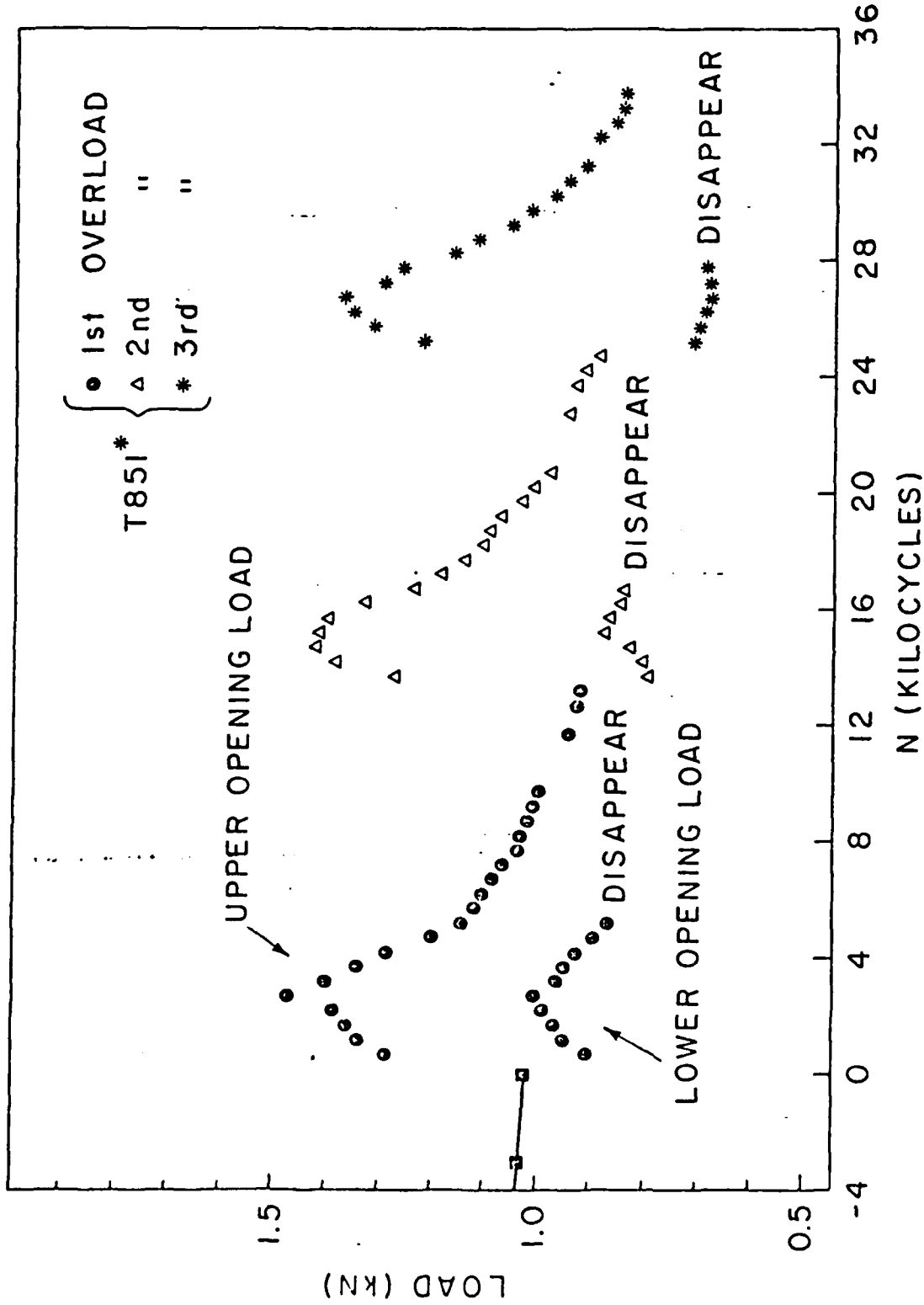


Figure 31(b): Closure level variation with number of cycles. The absence of cumulative effects in (a) can be explained by the monotonic decrease of average closure levels after each overload.

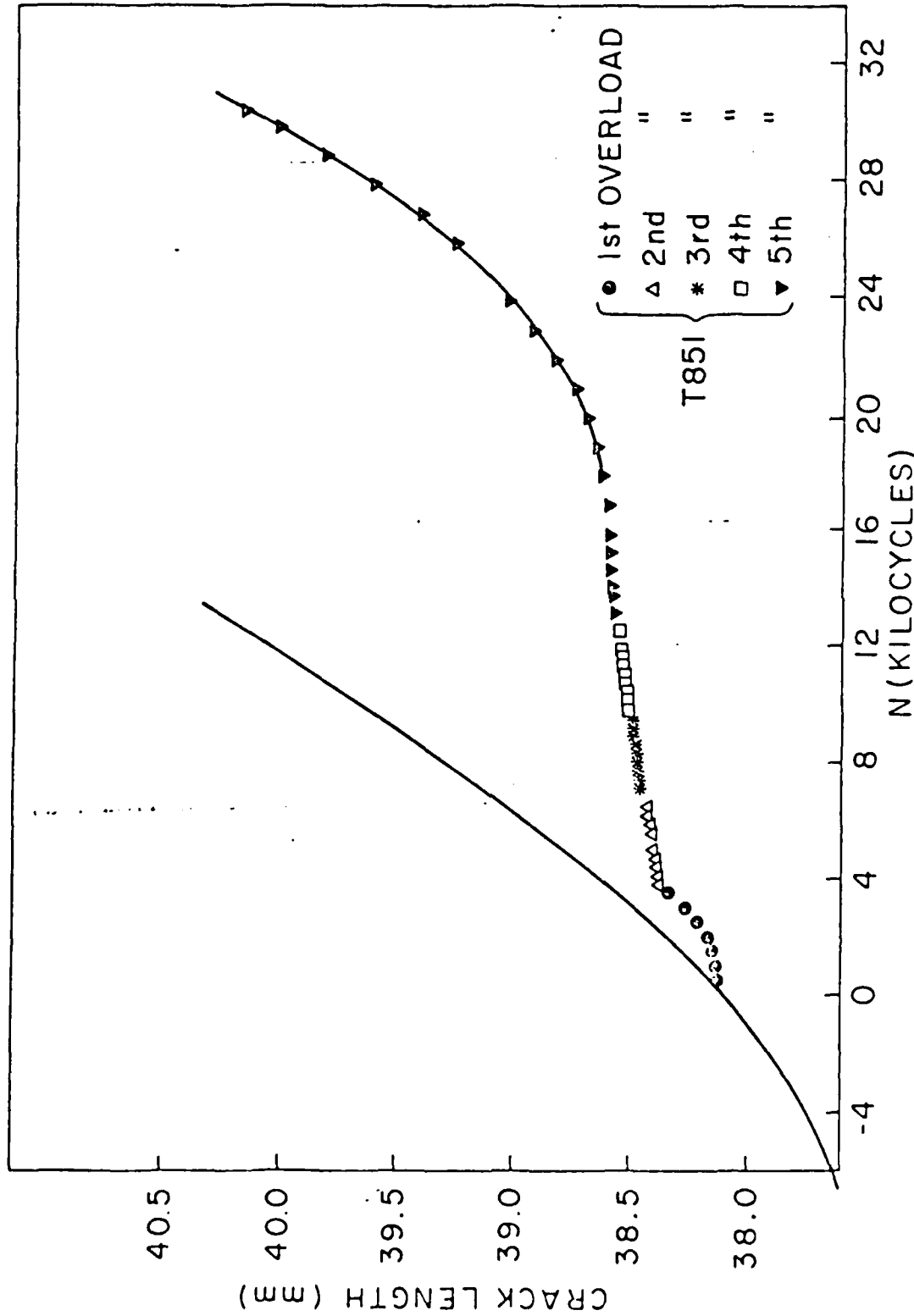


Figure 32: Crack growth retardation in the T851 temper following periodic single cycle overload with 3000 intervals.

(a): Crack length vs. number of cycles applied. The crack growth rate curve is gradually decreasing after undergoing each overload.

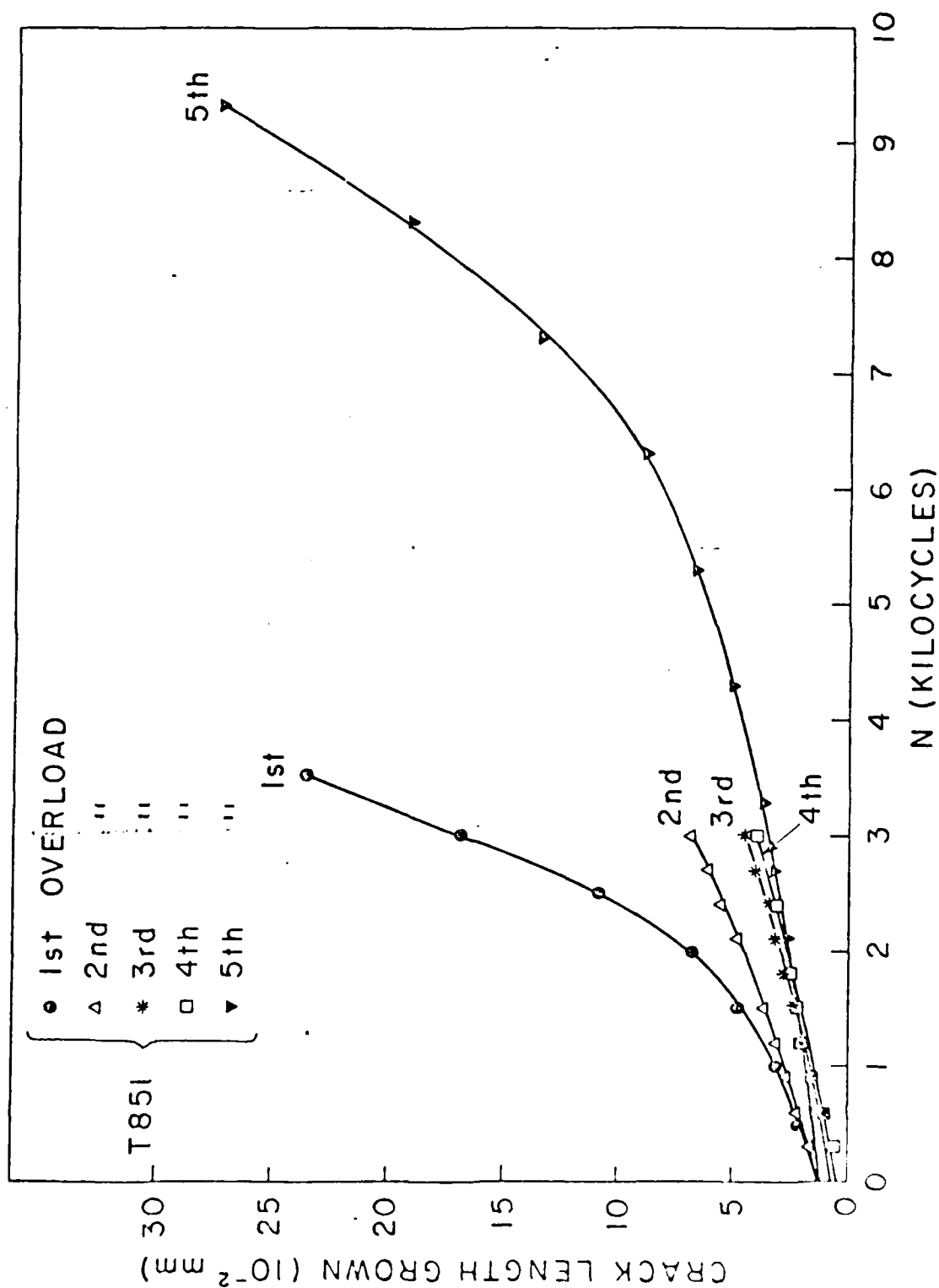


Figure 32(b): Magnified growth curve showing the decreasing slope following each overload.

A STUDY OF LOCALIZED PLASTIC DEFORMATION AS RELATED TO
FATIGUE MECHANISMS(U) BROWN UNIV PROVIDENCE RI DIV OF
ENGINEERING J BAIK ET AL. MAY 82 AFOSR-TR-82-0990
AFOSR-77-3246 F/G 11/6

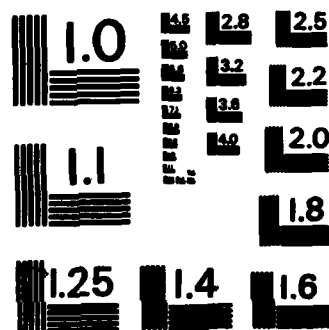
UNCLASSIFIED

AFOSR-77-3246

F/G 11/6

NL

END
*
Dimitri
JAG



MICROCOPY RESOLUTION TEST CHART
NATIONAL BUREAU OF STANDARDS-1963-A

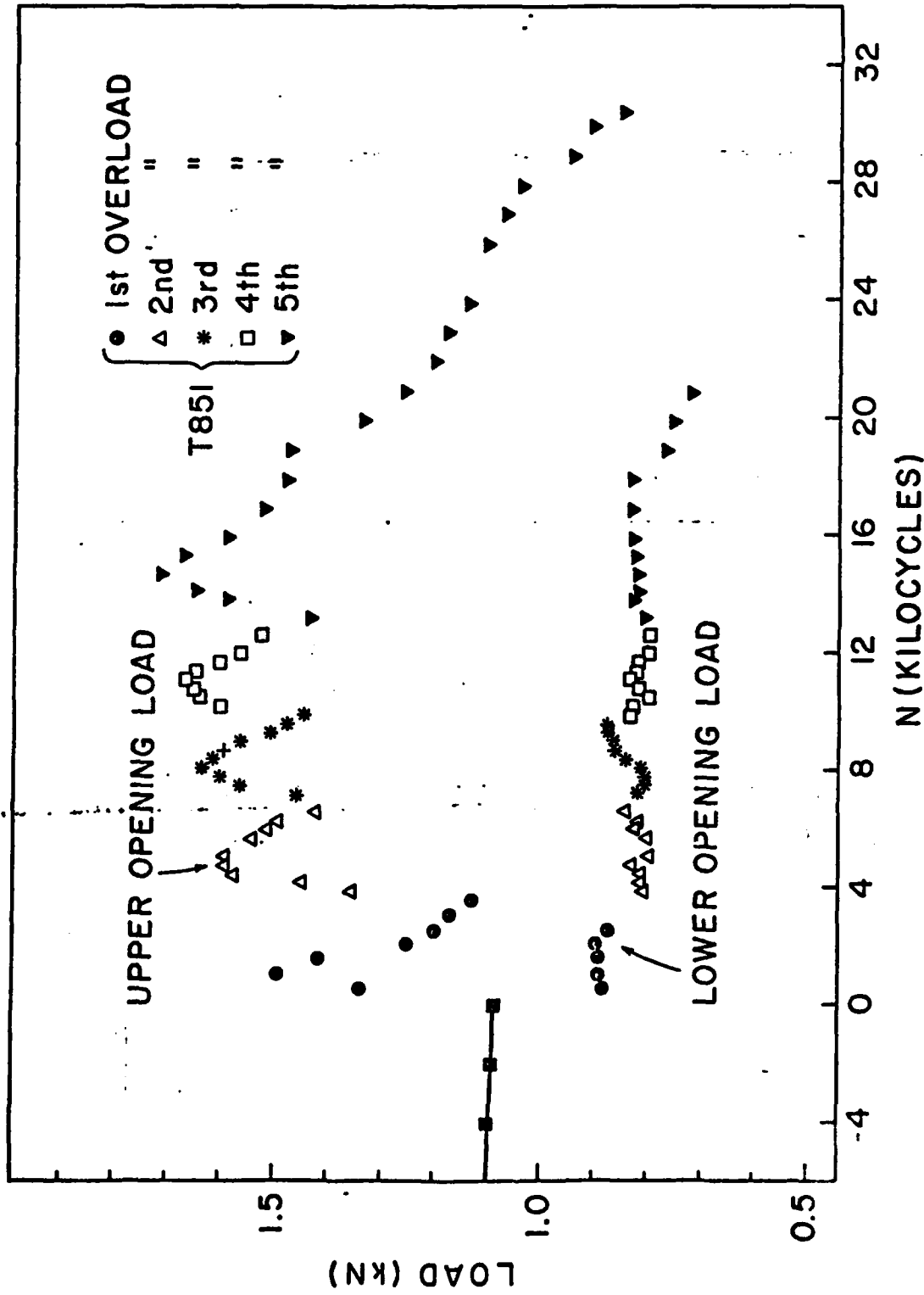


Figure 32(c): Closure level variation with number of cycles. The apparently increasing closure levels would predict decrease in growth rate after undergoing each overload.

zone, the accumulated overload effect is so pronounced that the rate of crack advance became the lowest following the consecutive overloads. The decreasing growth rates are shown in Figure 32b on a magnified scale where each curve starts at a position on the crack length axis which corresponds to the crack length immediately following the overload itself. The general reduction in the slopes of successive curves indicates a compounding overload retardation effect. Figure 32c shows the closure levels and again, the cumulative nature of each overload can be explained by the increasing closure loads.

A further comparison of overload retardation in the three tempers is shown in Figure 33. The three curves shown are for multiple overload tests with overload intervals of 5000 cycles for the T351 and T851* tempers, and 3000 cycles for the T851 temper. It is important to note that the initial overloads were applied at different initial crack lengths; the crack lengths, and therefore the maximum applied stress intensities, were highest for the T351 temper. Nevertheless, the rate of crack advance appears lowest for the T351 temper which illustrates that in this alloy, under the present conditions of testing, retardation was more pronounced for this temper.

Figure 34 shows three correlations of crack growth rate through overload affected regions in terms of an effective stress intensity range, ΔK_{eff} , where K_{open} was computed using the upper opening loads as described before which presumably correspond to fully opened cracks. In all cases the correlations appear quite good. The solid lines on each plot are based upon da/dN data obtained from tests employing uniform load amplitudes.

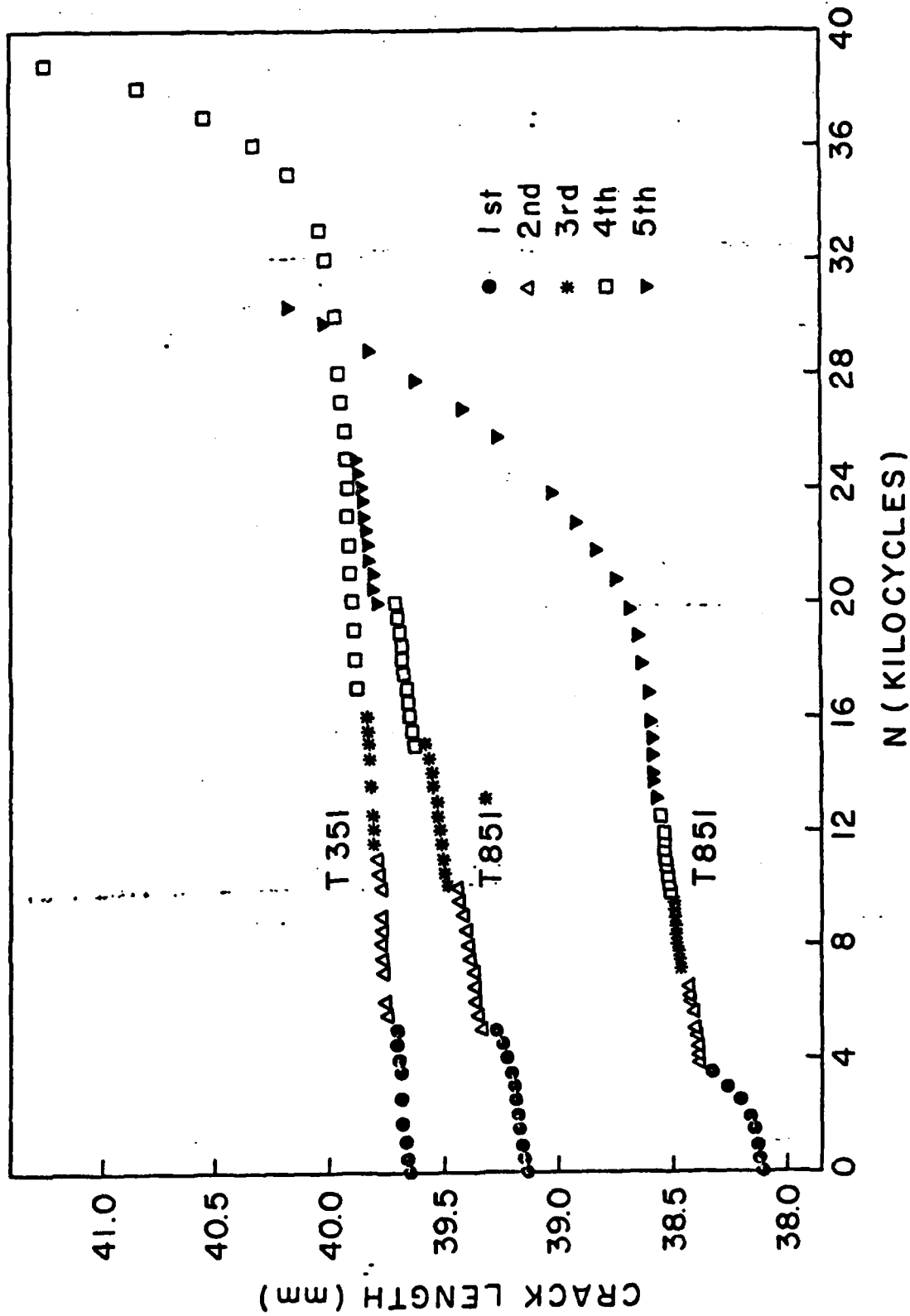


Figure 33: Comparison of overload retardation after multiple overloads for the three temps. Overload intervals are 5000 cycles for the T351 and T851* temps and 3000 cycles for the T851 temper.

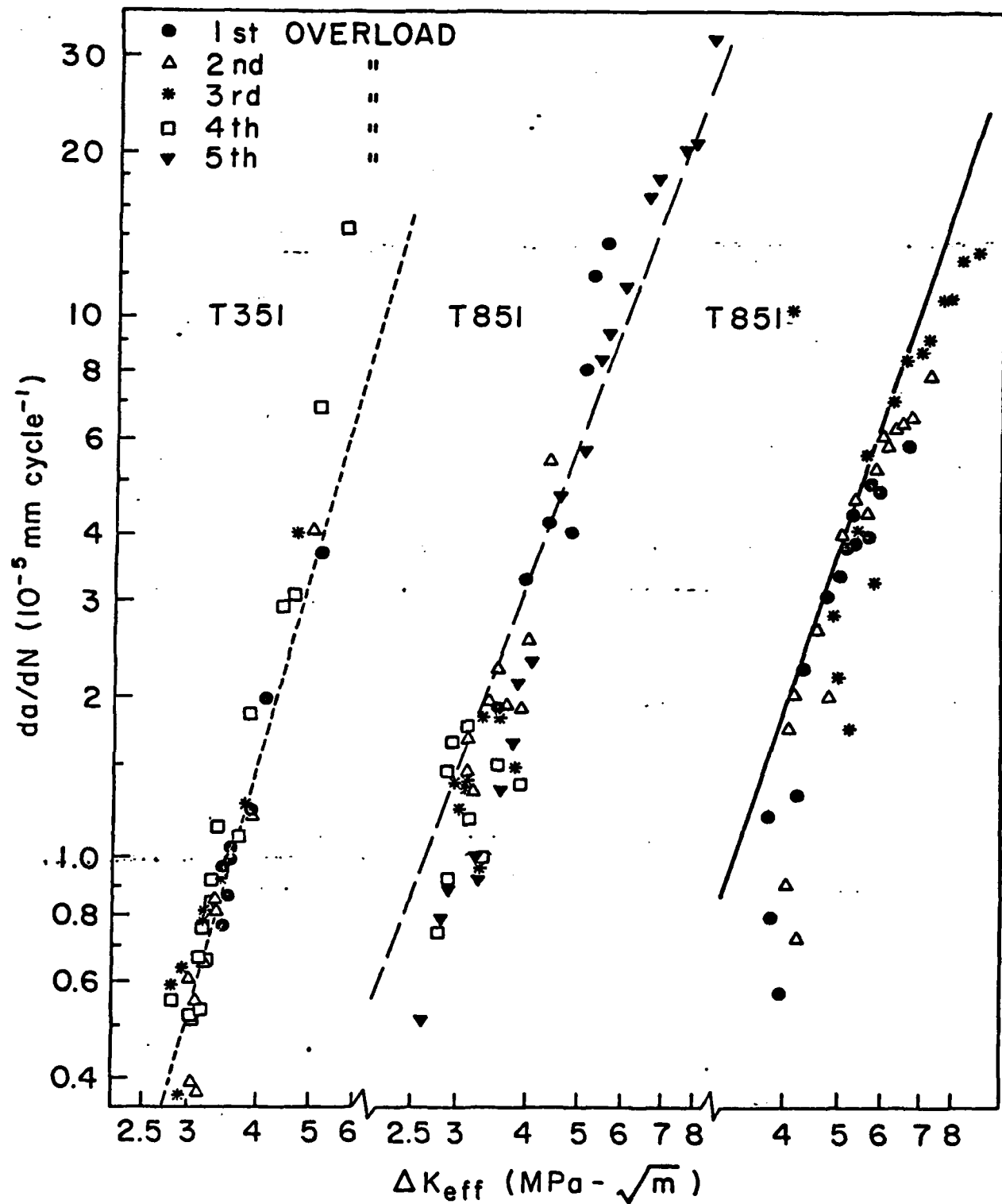


Figure 34: Crack growth data after each overload for three different tempers in terms of ΔK_{eff} . The straight lines on each plot are based upon Figure 25, which shows the results from uniform load amplitude.

4.3.3 Fractography

A scanning electron fractograph of the overloaded region is shown in Figure 35. This shows an identical fracture morphology before and after the overload except in the plastically stretched overloaded zone. The stretched band in Figure 35 was formed by a single cycle overload at a high K_{max} value and shows dimple rupture around the inclusion particles. In fact, the width of this band which has been known to be related to the fracture toughness of the material (49), primarily depends on the stress intensity level at overload; high K_{max} causes the crack jump and big dimple rupture band whereas low K_{max} results in the fine striations of stretched band. It should be noted at this point that these fine striations from overloads are completely different from the ductile striations formed typically during stage II crack growth as shown in Section II. 3.

Figures 36a-c show the fracture surfaces of three different microstructures subjected to periodic, single cycle 100 percent overloads. The positions of the crack fronts at the points where overloads were applied show up as fine striations as explained above. As a guide to their locations, a few of these have been indicated in the photographs. These figures may be used as a further means of appreciating the accuracy and sensitivity of differential compliance technique used for measuring crack lengths and crack length changes. The crack growth increments between the periodic overloads were measured under the SEM fractograph and these measurements were directly compared with the calculated crack growth increments detected from the differential

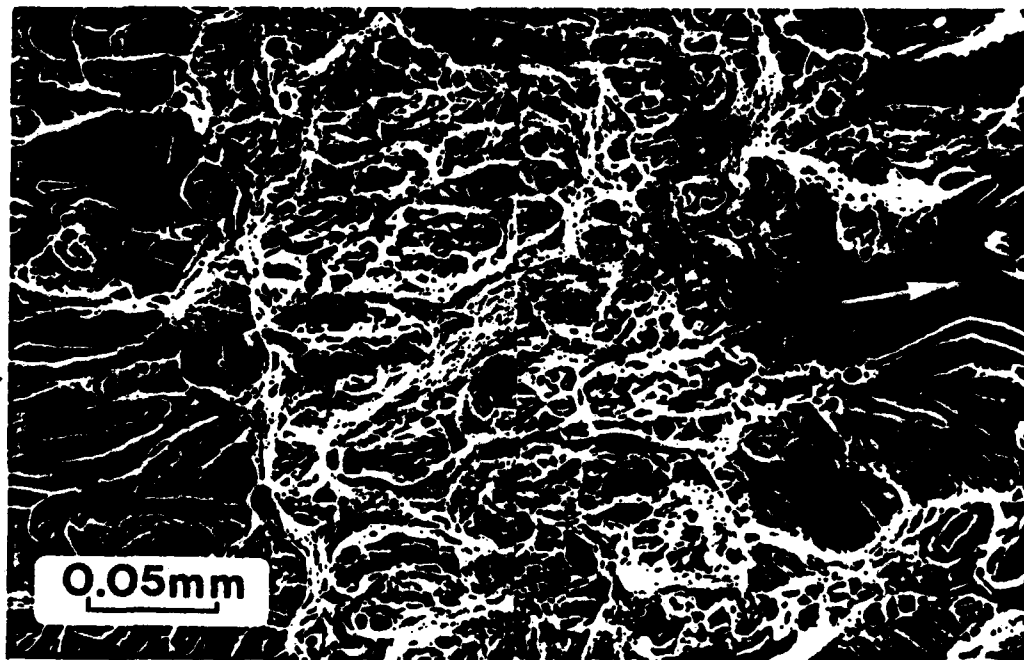
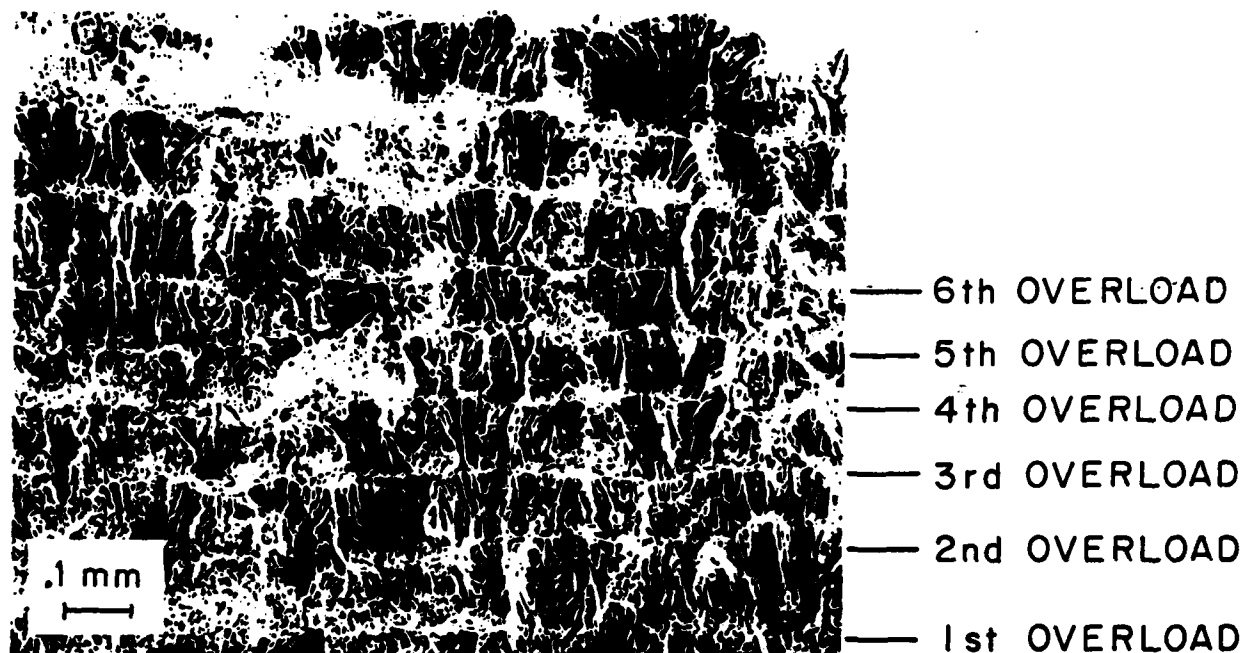


Figure 35: Scanning electron fractograph of the overloaded zone in 2048 aluminum. The propagation direction was indicated by the arrow.



CRACK LENGTH CHANGES BETWEEN OVERLOADS

	FRACTOGRAPH	MEASUREMENT BY DIFF. COMP. TECH.
AFTER 1st O.L.	0.144 mm	0.142 mm
AFTER 2nd O.L.	0.113 mm	0.111 mm
AFTER 3rd O.L.	0.100 mm	0.099 mm
AFTER 4th O.L.	0.091 mm	0.093 mm
AFTER 5th O.L.	0.095 mm	0.097 mm
TOTAL	0.543 mm	0.542 mm

(a)

Figure 36: SEM fractographs after periodic overloads.

(a) T851 temper subjected to eight overloads. The first five overloads are indicated as a guide to their location.

(b) T851* temper

(c) T351 temper

The comparison of computed and measured crack length changes establishes the accuracy of the differential compliance technique.

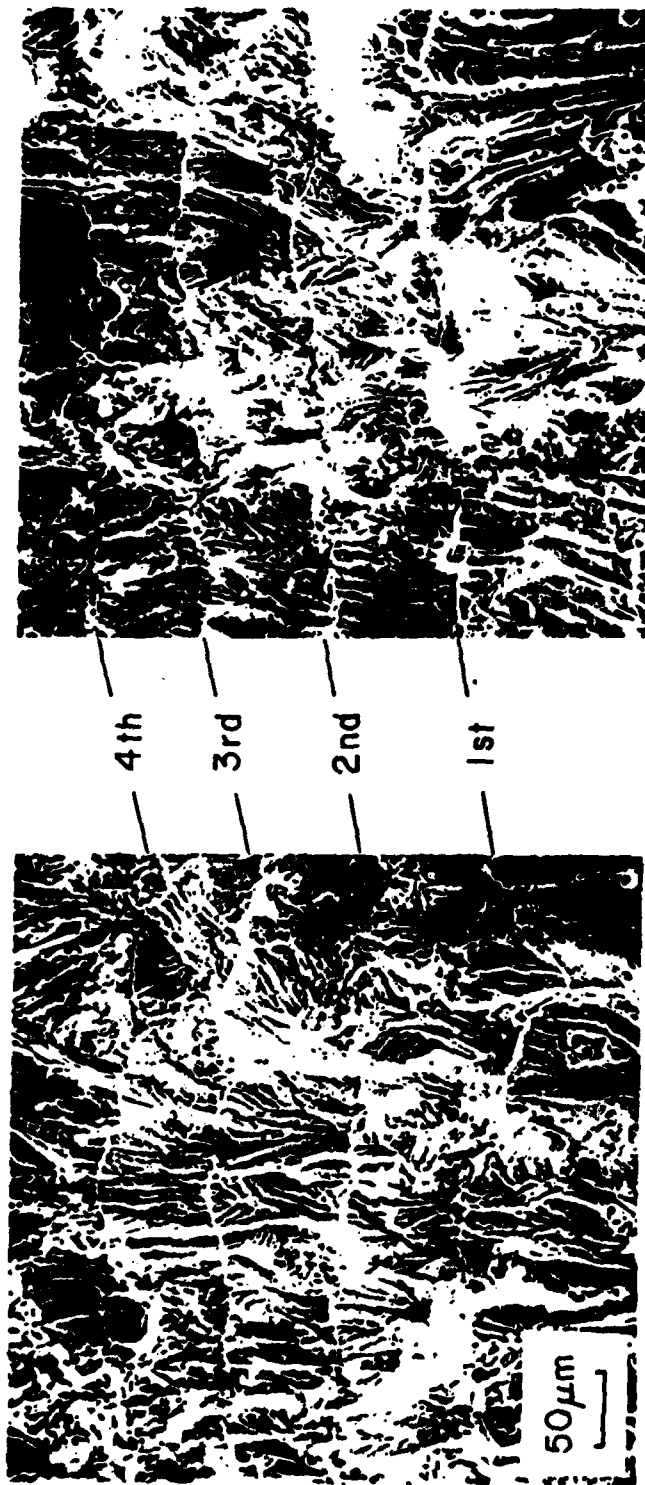


Figure 36(b)

CRACK LENGTH CHANGES BETWEEN OVERLOADS

	FRACTOGRAPH		MEASUREMENT
	LEFT	RIGHT	BY DIFF. COMP. TECH
AFTER 1st O.L.	0.088 mm	0.086 mm	0.088 mm
AFTER 2nd O.L.	0.072 mm	0.071 mm	0.069 mm
AFTER 3rd O.L.	0.065 mm	0.062 mm	0.059 mm
TOTAL	0.225 mm	0.219 mm	0.216 mm

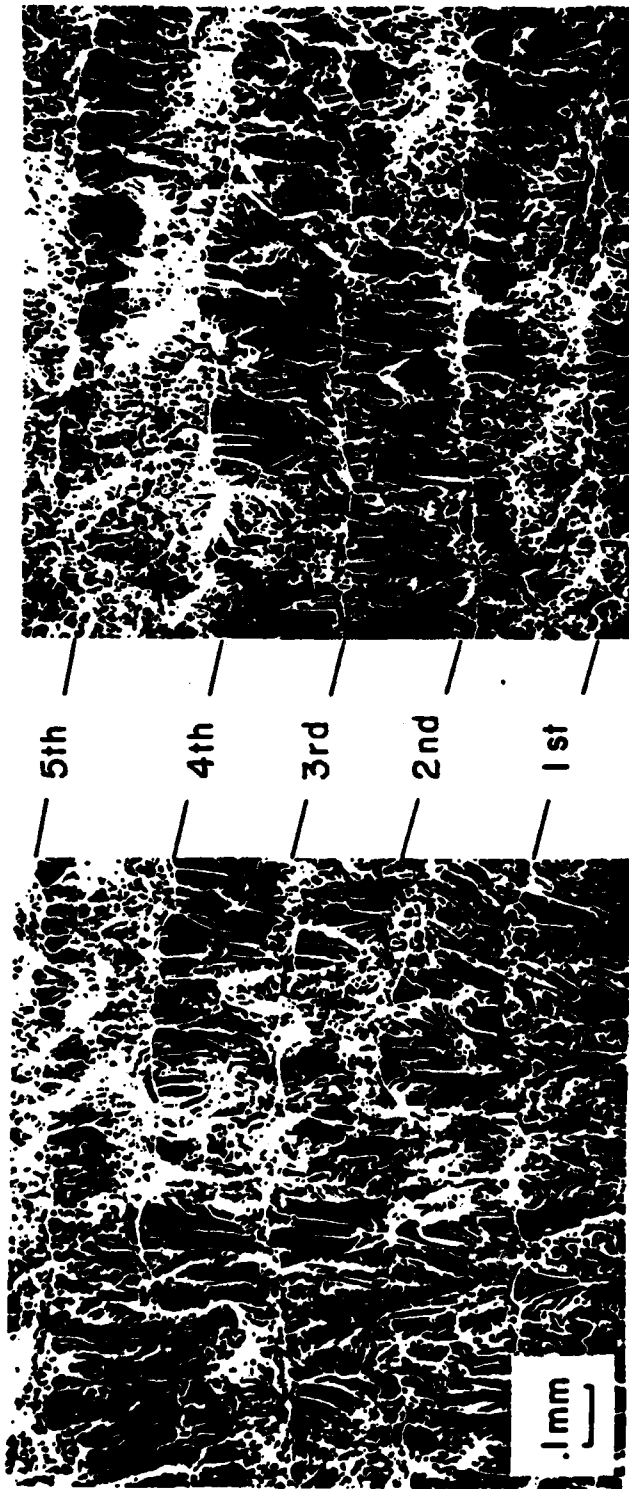


Figure 36(c)

CRACK LENGTH CHANGES BETWEEN OVERLOADS

	FRACTOGRAPH		MEASUREMENT BY DIFF. COMP. TECH.
	LEFT	RIGHT	
AFTER 1st O.L.	0.227 mm	0.234 mm	0.235 mm
AFTER 2nd O.L.	0.196 mm	0.203 mm	0.199 mm
AFTER 3rd O.L.	0.202 mm	0.205 mm	0.190 mm
AFTER 4th O.L.	0.237 mm	0.252 mm	0.293 mm
TOTAL	0.862 mm	0.894 mm	0.917 mm

change in compliance. The comparison results, listed in each figure separately, show indeed very good correlations which can be taken as evidence of both the accuracy and sensitivity of the differential compliance technique employed here.

III. 5. Discussion

In the present research program, both the low cycle fatigue (LCF) resistance for smooth, uniaxial tensile specimens and fatigue crack growth rate (da/dN) from plane strain compact tension specimens under both uniform loading and complex loading have been studied with different microstructures obtained by varying the ageing heat-treatment. When the fatigue properties of different microstructures are evaluated, both approaches must be considered as the former primarily deals with fatigue crack initiation while the latter is obviously concerned with crack propagation. Cyclic stress-strain properties obtained from incremental strain step tests are also incorporated to further understand fatigue crack growth behavior.

Since the basic fracture mode in all aluminum alloys is dimpled rupture characterized by particle or particle-interface fracture, void growth and coalescence, the nature, distribution and size of precipitates and/or second phase inclusions are all important in both fatigue initiation and propagation as well.

5.1 Microstructure Characteristics

Second phase particles in high-strength aluminum alloys can be categorized into three kinds of microstructural features such as constituents, dispersoid and hardening precipitates according to the way

in which they form (50). The constituent particles, which are large ($> 1\mu\text{m}$) and form by eutectic decomposition during ingot solidification and cannot be taken into solid solution during fabrication, are either insolubles such as $\text{Al}_7\text{Cu}_2\text{Fe}$, Mg_2Si or $(\text{Fe,Mn})\text{Al}_6$ or relatively soluble $\theta(\text{CuAl}_2)$ or $\text{S}(\text{Al}_2\text{CuMg})$. The second grouping of particles ($0.03\text{--}0.5\mu\text{m}$) are dispersoids such as $\text{Al}_{12}\text{Mg}_2\text{Cr}$ or $\text{Al}_{20}\text{Cu}_2\text{Mn}$, which form by solid state precipitation and, once formed, cannot be dissolved. The dispersoids seem to have dual, but contradictory roles; they suppress recrystallization or limit the growth of grains, favoring the transgranular mode of fracture associated with the highest energy absorption, but also nucleate microvoids by decohesion at the matrix interface, leading to the formation of void sheets between larger voids (51). The third and finest set of particles ($\sim 0.01\mu\text{m}$) which seem important in the fracture process is the age-hardening precipitates of major alloying elements (GP zones) which impede dislocation movement, and lead to the optimum combinations of strength and toughness. It was reported that they contribute to high fatigue limits (50).

For the application of the above concepts, 2048 aluminum has been developed for high toughness without sacrificing the other mechanical properties. The principal contribution to the high toughness was the substantial reduction in Fe and Si contents, minimizing the relatively large insoluble constituents that crack first and initiate void growth, and reduction in the Cu content below that in 2024 or 2124, permitting complete dissolution of second phase to decrease the brittle insoluble constituent particles of $\text{S}(\text{Al}_2\text{CuMg})$.

The microstructures studied in this research program consist of different kinds of precipitates from various ageing conditions and can be described as follows. The underaged condition (corresponding to commercial tempers like T351) contains the small, shearable, coherent GP II zones. Strengthening mechanism of these microstructures is described by precipitation hardening in that the precipitates impose a friction stress on the dislocation movement by interaction with their coherency stress fields, and by the creation of anti-phase boundaries within the ordered precipitates through dislocation cutting. The peakaged (corresponding to commercial tempers such as T851) and slightly overaged (designated as T851* here) conditions comprise of large, nonshearable, incoherent S' (Al_2CuMg) and coarse GP II zones. Their monotonic hardening mechanism is the so-called Orowan (52) bowing mechanism, by which dislocations pass between the widely spaced precipitates leaving a dislocation loop around each particle as the dislocation line advances. This dislocation loop exerts the back stress to the next following dislocations, inducing the subsequent dislocation movement to be difficult. Consequently, the coherent and closely spaced precipitates will be sheared by moving dislocation because of high bowing stress, whereas the incoherent and widely spaced precipitates will be encompassed by dislocation loops left behind running dislocations due to low bowing stress and their non-shearability.

5.2 Monotonic and Cyclic Deformation Response

The steady state cyclic deformation resistance of metal is conveniently described by the cyclic stress-strain curve. In order to determine

the cyclic stress-strain response of each microstructure, the incremental strain-step technique was employed here among others, such as reversed strain cycling tests, on a number of companion specimens under constant strain amplitude condition (20); the strain amplitude changes with a set of several fixed amplitudes, the multiple step test (53) and complex varying strain test (54). Although the cyclic properties can be influenced by test methods and the differences in the results of different procedures has been reported (53,54), it was well regarded that all the methods yield approximately coincident results. An important advantage of this incremental step test is that directly comparable monotonic and cyclic stress-strain curves are developed by testing a single specimen quickly and economically. In addition, the cyclic stress-strain curve generated from this test may provide the most reasonable estimate of cyclic stress-strain response for variable amplitude loading conditions that are generally encountered in engineering design applications (55).

In Al-Cu system the decrease in tensile-test elongation values during early stages of ageing treatment is slight, whereas at about the point of maximum hardness or slight overageing a sharp drop in ductility values is observed. As shown in Table III of Section II, the ductility of the T851* temper is close to that of the T851 temper, while it shows only half the value of the T351 temper. This reduction of ductility seems to correspond to a very heavy and almost continuous grain-boundary precipitation of brittle $S'(AlCuMg)$. The results also show the dependence of ductility on grain size. The reduction of ductility with increasing grain size can be attributed to the fact that the larger grain

sizes lead to longer slip lengths, more intense dislocation pile-ups with greater stress concentrations at grain boundaries which result in tensile cracks.

Monotonic work hardening capacity, indicated by the strain hardening exponent, n , is highest in the T351 temper and lowest in the T851 temper, which is probably due to the difference between small, coherent GP II zones of the T351 temper and large, non-shearable, incoherent S' of the T851 temper. It also appears to be dependent on the inherent strength levels of microstructure in that the softer material shows high work hardening rate. In cyclic deformation response, these properties are reversed; the T351 temper shows consistent cyclic hardening and the lowest cyclic hardening exponent, n' . The T851 and T851* tempers show consistent cyclic softening and higher cyclic hardening exponents. In all cases, however, the cyclic strain hardening exponent increases considerably compared to the monotonic hardening exponent. The monotonic hardening exponent strongly depends, again, on grain size in that the coarse grained microstructure shows almost double the value of fine grained one, which is consistent with the results of Thompson (57) for copper polycrystal. After cyclic deformation, though, the cyclic hardening exponents of these two different grain size microstructures become very close.

There is a general trend that metals with high monotonic strain hardening exponents can be expected to cyclically harden, while those with low monotonic exponents can be expected to soften (17). It was also reported that metals with an ultimate tensile strength to yield

strength ratio (σ_u/σ_y) greater than 1.4 (implying a high monotonic hardening exponent) cyclically harden, while those with a ratio less than 1.2 (implying a low exponent) cyclically soften (58). These observations are consistent with the present result in that the T351 temper showing high n and $\sigma_u/\sigma_y = 1.27$ cyclically hardens, and the T851 and T851* tempers showing low n and $\sigma_u/\sigma_y = 1.10$ cyclically softens.

The degree of hardening/softening depends on the applied strain amplitude; at the 0.4% of total strain amplitude the stress variations of all microstructures studied are nearly flat up to final failure, so that they do not show any clear hardening or softening. It was observed in pure Al-Cu binary system (59) that cyclic hardening followed by softening occurred at large and intermediate strains, while at low strains softening did not occur. It should also be pointed out that 0.4% of total strain amplitude belongs to the elastic deformation region of the monotonic stress-strain curve for all microstructures, as shown in Figure 5. Nevertheless, the specimens did fail implying that the microscopic deformation is localized and accumulated at weak zones of material leading to final failure.

Calabrese and Laird (1,60) observed in a pure Al-Cu binary system cyclic hardening followed by softening for coherent precipitates of GPI and GPII (θ'') zones and cyclic saturation for incoherent θ' (CuAl_2). In the former case, they explained that cyclic hardening initially occurs because of interaction of dislocation-coherency stress field from precipitates and accumulation of dislocations and then softening follows when

the to and fro motion of dislocation scrambles the atoms in the precipitates so as to remove the ordering component of hardening. Laird et al. (56) further showed in Al-Ag alloy that the precipitates should be in ordered state for softening by disordering to occur.

In the commercial 2048 aluminum studied here, though, the T351 temper containing only coherent precipitates shows continuous cyclic hardening until final fracture over the entire strain range tested. Keeping in mind that commercial alloys have not only coherent GP zones but a considerable amount of both incoherent, non-shearable dispersoids and constituents as explained previously, the distribution of second phase particles can be regarded as an effective factor in preventing cyclic softening. These results are consistent with the results of Endo and Morrow (61), and Fine and Santner (59) who also observed continuous cyclic hardening in 2024-T4 commercial aluminum.

On the other hand, both the T851 temper and the T851* temper show continuous cyclic softening until final failure. It should be pointed out that these tempers showed double inflection points on their hysteresis loop during the initial cycles reflecting the large influence of internal stress hardening (24) due to non-shearable, elastic dispersed precipitates of S'. It was reported that the dispersion hardened system of pure alloys showed clear saturation following either initial hardening for Al-Cu binary system (60) or initial softening for Al-Cu-Mg ternary system (24). The fact that the commercial alloy of dispersion hardened system showed a gradual cyclic softening, again, emphasizes the role of the other second phase particles such as

constituents and dispersoids in cyclic deformation. The details of the softening process, however, are as yet unclear.

5.3 Fatigue Life and Crack Initiation

Since the most decisive parameter of the fatigue process is the cyclic plastic strain which is a necessary prerequisite for the existence of fatigue (26), the Coffin-Manson relation for plastic strain, $\Delta \epsilon_p / 2 = \epsilon'_f (2N_f)^c$, is widely adopted for determining fatigue resistance.

In the present LCF testing, two kinds of strain control tests were employed and compared: total strain control and plastic strain control. When the total strain amplitudes are maintained constant through the test, the plastic strain amplitudes will change depending on the cyclic hardening or softening behavior. Because of simplicity and ease nevertheless, total strain controlled has been still the majority of LCF experiment reported in which the plastic strain amplitude was determined conventionally by corresponding value at saturation point, or at half life ($N_f/2$) point if no saturation.

As shown in Figure 10, in the plastic strain range tested ($< 1\%$), considerable difference was observed between the results obtained from these two different tests. The difference was pronounced, in particular, for the T351 temper and in the low plastic strain range, in that the fatigue life determined from total strain control was poor compared to that from plastic strain control. Departure from the log-log linear relations reported elsewhere (28,61,62,63) was observed in the plot from the total strain control test, but not in the plot from the plastic strain control test. Sometimes, the departure from linearity was attributed to environmental

effects or different deformation mechanisms in low strain and high strain regimes (40). It should be noted, as mentioned before, that those results were obtained from total strain control test. From the above observation, it can be concluded that the plastic strain control test which compensates automatically for the plastic strain variation due to cyclic hardening or softening does show a more accurate Coffin-Manson relation representing fatigue resistance.

The fatigue life plotted from the plastic strain control test does not show any appreciable differences between different tempers tested when account is taken of the experimental scatter band (see Figure 12). Also, both the fracture ductility coefficient, ϵ_f , and the fatigue ductility exponent, c , which have been regarded as parameters indicative of fatigue resistance do not show any systematic relations between different tempers (refer to Table III).

Fatigue crack initiation during cyclic deformation generally occurs in regions where strain has become localized such as in a slip band, at inclusions, or at grain boundaries. It was suggested that overall hardening/softening may occur prior to strain localization but is generally not critical to the initiation of fatigue cracks (64). The most intriguing aspect of the crack initiation process relates to the generation of the nucleation sites. Although strains under monotonic loading produce surface offsets that resemble a staircase morphology, cyclic strains produce sharp peaks (extrusions) and troughs (intrusions) (65,66) resulting from non-reversible slip. These surface upheavals represent the free surface terminations of dense bands of highly localized slip,

which are called "persistent slip band" (PSB) due to the fact that they persist more or less unchanged throughout the major part of a low strain amplitude fatigue test, and that they persist after the surface of a specimen is electropolished and re-strained.

On the other hand, high-strength alloys in which slip is normally difficult are subject to crack initiation at inclusions in the form of impurities, undissolved second phase, and precipitate hardened particles. In 2024-T4 commercial aluminum, Grosskreutz and Shaw (67) observed that crack nucleation occurs at the interface between a surface impurity inclusion and the alloy matrix, and further proposed the interfacial debonding mechanism for producing cracks. They also showed that cracked constituent particles either formed during processing or during fatigue loading did not initiate fatigue cracks in the matrix.

Kung and Fine (68) recently reported the combined view of crack initiation in 2024-T4 aluminum and 2124-T4 which is a high purity version of 2024. They found that at high stresses fatigue cracks were initiated on coarse slip bands while at low stresses crack initiations were favored at constituent particles.

Even though a systematic investigation of fatigue crack initiation has not been performed in this LCF test program, the fracture surface observation of LCF test specimens revealed that the T351 temper favors coarse slip bands as crack initiation sites, whereas the T851 and T851* tempers seem to favor large second phase particles as crack initiation sites. During cyclic deformation, slip lines were readily seen on electropolished specimen surfaces under an optical telescope of

low magnification (X40) and cracks were observed to nucleate on the heavily deformed slip line. This observation can be explained by noting that the T351 temper is more prone to localized shearing.

The EDAX analysis of the second phase particles comprising the fatigue crack nucleation sites, as shown by the fractographs in Section II, frequently showed peaks characteristic of non-metallic constituents. This implies that these second phase particles were attacked leaving pits or debonded from matrix during the electropolishing process. These electropolishing pits or debonded interfaces have the effect of stress concentrators, hence could be more effective in assisting the fatigue crack initiation.

Consequently, it can be suggested that the fatigue crack is initiated more easily at the second phase particles or etch pits within the slip band where the dislocation slip motion can be impinged or blocked.

5.4 Crack Closure and Fatigue Crack Growth Under Uniform Loading

Through the fatigue growth behavior investigation, a highly sensitive and accurate differential compliance technique has been used to measure fatigue crack growth rates and to determine crack tip closure loads, especially under plane strain conditions. It should be pointed out that the compliance technique described here represents the purely mechanical crack and provides a through-thickness measurement which is a critical point in interpreting plane strain phenomena. For ductile materials, such as 2048 or 2024 aluminum, for example, it has been repeatedly observed that cracks lag behind on the free surfaces of compact tension specimens even after proper stress relief, as explained in Section III, is performed. Therefore, surface measurement techniques such as

optical microscopy or strain gauges glued ahead of the crack would, in the case of our experiments on 25.4 mm thick specimens, give an inaccurate description of crack length and crack growth rates. Also, the differential compliance technique employed here has been shown to be very accurate by comparison of the calculated crack lengths with the directly observed values under fractography as discussed earlier (see Figure 36).

At this point, it is worth mentioning several other methods to measure crack closure proposed in the literature. Some of them can be briefly evaluated as follows (69): [1] Electrical potential method - This method was developed for automatic crack length measurement. It is possible to use this method, but difficulties may arise due to electrical short circuits over the crack, for example, at the shear lips or some other minor asperities left on the fracture surface. Further, a mechanically open crack is not the same as an electrically open crack. [2] Ultrasonic transmission of surface waves through the crack line - Transmission is possible if the crack is closed. However, acoustic short circuiting is possible. Again, a mechanically open crack is not the same as an "acoustically" open crack. [3] Strain gages on the surface near the crack - Indications of non-linear behavior are obtained, but interpretation problems occur. This technique mostly detects the closure effect on the surface, which is in plane stress.

It has been found experimentally that the fatigue crack growth rate is much influenced by loading history. Since this effect can be explained in terms of crack closure, a good deal of attention in this research was paid to the measurement of crack tip closure and to the

attempt to correlate closure, through the notion of an effective stress intensity range, ΔK_{eff} , with crack growth rates, da/dN , quantitatively. As the previous discussion of results has indicated, a reasonably good correlation does exist for simple loading histories. The closure model also seemed to provide an accurate description of overload retardation effects in that when the increased opening loads due to the overload affected region were used to define ΔK_{eff} the da/dN versus ΔK_{eff} relationship obtained was in very good agreement with that obtained using uniform loading histories.

The phenomenology of crack closure is, as shown in Figure 24 of Section III, rather complex and depends upon both microstructure and stress intensity range. An abrupt decrease in opening load occurs suddenly at a certain range of K_{max} and gives rise to an apparent transition in crack tip closure. McEvily (10) claimed that the difference in compliance of the various specimens may have contributed to the difference in closure levels observed on the post-transition part. In the present study, however, the results contained in Table IV along with the reversibility of transition effect demonstrated show that this transition was not simply related to crack length (a/w) or overall specimen compliance (including geometry) but was related to the attainment of a critical K_{max} level, at least when the stress ratio $R (=L_{min}/L_{max})$ is less than 0.20.

The magnitude of the crack opening loads seemed to be associated with the mode of crack advance. It was suggested (10) that crack growth is characterized by Mode II (shearing mode) at low ΔK followed by

predominantly Mode I (opening mode) growth at high ΔK . Fractographic evidence changes with ΔK level which is consistent with this notion has been presented by Santner and Fine (2) for crack growth in both aluminum 3.6 wt percent copper alloys and naturally aged aluminum. Recently, Otsuka et al. (14) have also ascertained by fractographic analysis that crack growth in the near threshold region occurs by a Mode II process rather than by a Mode I process, showing faceted fracture surface around the threshold region in low carbon steel. Furthermore, Hornbogen and Gahr (70) have shown that in iron-nickel-aluminum alloys, aged to contain coherent precipitates, fatigue crack occurs in a shearing mode (their "slip band decohesion") at low ΔK . At low ΔK the fracture surfaces are characterized by shearing fracture of considerable zig-zag deviations of the fatigue crack from the plane normal to the stressing axis, and hence a very rough topography whereas after the transition the surfaces are much smoother.

Shearing modes lead to a rough fracture surface topography which in turn would lead to the large K_{open}/K_{max} displayed in Figure 24 and thus possibly a reduced crack growth rate. One uncertainty in applying the crack closure model in this case is of course that full opening of the crack is unnecessary for growth in the shear mode. However, with the above mentioned evidence for fracture mode transition and grain size in mind the computed plastic zone sizes ahead of the crack at the K_{max} closure transition level were compared with the measured grain widths under optical microscopy. Table IV shows some details on nine typical tests on both 1 inch and 1/2 inch thick specimens and there the plastic

zone sizes were computed as the maximum extent of a monotonic zone at $K = K_{\max}$. The comparison is certainly a favorable one within a small scatter range. Now in a related study Irving et al. (12,71) noted similar transitions in fracture topology in structural titanium alloys and there they attempted to correlate the onset of this fractographic transition with the attainment of a reversed plastic zone size (cf. Ref. (72)) comparable to the grain size. The correlation in our results, however, strongly suggests that the transition occurs when the computed monotonic plastic zone size extends fully over at least one grain, and once this happens the fracture mode changes from shearing mode to opening mode. The above results are also in good agreement with those of Paris and Hermann (7) who studied crack growth and crack tip closure of 2024 aluminum. It is important to note that the present context, grain size should be interpreted as grain width.

The above observation can also explain why the coarse grain structures led to higher closure loads and lower growth rates than the fine grain structures in an intermediate ΔK range. Recently, Louwaard (15) has reported an interesting example of slip induced closure effects on a 7075 aluminum alloy. The alloys with a large grain size displayed a "slip band cracking" fracture mode within the grains which lead to high closure levels and low values of crack growth rate, especially in vacuum. Here again, the high closure is presumably related to the rough fracture topology accompanied by frequent and intensive crack branching. A similar behavior was not observed in fine grained material. While it may be that large grains impose less restraints on grain matrix shearing, there are a

number of observations which suggest that the slip properties are also very important in determining if localized shear will occur. Asaro (4) showed that small coherent or even semi-coherent precipitates or zones are more conducive to shear instabilities and plastic strain localization than large incoherent precipitates. Hornbogen and Graf (16) also found that localized shearing, slip-band fracture and reduced crack growth rates occurred in sheets of underaged iron-nickel-aluminum alloys. These were not grain size effects, but were clearly related to the precipitate size and degree of coherency. Localized shearing and slip band cracking did not occur in overaged alloys. Consequently at low K_{max} levels, i.e. below the transition in K_{open}/K_{max} , the crack front seemed to undergo pronounced out-of-shearing which led to the rough fracture surface topology. These behaviors are generally favored by coarse grain size, underaged microstructures, and inert environments. Also, as pointed out in earlier reports (73,74), all three of these factors favor non-uniform plastic deformation by localized shearing within the grain matrices. We believe that the large closure loads in the pre-transition region are, in fact, primarily due to the "residual cracking" of the asperities left on the fracture surface which are shown in Figure 28b in the intermediate wake of the crack tip. At large values of K_{max} the fracture surfaces are decidedly smoother and the value of the opening load (along with K_{open}/K_{max}) decreases. Another observation of several microbranches on the cross-sectional surface of the crack before the transition also gives good evidence that crack growth by a shearing mode is operative in the pre-transition zone, and explains the low growth rate at low ΔK .

However, few branches were observed in the post-transition zone where the crack grows by a tensile mode. In this point, Priddle (75) has ascertained that the crack deviations on shear planes and crack branching in coarse grain materials imply a departure from the homogeneous isotropic material which is assumed for a correct analysis and treatment of the results by fracture mechanics theory. The crack deviation from the plane of maximum tensile stress leads to a reduction in K_I and increase in K_{II} stress intensity components (76). This reasoning may explain the poor relation between da/dN and ΔK or ΔK_{eff} in the pre-transition zone, as shown in Figure 25.

It was shown in an earlier report (40) that 2048 aluminum showed superior fatigue resistance to the 2024 aluminum in the higher ΔK range (opening mode) but slightly inferior properties in the lower ΔK range (shear mode). This observation is consistent with that of El-Soudani and Pelloux (81) who found that improvement in resistance to fatigue crack growth with lower inclusion contents are observed only in the high ΔK range for 7075 aluminum. Further, Munz et al. (77) found during the fatigue initiation test that the distribution of the dislocations was uniform in the commercial 2024 aluminum whereas the pure alloy X-2024 (presumably close to 2048 here) showed an inhomogeneous distribution of dislocations which were arranged in narrow deformation bands. Along with above observations, it can be concluded that when the shearing mode is predominantly active, the second phase particles due to impurity can serve as an obstacle for dislocation glide. On the other hand, when the opening mode is dominant, those particles can cause the formation of voids

by tearing along the interfaces between the matrix and those particles. The above arguments can be given as indirect evidence of mode transition, but further investigations are required.

5.5 Fracture Toughness

The plane strain toughness test results show that the T351 temper is toughest among others. Also, the K_{IC} value of $37.5 \text{ MPa}\sqrt{\text{m}}$ for the fine grained T851 temper is comparable to literature value of $38.5 \text{ MPa}\sqrt{\text{m}}$ (42), so that the validity of our test can be justified. It should be noted that these values are obtained from the specimens of longitudinal transverse (L-T) orientation. Yahn and Rosenfield (78) suggested that in commercial aluminum the fracture toughness depends on [a] the extent of the heavily strained region ahead of the crack tip which is a function of yield strength and modulus, [b] the size of the ligaments which are related to the volume fraction of cracked particles, and [c] the work of rupturing the ligaments. While they (78) suggested fracture toughness dependence on yielding strength, the results here show that toughness strongly depends on ductility of materials. The fine grained T851 temper shows higher ductility and thus higher K_{IC} value than the coarse grain T851 or T851* tempers (see Table III), even though the former had a higher yield strength. Aside from the grain size effect, the coarse grain T851 temper shows higher K_{IC} value than the coarse grain T851* temper, again due to its higher ductility.

With respect to precipitates characteristics, the particle-matrix interface of non-coherent second phase particles may be sufficiently weak that cavity formation begins as soon as the matrix begins to deform.

With respect to the particle size, it is general observation that the larger particles fracture at lower plastic strains than small particles. The dislocation model suggests (79) that up to some limiting size, screw dislocation blocked by a particle may cross slip around the particle by jogging, but that beyond this limiting size, cross slipping becomes impossible and dislocations may pile up at the particle, creating high local stresses across the particle-matrix interface sufficient to cause separation.

5.6 Overload Retardation and Crack Growth Under Complex Loading

As a first step toward understanding fatigue crack growth under spectrum loading, as encountered in real service conditions, overload retardation and load interaction effects were studied by applying a single cycle, and periodic single cycle overloads. Throughout the test, only the 100 percent overloads were applied to compare the magnitude of retardation effects between the different tempers studied. Recently, a number of different observations on retardation phenomena due to various factors have been reported and summarized by Corbly and Packman (80).

All three tempers showed considerable amount of crack retardation following overload although the magnitude was greatest in the T351 temper. The phenomenology of closure, following even simple overloads though, is quite complicated. As shown in Figures 21 and 29b, c, there are two distinct opening loads after the overload applied. The lower opening load is usually of lesser magnitude than that prevailing just prior to the overload, whereas the upper opening load is considerably larger. The latter goes through a transient increase followed by a continuous

decrease to the level existing before the overload. When this upper opening load is used to compute K_{open} and ΔK_{eff} , the results shown in Figure 29d are obtained. Therefore, it can be concluded that the retardation phenomenon is accounted for quantitatively using the idea of crack tip closure, at least for single cycle overloads.

Overload effects were cumulative in that when subsequent overloads were applied before the crack had fully grown out of the overload affected zone both the closure loads and the magnitude of retardation increased. The extent of this overload affected zone appeared to correlate well with the computed "static" plastic zone size. For the case of "isolated" periodic overload, the interaction effects between the subsequent overloads were not observed. The retardation phenomenon for multiple cycle overloads is, indeed again, reasonably well accounted for quantitatively using the crack tip closure model. The next step in a study of this type is to super impose a more complex loading pattern in an attempt to simulate spectrum loading.

III. 6. Conclusions

[1] Underaged microstructures (T351) have shown continuous cyclic hardening over the entire strain amplitude range whereas peakaged (T851) or slightly overaged (T851*) microstructures have shown continuous cyclic softening until fracture. Fatigue initiation life based on the plastic strain control tests has not shown any significant difference between the microstructures tested. Plastic strain control test provided a more accurate correlation with the Coffin-Manson plot than total strain control tests for microstructures tested here. Fatigue crack frequently

initiated from the second phase particles on the surface.

[2] Crack closure model provided an accurate and quantitative description of overload retardation effects as well as crack growth in constant amplitude loading. The magnitude of crack opening loads seemed to be associated with the mode of crack advance. At low K_{max} level, that is below the transition in K_{open}/K_{max} , the crack front seemed to undergo out-of-plane shearing which led to the rough fracture surface topology. This transition of closure load correlated well with a critical value of K_{max} which yielded a computed zone size approximately equal to the grain width.

[3] The underaged microstructure and the coarse grain size material showed large crack tip closure loads and thus low crack growth rates. These behaviors are attributed to an increased tendency for localized shearing within the grain matrices.

[4] Overload effect was cumulative when subsequent overloads were applied before crack had fully grown out of the overload affected zone. The greatest amounts of retardation following single cycle and periodic single cycle overloads was observed in underaged microstructures.

[5] The differential compliance technique employed in present study produces a "mechanical definition" of crack length and closure. We believe that this technique is superior to surface measurement procedures in that it provides a more realistic estimate of "through thickness" phenomena and is capable of detecting crack length changes of less than 0.01 mm.

III. 7.1 List of Tables

	<u>page</u>
TABLE I. Chemical Analysis of 2048 Aluminum in Weight Percent	14
TABLE II. Ageing Designation and Condition Used for 2048 Aluminum Specimen	14
TABLE III. Monotonic Tensile and Cyclic Parameters	26
TABLE IV. K_{max} Value and Plastic Zone Size Computed at Transition	65
TABLE V. Plane Strain Fracture Toughness (K_{IC}) at Room Temperature	70

III. 7.2 List of Figures

	<u>page</u>
Figure 1. Typical grain structure in 2048-T351. A shows the rolling direction. Crack's plane is parallel to face B and its front is parallel to edge C	15
Figure 2. Dimensions of low cycle fatigue specimen (unit:mm)	15
Figure 3. The final stage of total strain control LCF test shows the distorted hysteresis loops when a macroscopic large crack developed. Note that the tensile peak continuously drops while the compressive peak remains nearly constant	18
Figure 4. Hysteresis loops during the incremental strain step test (a) T351 temper shows the cyclic hardening behavior (b) T851 temper shows the cyclic softening behavior (c) T851* temper after 3 blocks of incremental strain shows the stable, solid hysteresis loops (a) and (b) taken from the first decreasing strain block are not stabilized yet. Monotonic stress-strain curves were taken from the first quarter cycle of (a) and (b)	21
Figure 5. Monotonic and cyclic stress-strain curves obtained during the incremental step test (a) T351 temper is cyclically hardened over the entire plastic strain range (b) T851, (c) T851* and (d) fine grained T851 temper are cyclically softened over the entire plastic strain range	24
Figure 6. Cyclic hysteresis loops from 1 to 10 cycles from the fine grained T851 temper, tested at total strain amplitude of $\pm 1.0\%$. The doubly inflected behavior of reversed deformation are shown clearly in the first hysteresis loop and diminishes as the cyclic loading goes on	28
Figure 7. Cyclic response curves for different microstructures from total strain control tests (a) T351 (b) T851 (c) T851* (d) Fine grained T851 temper. The constant strain amplitudes in percent are indicated on the curves. Note that	

the cyclic stress amplitude was determined by taking average values of tensile and compressive peaks in each hysteresis loop. Only the T351 temper shows cyclic hardening behavior 30

Figure 8. Hysteresis loops of 1 to 10 cycles taken from the plastic strain control test on T851 temper. The plastic strain amplitude was $\pm 0.5\%$. Slightly wavy curves are due to stepwise motion of loading ram by computer control. Note that the half widths of the hysteresis loops are smaller than the plastic strain amplitude, probably due to reversed plastic flow even at positive stress 33

Figure 9. Cyclic response curves obtained from plastic strain control tests
(a) T351 (b) T851 (c) T851* (d) Fine grained T851 temper. The plastic strain amplitude in percent are indicated on the curves. These magnitudes are corrected values according to explanations in the text 34

Figure 10. (a) Typical stress-strain hysteresis loop. Total strain can be divided into an elastic strain portion and a plastic strain portion.
(b) Typical strain-life curves for elastic, plastic and total strain amplitudes. For the notations, see the text 37

Figure 11. Strain-fatigue life relations for different microstructures studied
(a) T351 (b) T851 (c) T851* (d) Fine grained T851 temper. In these graphs, the cross mark represents the computed plastic strain amplitude determined at half life in total strain control test, whereas the open square represents the fixed value from the plastic strain control test. Note that the T351 temper shows a big difference between two values 39

Figure 12. Fatigue life vs plastic strain amplitude plot. Only the results obtained from plastic strain control tests were plotted to compare the LCF resistance of different microstructures 42

Figure 13. SEM photograph showing a cluster of surface cracks around the fatigue crack initiation site marked as A. Surface cracks are parallel to fracture surface

and left chevron marks below the initiation site. From the T351 temper in the plastic strain amplitude of $\pm 0.2\% \times 150$ 43

- Figure 14. SEM fractographs taken from the T851* temper specimen tested at $\pm 0.5\%$ total strain amplitude
(a) Multiple initiation sites are shown as A, B, C at low magnification (x15)
(b) Magnified view (x150) of A shows feathery marks emanating from nucleation "eye".
(c) and (d) are higher magnification of B and C, respectively 45

- Figure 15. SEM fractographs showing large second phase inclusions on the initiation site
(a) inclusion of $15 \mu\text{m} \times 700$, T851 temper
(b) inclusion of $20 \mu\text{m} \times 400$, T851 temper
EDAX analysis showed that both inclusions are Si-bearing impurity particles 47

- Figure 16. Transitions from Stage I to Stage II characterized by (a) striations perpendicular to propagation directions or (b) steps; (a) also shows a small inclusion on the initiation "eye" which turned out as CuAl_2 by EDAX analysis 48

- Figure 17. Ductile striations comprising secondary cracks at the roots
(a) T851 temper at x1500 magnification
(b) T851* temper at x900 magnification 49

- Figure 18. The end stage of fatigue shows the mixed mode of ductile striation and intermingled dimples 50

- Figure 19. The final overloaded zone by tensile fracture shows stretched zone and dimples associated with the second-phase particles 50

- Figure 20. Block diagram of differential compliance system 55

- Figure 21. Photographs of unreduced data as plotted X-Y recorders in the laboratory
(a) Recorded curves of load vs load point displacement
(b) Recorded curves of load vs differential displacement for uniform loading

- (c) Same as (b)
- (d) Same as (b) and (c) after a single cycle overload 56

- Figure 22. "Frictionless grips" used for compliance measurements
- (a) A view of compact tension specimen and hanger plates with labelling corresponding to that in (b)
 - (b) Schematic diagram of bending of a specimen and of compensating flexing of hanger plates for the grip configuration shown in (a). N indicates the flexible necked-down sections of the hanger plates, P indicates the loading pins and S indicates the set screws used to prevent rotation of specimen about the pins 58

- Figure 23. Dimensions of our modified compact tension specimens (unit:mm). Note that the modified specimen has the razor edges on its load line to measure the load-line displacement 60

- Figure 24. Fatigue crack closure in coarse and fine grain 2048 aluminum represented in terms of the ratio K_{open}/K_{max} versus normalized crack length a/w . Closed squares represented a test involving load reductions following the transition from high to low closure which shows increasing closure behavior. Note that there is no apparent transition in the case of constant $K_{max} < K_{transition}$ as shown with asterisks 63

- Figure 25. Typical crack growth rate data for three different tempers represented in terms of ΔK and ΔK_{eff} 68

- Figure 26. Load-crack opening displacement curves for different microstructures tested. The steeper linear slope for T351 temper is due to short crack length. P_0 , the intersection point of curve and 0.95 of linear slope, is used for calculation of K_{IC} value 71

- Figure 27. Optical microscopy of fatigue crack profile showing a number of microbranches prior to the transition point which is indicated by the arrow . . . 73

- Figure 28. (a) Scanning electron fractograph showing secondary cracks labelled by "A" parallel to the specimen surface. The propagation direction was indicated by the arrow.
- (b) Typical scanning electron fractograph of 2048 aluminum showing a fragment labelled by "B". The propagation direction was indicated by the arrow 75

- Figure 29. Results on overload retardation in crack growth following a single cycle overload in 2048-T851.
- (a) Crack length vs number of cycles applied. The solid line represents the estimated crack growth rate curve without overload.
- (b) Variation of lower and upper opening loads with crack length. The straight solid line shows the level of single opening loads before the overload. Note that the lower opening load disappears to become a single opening load after point 15, implying that the crack has grown out of the overload affected region.
- (c) Lower and upper opening loads vs number of cycles applied. The solid line again shows the level of opening loads before the overload.
- (d) Crack growth rates vs ΔK_{eff} . The closed circles indicate the crack growth rates before overload and the open circle after overload 79

- Figure 30. Retardation of crack growth in the T351 temper following periodic single cycle overload with 5000 cycle intervals
- (a) Crack length vs number of cycles applied. The solid curve shows the estimated growth rate curve without any overloads.
- (b) Closure level variation with number of cycles. Note that the average closure levels monotonically increase following each overload 85

- Figure 31. Results on crack retardation in the T851* temper by "isolated" single cycle overloads
- (a) Crack length vs number of cycles applied.
- (b) Closure level variation with number of cycles. The absence of cumulative effects in (a) can be explained by the monotonic decrease of average closure levels after each overload 88

- Figure 32. Crack growth retardation in the T851 temper following periodic single cycle overload with 3000 cycle intervals
- (a) Crack length vs number of cycles applied. The crack growth rate curve is gradually decreasing after undergoing each overload
 - (b) Magnified growth curve showing the decreasing slope following each overload
 - (c) Closure level variation with number of cycles. The apparently increasing closure levels would predict decrease in growth rate after undergoing each overload 90
- Figure 33. Comparison of overload retardation after multiple overloads for the three tempers. Overload intervals are 5000 cycles for the T351 and T851* tempers and 3000 cycles for the T851 temper 94
- Figure 34. Crack growth data after each overload for three different tempers in terms of ΔK_{eff} . The straight lines on each plot are based upon Figure 25, which shows the results from uniform load amplitudes 95
- Figure 35. Scanning electron fractograph of the overload zone in 2048 aluminum. The propagation direction was indicated by the arrow 97
- Figure 36. SEM fractographs after periodic overloads
- (a) T851 temper subjected to eight overloads. The first five overloads are indicated as a guide to their location.
 - (b) T851* temper
 - (c) T351 temper
- The comparison of computed and measured crack length changes establishes the accuracy of the differential compliance technique 98

IV. References

1. C. Calabrese and C. Laird, *Journal of Materials Science and Engineering*, Vol. 13, 1974, pp. 141-157.
2. J. S. Santner and M. E. Fine, *Metallurgical Transaction A*, Vol. 7A, 1976, pp. 583-593.
3. M. Gell and G. R. Leverant, *Acta Metallurgica*, Vol. 12, 1964, p. 159.
4. R. J. Asaro, "Strain Localization and Fracture in Ductile Crystals," *Brown Report*, Feb., 1978.
5. W. Elber, *Engineering Fracture Mechanics*, Vol. 2, 1970, pp. 37-45.
6. W. Elber, *ASTM STP 486*, 1971, pp. 230-242.
7. P. Paris and L. Hermann, in proceedings of the "International Congress on Theoretical and Applied Mechanics," Delft Pub. North-Holland, Amsterdam, 1977.
8. M. W. Mahoney and N. E. Paton, "4th International Conference on Fracture," Univ. of Waterloo, Canada, D.M.R. Taplin ed., Pergamon Press, 1977, pp. 1081-1089.
9. D. P. Musil and R. I. Stephens, *Ibid.*, pp. 1017-1024.
10. A. J. McEvily, *Metal Science*, 1977, p. 274.
11. O. Buck, J. D. Frandeson, and H. L. Marcus, *Engineering Fracture Mechanics*, Vol. 7, 1975, pp. 167-171.
12. P. F. Irving, J. L. Robinson, and C. J. Beevers, *Ibid.*, p. 619.
13. P. Paris, *Proceedings of the 10th Sagamore Conference*, Syracuse University, 1965, p. 107.
14. A. Otsuka, K. Mori, and T. Miyata, *Engineering Fracture Mechanics*, Vol. 7, 1975, p. 429.
15. E. P. Louwaard, *Report LR-243*, Delft Univ. of Tech., Jan., 1977.
16. E. Hornbogen and M. Graf, *Acta Metallurgica*, Vol. 25, 1977, p. 877.
17. R. W. Landgraf, *ASTM STP 467*, 1970, pp. 3-36.
18. L. F. Coffin, Jr., *ASTM STP 465*, 1969.
19. E. A. Starke, Jr., *Materials Science and Engineering*, Vol. 29, 1977, pp. 99-115.
20. R. W. Landgraf, J. Morrow and T. Endo, *Journal of Materials*, Vol. 4, 1969, pp. 176-188.

21. D. R. Raske and J. Morrow, ASTM STP 465, 1969, pp. 1-25.
22. C. E. Feltner and M. R. Mitchell, ASTM STP 465, 1969, pp. 27-66.
23. R. J. Asaro, Acta Metallurgica, Vol. 23, 1975, pp. 1255-1265.
24. R. E. Stoltz and R. M. Pelloux, "Work Hardening in Tension and Fatigue," AIME pub., A. W. Thompson ed., 1975, pp. 224-239.
25. P. Lukas, M. Klesnil and J. Polak, Materials Science and Engineering, Vol. 15, 1974, pp. 239-245.
26. P. Lukas and J. Polak, "Work Hardening in Tension and Fatigue," AIME pub., A. W. Thompson ed., 1975, pp. 177-205.
27. R. W. Landgraf, Ibid., pp. 240-259.
28. S. S. Manson and M. H. Hirschberg, in "Fatigue: An Interdisciplinary Approach," Syracuse Univ. Press, Syracuse, N.Y., 1964, p. 133.
29. L. F. Coffin, Jr., Transaction of ASME, Vol. 76, 1954, p. 931.
30. S. S. Manson, NACA Technical Note 2933, 1954.
31. T. H. Sanders, Jr., D. A. Maunery, and J. T. Staley, "Fundamental Aspects of Structural Alloy Design," Jaffe and Wilcox ed., 1977, pp. 487-519.
32. F. J. Pitoniak, A. F. Grandt, L. T. Montulli, and P. F. Packman, Engineering Fracture Mechanics, Vol. 6, pp. 663-670.
33. T. T. Sih and R. P. Wei, Ibid., pp. 19-32.
34. O. Buck, C. L. Ho, and H. L. Marcus, Engineering Fracture Mechanics, Vol. 5, 1973, pp. 23-34.
35. J. D. Frandsen, R. V. Inman, and O. Buck, International Journal of Fracture Mechanics, Vol. 8, 1972, pp. 469-471.
36. R. Roberts and R. A. Schmidt, International Journal of Fracture Mechanics, Vol. 11, 1975, pp. 345-348.
37. M. Katcher and M. Kaplan, ASTM STP 559, 1974, pp. 264-282.
38. W. N. Sharpe, Jr., and A. F. Grandt, Jr., ASTM STP 590, 1976, pp. 302-320.
39. L. Hermann and P. Paris, unpublished research, Brown University.

40. J. M. Baik, M. S. Thesis, Brown University, 1979.
41. J. E. Srawley, "Wide Range Stress Intensity Factor Expressions for ASTM E399 Standard Fracture Toughness Specimens," NASA TMS-71881.
42. D. S. Thompson, Metallurgical Transaction A, Vol. 6A, 1975, pp. 671-683.
43. R. E. Jones, Engineering Fracture Mechanics, Vol. 3, 1973, p. 585.
44. J. Schijve, Advances in Aeronautical Sciences, Vol. 3, Pergamon Press, 1962, pp. 387-408.
45. O. E. Wheller, Journal of Basic Engineering Transaction, ASME, Vol. 94, Series D, No. 1, March 1972, pp. 181-186.
46. R. H. Christensen, Metal Fatigue, McGraw-Hill, New York, 1959, pp. 376-412.
47. E. F. J. VonEuw, R. W. Hertzberg, and R. Roberts, ASTM STP 513, 1972, pp. 230-259.
48. O. Buck, J. D. Frandsen and H. L. Marcus, ASTM 595, 1976, pp. 101-112.
49. W. G. Clark and R. C. Bates, "Microscopic Aspects of Fracture Toughness," Scientific Paper 69 - 109 - RDAFC - PI, Westinghouse Research Laboratories, Dec., 1969.
50. J. T. Staley, ASTM STP 605, 1976, pp. 71-103.
51. J. G. Kaufman, "Specialist Meeting on Alloy Design for Fatigue and Fracture Resistance," AGARD - CP - 185, 1976, pp. 2.1-2.26.
52. E. Orowan, "Fracture and Strength of Solids," Reports of Progress in Physics, Vol. 12, 1948-9, p. 185.
53. J. Polak, M. Klesnil, and P. Lukas, Materials Science and Engineering, Vol. 28, 1977, pp. 109-117.
54. K. Koibuchi and S. Kotani, ASTM 519, 1973, pp. 229-245.
55. C. E. Jaske, H. Mindlin, and J. S. Perrin, Ibid., pp. 13-27.
56. C. Laird, V. J. Langelo, M. Hollrah, N. C. Yang, and R. De La Veaux, Materials Science and Engineering, Vol. 32, 1978, pp. 137-160.
57. A. W. Thompson, "Work Hardening in Tension and Fatigue," AIME pub., A. W. Thompson ed., 1975, pp. 89-126.

58. R. W. Smith, M. H. Hirschberg, and S. S. Manson, "Fatigue Behavior of Materials Under Strain Cycling in Low and Intermediate Life Range," NASA TN D-1574, April, 1963.
59. M. E. Fine and J. S. Santner, *Scripta Metallurgica*, Vol. 9, 1975, pp. 1239-1241.
60. C. Calabrese and C. Laird, *Journal of Materials Science and Engineering*, Vol. 13, 1974, pp. 159-174.
61. T. Endo and J. Morrow, *Journal of Materials*, JMLSA, Vol. 4, No. 1, 1969, pp. 159-175.
62. T. H. Sanders and E. A. Starke, Jr., *Metallurgical Transaction A*, Vol. 7A, 1976, pp. 1407-1418.
63. R. E. Sanders, Jr., and E. A. Starke, Jr., *Materials Science and Engineering*, Vol. 28, 1977, pp. 53-68.
64. S. P. Lynch, ASTM STP 675, 1979, pp. 174-213.
65. W. A. Wood, "Fracture," Technology Press of M.I.T. and John Wiley, New York, 1959, p. 412.
66. W. A. Wood, *Treatise on Materials Science and Technology*, Vol. 5, H. Herman ed., Academic Press, New York, 1974, p. 129.
67. J. C. Grosskreutz and G. G. Shaw, "Proceedings of the 2nd International Conference on Fracture," P. L. Pratt ed., Chapman and Hall, London, 1969, pp. 620-629.
68. C. Y. Kung and M. E. Fine, *Metallurgical Transaction A*, Vol. 10A, 1979, pp. 603-610.
69. J. Schijve, "Four Lectures on Fatigue Crack Growth," Report LR-254, Delft Univ. of Technology, Netherlands, 1976.
70. E. Hornbogen and K. Z. Gahr, *Scripta Metallurgica*, Vol. 24, 1976, pp. 581-592.
71. P. E. Irving and C. J. Beevers, *Materials Science and Engineering*, Vol. 14, 1974, pp. 229-238.
72. J. R. Rice, ASTM STP 415, 1967, pp. 247-311.
73. R. J. Asaro, L. Hermann, and J. M. Baik, *Metallurgical Transaction A*, Vol. 12A, 1981, p. 1133.
74. J. M. Baik, L. Hermann, and R. J. Asaro, "Mechanics of Fatigue," AMD-Vol. 47, T. Mura ed., ASME Winter Meeting at Washington, 1981, pp. 33-51.

75. E. K. Priddle, *Scripta Metallurgica*, Vol. 12, 1978, pp. 49-56.
76. H. Kitagawa, R. Yunki, and T. Ohira, *Engineering Fracture Mechanics*, Vol. 7, 1975, p. 515.
77. G. Lutjering, H. Doker, and D. Munz, "Microstructure and Fatigue Behavior of Al-Alloys," paper 87, 3rd International Conference on the Strength of Metals and Alloys, Cambridge, England, 1973.
78. G. T. Hahn and A. R. Rosenfield, *Metallurgical Transaction A*, Vol. 6A, 1975, pp. 671-683.
79. J. R. Low, Jr., *Engineering Fracture Mechanics*, Vol. 1, 1968, pp. 47-53.
80. D. M. Corbly and P. F. Packman, *Engineering Fracture Mechanics*, Vol. 5, pp. 479-497.
81. S. M. El-Soudani and R. M. Pelloux, *Metallurgical Transaction*, Vol. 4, 1973, pp. 519-531.

V. Professional Personnel

The following people of the Division of Engineering at Brown University have been engaged in this research program:

Principal Investigator: Dr. Robert J. Asaro
Professor

Faculty Associate: Dr. L. B. Freund
Professor

Research Engineer: Mr. Laurenz Hermann
Senior Research Engineer

Graduate Research
Assistant: Dr. J. M. Baik
Ph.D. awarded June 1982

VI. Reports and Publications

1. Technical Report AFOSR Grant No. 77-3246 (1978)
2. "Transition in Fatigue Crack Closure in 2048 Aluminum"
R. J. Asaro, L. Hermann and J. M. Baik, to appear in
Metallurgical Transactions.
3. "An Instrumented Differential Compliance Technique for
Measuring Fatigue Crack Growth and Crack Closure",
L. Hermann, P. Paris and R. J. Asaro.
4. "A Line Plastic Zone Model for Steady Mode III Crack
Growth in an Elastic-Plastic Material", L. B. Freund
and L. B. Sills, J. Mech. Phys. Solids 28, 49 (1980).
5. Technical Report AFOSR Grant No. 77-3246 (1979).
6. "Fatigue Crack Growth and Overload Retardation in
2048 Aluminum", J. M. Baik, L. Hermann and R. J. Asaro,
submitted to J. Mechanics of Materials.
7. Technical Report AFOSR Grant No. 77-3246 (1980).
8. "Fatigue Crack Growth and Overload Retardation in
2048 Aluminum", in Mechanics of Fatigue, AMD Vol.
47, ASME, 1981.
9. Final Technical Report AFOSR Grant No. 77-3246 (1982).

Theses

1. J. M. Baik, "Fatigue Crack Growth and Overload Effects
in 2048 Aluminum", April, 1979.
2. J. M. Baik, "Microstructural and Mechanical Aspects of
Fatigue Crack Initiation and Growth in a 2048 Aluminum
Alloy", June 1982.

VII. Oral Presentations

1. AFOSR Workshop on Fatigue in Aluminum Alloys, held April, 1978 at Alcoa Tech. Center, Monroeville, PA.
2. "Fatigue Crack Growth in 2048 Aluminum", AIME meeting, February, 1979 in New Orleans, LA.
3. "Metallurgical Effects in Fatigue Crack Growth in 2048 Aluminum", Air Force Materials Research Laboratory, Dayton, Ohio, April, 1980.
4. "Fatigue Crack Growth and Overload Retardation in 2048 Aluminum", AIME meeting, October, 1981.
5. "Fatigue Crack Growth and Overload Retardation in 2048 Aluminum", Winter meeting of ASME, 1981.
6. "Microstructural and Mechanical Aspects of Fatigue Crack Initiation and Growth in a 2048 Aluminum Alloy", Imperial Clevite, Cleveland, Ohio, June 1982.
7. "Microstructural and Mechanical Aspects of Fatigue Crack Initiation and Growth in a 2048 Aluminum Alloy", Ames Laboratories, Ames, Iowa, June 1982.